ENHANCING PHASE CHANGE HEAT TRANSFER

VIA INTERFACIAL ENGINEERING

A Dissertation

by

RUISONG WANG

Submitted to the Graduate and Professional School of
Texas A&M University
in partial fulfillment of the requirements for the degree of

DOCTOR OF PHILOSOPHY

Chair of Committee,	Dion S. Antao
Committee Members,	James D. Batteas
	Jonathan R. Felts
	M. Cynthia Hipwell
Head of Department,	Guillermo Aguilar

May 2022

Major Subject: Mechanical Engineering

ABSTRACT

Liquid-vapor phase change processes play an essential role in maintaining the water balance in the natural water cycle and are ubiquitous in various industrial applications such as power generation and conversion, water harvesting/desalination, and electronics thermal management. The pursuit of enhancing phase change heat transfer and especially enhanced condensation has been ongoing for decades, as the improvements can have significant impacts on both the environment and the efficiency of energy systems in industries. Dropwise condensation typically facilitated with thin (<100 nm) low surface energy coatings is broadly known to enhance heat transfer due to faster shedding of the condensate. However, low surface tension fluids condense on these low surface energy coatings in the inefficient filmwise mode, and thin coatings at the thickness required to improve heat transfer typically degrade rapidly (minutes to hours) during water vapor condensation. More importantly, the degradation/failure mechanism(s) of these coatings during condensation remain unknown and/or unproven. In this dissertation, we present two pathways (*i.e.*, surface geometry method and surface energy method) to overcoming the existing limitations of low surface energy coatings and enhancing the performance of liquid-vapor phase change heat transfer accordingly. In the surface geometry method, we introduce a scalable and robust capillary-enhanced filmwise mode where condensation occurs within a high effective thermal conductivity porous condenser and condensate removal was sustained by the capillary forces within the porous media. The semi-analytical modeling framework incorporates the non-linear pressure gradient

obtained by discretization and the accurate local liquid-vapor interface (meniscus) curvature/shape, and demonstrates favorable enhancements on the heat transfer coefficients of low surface tension liquids. In the surface energy method, we present a mechanistic understanding of the condensation-mediated degradation of self-assembled monolayer coatings on silicon and copper surfaces, and we significantly extend the coating durability when condensing water vapor continuously. Elimination of water/moisture in the synthesis and proper surface terminations (*i.e.*, cleaning, polishing, plasma modification) are experimentally validated to be essential to obtain superior coating robustness for condensation. The novel insights from this work have the potential to drastically improve transport efficiency in enhanced phase change heat transfer applications and sustainable energy/water technologies.

ACKNOWLEDGEMENTS

My time spent in Texas has been incredibly amazing, and is primarily delighted by the people I meet and work with at A&M. First, I would like to express my deepest gratitude to my advisor Prof. Dion S. Antao, who has always been supportive and inspiring, and is literally the nicest person I have ever known. I still remember the first day I visited the lab, and the only thing existed was a huge optical table. We have completed an impressive job of building up a fully functioning lab from scratch over the past few years, and it would not be possible without Prof. Antao's professional guidance and creativity. There were days and nights that we spent in the lab together setting up equipment and deriving equations. Being the first PhD student in the lab is undoubtedly challenging, but Prof. Antao has made it so rewarding and less frustrating to me by providing increasing levels of freedom and trust. His patient mentoring and high standard for work are what help me grow into an independent researcher.

It is my great honor to have Prof. James Batteas, Prof. Jonathan Felts and Prof. Cynthia Hipwell on my dissertation committee. Their interdisciplinary insights and valuable advices helped me improve the quality of this work. I would like to thank Dr. Wilson Serem and Dr. Jing Wu from Materials Characterization Facility for the training on several equipment and many discussions. I also want to thank all current and former members in the Thermal Engineering Group, Sarojeet, Karan, Sanat, Sunil, Jiahui, Shiyu, Shoaib and Emily, who have been dependable colleagues and of great help in work.

I would like to dedicate my greatest thanks to my family. My parents brought me from a small town to Shanghai when I was a child, and none of these would have happened if it is not their courage and sacrifice. They always support me unconditionally in every single decision I have made, and they are absolutely the best role models to me on how to be a better person. I am deeply grateful to my beloved wife Hui Jiang, who has always been the biggest fan of me and the most awesome partner that I could ever imagine. I am getting a PhD when I just turned 27, but marrying her is still the largest achievement in my life. I have to thank my cat Blue for being a good boy and his years of close company. Family, including my baby Blue of course, is not only where my confidence comes from but also what motivates me to push myself further. Also, it is my fortune to have so many wonderful friends, and just to name a few: my best bro Jiaxi, Min, Xiaobo, Fangzhou, Yuan, Cole, Xin and many others (please forgive me for not listing all). They have made my life in Texas so delightful and remind me that I am never alone.

Finally, I would like to show my sincere appreciation to a mentor that I have never met (and unfortunately I will not have any chances to meet in the future), Kobe Bryant. I have learned to become a resilient fighter as Kobe was from his attention to details and obsession with winning, as he said, “The moment you give up is the moment you let someone else win.” His relentlessness and fearlessness have inspired me to overcome the setbacks in both work and life throughout the years. Mamba mentality is what have made me “me” to a certain extent, and will always be my incentive to work harder and improve myself.

In retrospect, what I own and what I have accomplished at this moment are beyond the wildest imagination that I would have before joining Texas A&M, and I could not be more grateful for all experiences and supports that brought me here. What an incredible journey in Aggieland! RUISONG OUT!

CONTRIBUTORS AND FUNDING SOURCES

Contributors

This work was supervised by a dissertation committee consisting of Professor Dion S. Antao (chair), Professor M. Cynthia Hipwell and Professor Jonathan R. Felts of the J. Mike Walker ’66 Department of Mechanical Engineering, and Professor James D. Batteas of the Department of Chemistry.

The liquid meniscus model in Chapter 3 was developed by Karan Jakhar and published in 2019; The heat exchanger insulation in Chapter 4 was designed by Shoaib Amhed and published in 2021; The polished copper samples in Chapter 4 was prepared by Jiahui Guo; The droplet departure diameters in Chapter 4 was obtained by Emily Muckleroy. All students above are affiliated with the J. Mike Walker ’66 Department of Mechanical Engineering. All other work conducted for the dissertation was completed by the student independently.

Funding Sources

Graduate study was supported by the J. Mike Walker ’66 Department of Mechanical Engineering at Texas A&M University. This work was also made possible in part by the U.S. Department of Energy, Office of Energy Efficiency and Renewable Energy under Grant DE-EE0008605, the American Chemical Society Petroleum Research Fund under Grant 61698-DNI9, and the U.S. National Science Foundation under Award 2048125. Its contents are solely the responsibility of the authors and do not necessarily

represent the official views of the U.S. Department of Energy, the American Chemical Society, and the U.S. National Science Foundation.

TABLE OF CONTENTS

Page

LIST OF FIGURES

Page

LIST OF TABLES

Page

CHAPTER I

OVERVIEW & INTRODUCTION

Three phase change processes, such as condensation (vapor to liquid), freezing (liquid to solid) and sublimation (solid to vapor), are ubiquitous in nature and energy industries (*e.g.*, power generation and energy conversion). Specifically, liquid-vapor phase change (*i.e.*, condensation, evaporation and boiling) plays an essential role in maintaining the water balance in the natural water cycle, and are prevalent in various industrial applications, for instance water harvesting/desalination, the biomedical industry, and electronics thermal management, due to the large latent heat released or absorbed by a thermodynamic system during the phase transition.[1-7] The pursuit of enhancing liquid-vapor phase change heat transfer has been ongoing for over half-a-century through two primary pathways: (i) minimizing the temperature difference between the bulk fluid and the solid surface where nucleation occurs; and (ii) tuning the wetting behavior of the nucleation surface *via* micro-/nanofabrication and low surface energy coatings.[6-9] A temperature difference between the solid/wall temperature and the liquid/vapor saturation temperature (*i.e.*, superheating in boiling and subcooling in condensation) is typically required for phase change to occur, and is often used to characterize the heat transfer in the corresponding process. Reducing the superheat and subcooling at the boiler and condenser of the Rankine cycle in the power generation systems improves the electrical output work, and in the refrigeration cycle, lower superheat and subcooling at the evaporator and condenser leads to a higher coefficient of performance.[6, 8, 10-12] The wettability of a solid surface with a certain fluid (*i.e.*, liquid or

gas/vapor) surrounded by another fluid determines the bubble and droplet dynamics in terms of nucleation, growth and departure. Creating micro-/nanotextured structures and heterogeneous surfaces alters the liquid wetting preference and increases the effective area for heat transfer; and modifying surface energy of the solid in contact with the bulk fluid (*i.e.*, liquid in boiling and vapor in condensation) with hydrophobic or hydrophilic coatings changes the liquid mobility, contact angles, and the preferential nucleation sites to accelerate the droplet/bubble departure and re-nucleation, leading to the enhanced critical heat fluxes and heat transfer coefficients.[8, 13-16]

Over the past few decades, remarkable enhancements of both boiling and condensation heat transfer have been demonstrated by numerous researchers in water-energy related fields with the utilization of low surface energy coatings, while enhancing evaporation has been well studied where the dominant method is increasing the effective surface area.[3, 6, 17] There are many parallels between boiling and condensation (*e.g.*, the nucleation and departure): vapor bubbles nucleate in a liquid pool and depart from the superheated surface during boiling, and liquid droplets nucleate in a vapor environment and shed from the condenser surface during condensation.[7, 8] However, the effects of low surface energy coatings appear to be different in the processes of condensation and boiling: in condensation, hydrophobic coatings are essential in fast droplet removal resulting from the low contact angle hysteresis, while in boiling, hydrophobic surfaces improve the bubble nucleation density, assisting in achieving a higher heat transfer coefficient, even though hydrophilic surfaces with low contact angles increase the critical heat flux. Therefore, many works have developed biphilic surfaces,

comprising both hydrophobic and hydrophilic surfaces, to create spatially varying wettability for boiling enhancements, where bubble nucleation occurs on hydrophobic region and the hydrophilic region prevents the formation of the undesirable vapor film (*i.e.*, constraining the bubble expansion in the lateral direction).[18-20] Similar hybrid surfaces have been demonstrated in condensation applications to suppress the condensate flooding on textured surfaces and improve the lifetime of promoting dropwise condensation, but the majority of studies still focus on enhancing condensation heat transfer with hydrophobic coatings.[21-24]

Although an extensive body of work has leveraged low surface energy coatings to enhance boiling and condensation heat transfer, there are two major limitations to industrial applications: (i) low surface energy coatings only repel high surface tension liquids (*e.g.*, water), while low surface tension liquids (*e.g.*, refrigerants and hydrocarbons that commonly used in power generation and refrigeration industries) still wet these coatings entirely; (ii) thin coatings (<1 μm) are known to fail rapidly with active nucleation at the coating-solid interface, but thicker coatings largely impede heat transfer due to the large thermal resistance resulting from low thermal conductivity coating materials.[13, 14, 25-29] Several encouraging techniques have been developed in the past decade (*e.g.*, lubricant-infused surfaces, and novel micro-/nanotextured surfaces) to work with low surface tension liquids, but the failure modes for these surfaces are mostly irreversible. Modifying the surface wettability with coatings exhibits more promising potential to be applied to industries owing to the superb scalability and the rising development of coating chemistries/materials, and is still the predominant research topic

in the field of enhanced phase change heat transfer. Since the current durability of the low surface energy coatings (mostly hours to days during water vapor condensation) is much lower than industries would typically require (years to tens of years), it is particularly essential to mitigate coating degradation (*i.e.*, extend the lifetime) during liquid-vapor phase change processes.[27, 28, 30] Unfortunately, only limited amount of work has looked at long-term robustness tests of such coatings under extreme phase change conditions (*i.e.*, condensation and boiling), and more importantly, there is little-to-no mechanistic understanding of how low surface energy coatings fail during continuous nucleation and how to extend their lifetime accordingly.

In this dissertation, we address a major bottleneck to adopting low surface energy coatings in the sustainable energy/water technology industry *via* providing durable solutions to enhance liquid-vapor phase change heat transfer with a focus on condensation, given the similarity between condensation and boiling. Both limitations of low surface energy coatings in: (i) repelling low surface tension liquids and (ii) inadequate coating robustness during condensation are resolved. Specifically, we develop a novel capillary-enhanced mode of condensation, which leverages capillary forces within a high thermal conductivity porous media to promote condensate removal, to increase the condensation heat transfer coefficient in the filmwise mode for a variety of fluids including low surface tension liquids. The corresponding semi-analytical model exhibits great versatility in modeling both condensation and evaporation phase change processes, and demonstrates excellent accuracy in predicting the heat transfer coefficient enhancement in condensation and the dry-out heat flux in evaporation through the

incorporation of actual meniscus curvature at the liquid-vapor interface. Furthermore, we elucidate the mechanism of condensation-mediated degradation of self-assembled monolayer (or SAM) coatings on silicon surfaces: the monolayer coatings fail during condensation due to the propagation of coating defects, which result from the presence of water/moisture during the coating synthesis process (*i.e.*, cross-linking of SAM molecules and wetting preference of the substrate contribute to these coating defects). The coatings deposited in a controlled/anhydrous condition exhibit superior long-term robustness with no signs of coating failure during water vapor condensation. Besides, we introduced oxygen plasma modification prior to controlled environment SAM coating on copper surfaces to facilitate better bonding with the dropwise promoter (*i.e.*, silane SAM), and achieved >500× extension on coating durability compared to the state-of-the-art for silane coatings on metal surfaces. Perfect dropwise condensation was maintained for coated copper tubes with a heat transfer coefficient enhancement ≈5-7× over the filmwise mode without any noticeable coating degradation. The work reported in this dissertation advances the enhancement of liquid-vapor phase change heat transfer *via* developing an innovative mode of condensation and mechanistically understanding (and validating) the degradation of dropwise condensation promoters. The novel insights from this work will enable the development of durable solutions to enhanced liquid-vapor phase change heat transfer in a variety of industrial applications, such as semiconductor industries, water harvesting/desalination, and energy conversion systems.

CHAPTER II

LITERATURE REVIEW & BACKGROUND

General phase change processes of matter include melting and freezing (liquid-solid), condensation, evaporation and boiling (liquid-vapor), and sublimation and deposition (solid-vapor). Particularly, liquid-vapor phase change is attractive to the heat transfer community due to the excellent heat dissipation/absorption ability arising from the large latent heat of a fluid, and has been widely applied to water-energy industries for a long time. Researchers have been looking into enhancing liquid-vapor phase change heat transfer, especially for condensation and boiling, for decades. In this chapter, a literature review and the background of liquid-vapor phase change heat transfer is discussed with a focus on water vapor condensation enhancement techniques. We cover the advances and developments of enhanced condensation over the past half-a-century from the traditional filmwise mode and dropwise mode to the jumping droplet mode and slippery liquid-infused porous surfaces (SLIPS) or lubricant-infused surfaces (LIS), and to other recent novel methods. The lifetime/durability of typical promoters for enhanced condensation and the corresponding proposed degradation mechanisms during water vapor condensation are also summarized.

This chapter includes general information on representative condensation modes and enhancement techniques, promoter durability, promoter degradation mechanisms, and some recent novel advances in this field.

2.1 Condensation Modes & Enhancement Techniques

2.1.1 Filmwise Condensation

When water vapor condenses on typical metal or metal oxide heat transfer surfaces, the high surface energy of these materials leads to the condensate (*i.e.*, liquid water) forming a liquid film on the condenser.[15, 16] The thin low thermal conductivity liquid film impedes heat transfer, and the resulting heat transfer mode is *filmwise* condensation.[15, 16, 28, 31] In 1916, Nusselt[31] developed models for laminar falling films on a vertical flat plate and a horizontal cylindrical tube to estimate the condensation heat transfer coefficient in the ideal case without considering the presence of non-condensable gases (NCGs), and this model has been extensively validated with experiments ever since.[26, 32-38]

Heat transfer can be enhanced during the filmwise mode by effectively increasing the surface area for heat transfer by roughening the condenser surface with micro-fins or cross-grooved fins, both of which are in use in commercial systems as enhanced tubes or finned tubes.[9, 39-43] An alternate method to enhance condensation is to decrease the effective thermal resistance of the liquid film (*via* increased thermal conductivity and/or reduced thickness) using a porous medium. Renken and Mueller[44] performed experiments with a porous metallic coating, showing a 200% increase in heat flux compared to a plain copper surface, and condensation occurred both inside and above the porous wick layer limiting performance, similar to condensation inside a heat pipe. Recently, Preston *et al.*[45] used a similar porous metal wick to enhance condensation heat transfer. Here, condensate flow was only inside the porous layer, and failure of this condensation mode was

determined as the heat transfer condition when the condensate formed a liquid film above the wick. Condensate flow through the wick was gravitationally driven and their experiments demonstrated condensation enhancement for pentane, a low surface tension fluid, of over 350%.

2.1.2 Traditional Dropwise Condensation

Reducing the surface energy at the condenser-condensate interface facilitates the formation of discrete droplets that shed from the condenser.[13, 14, 46] This dropwise condensation mode can result in more efficient heat transfer when droplet shedding occurs rapidly, with droplets sweeping the surface to create fresh locations for condensation.[33, 47-50] Polymer coatings and self-assembled monolayers (or SAMs) coatings are most commonly used dropwise promoters which are deposited on metal or metal oxide surfaces *via* chemical vapor deposition (CVD), solution-based deposition, spin coating, *etc*.

Polymer coatings such as polytetrafluoroethylene (PTFE) were studied in the 1950s to enhance condensation,[51-54] and various other organic/polymer coatings such as No-stik, silicone, parylene, *etc*., have been studied since.[55-57] These polymer coatings have been shown to have ≈0.4-8.6× enhancement in the heat transfer coefficient (HTC) and a lifetime of promoting DWC from a few days to over 2 years, depending on various aspects including the coating material, surface roughness, chemical activity of the substrate, and most importantly coating thickness.[55, 56] In 1986, Marto *et al.*[56] studied various polymer coatings (Fluoroacrylic, Parylene, No-stik and Emralon-333) with different thicknesses on titanium, copper and copper-nickel, and evaluated the effect of surface roughness level on

coating adhesion. This work was extended by Holden *et al.*[55] in 1987 with the addition of new coatings (*i.e.*, Nedox, Fluoroepoxy, Isonel and Silicone) and a wider range of coating thickness from 0.4 μm to 60 μm on similar metal surfaces.

Monolayer coatings such as self-assembled monolayers (SAMs) are commonly used to demonstrate condensation heat transfer enhancement due to the negligible thermal resistance of a single molecular layer (≈few nm). In 1946, Bigelow *et al.* deposited n-octadecylamine and n-nonadecanoic acid on 13 metal and non-metal surfaces to demonstrate the hydrophobicity, which is known to be the first study of self-assembled monolayer coatings.[58] Blackman *et al.* reported a broad study in 1957 with the deposition of 16 different alkyl chain compounds on copper and copper alloy surfaces,[59, 60] and since then alkylthiol SAMs have been widely applied on various metals to tune the surface wettability for condensation applications.[47, 61-64] More recently, alkylsilane SAMs have been studied extensively due to their favorable chemical and thermal stability compared to thiols.[65-67] In 1989, Wasserman *et al.* studied the wetting behavior and structures of alkyltrichlorosilanes at various chain lengths from 1 to 17 (*i.e.*, 1 to 17 carbon atoms in the alkyl chain), and they concluded that the wetting of these monolayer coatings are approximately independent of the chain length for longer chains (more than 4 carbon atoms).[68] Fadeev and McCarthy demonstrated the wettability of alkyl chlorosilanes with the chain length from 1 to 18 at different synthesis conditions, such as solution temperature, immersion time, and deposition methods (*i.e.*, vapor phase *vs* solution based).[69, 70] Naik *et al.* examined the structural alignments of alkylsilanes with different ending groups by multiple transmission and reflection infrared (MTR-IR) spectroscopy

and reported that chlorosilanes exhibit denser packing compared to ethoxysilanes and methoxysilanes.[71]

Recently, slippery omniphobic covalently attached liquid (SOCAL) coatings have gained much attention due to the excellent water repellency (contact angle hysteresis < 5°) and the simple and rapid deposition procedure.[72-76] Polymerization occurs during the evaporation/solidification of the coating solution, so that both monolayers and multilayers may appear depending on the drying time. Several works have shown good SOCAL coatings made by different chemicals with low surface roughness and minimal contact angle hysteresis,[74-76] however, no further studies on the coating properties other than wettability (*e.g.*, coating robustness, heat transfer performance) are reported. Other low surface energy coating or surface hydrophobization methods, such as depositing noble metals,[77-79] rare earth oxides[80-82] and ion implantation,[83-85] were also presented to promote dropwise condensation of water vapor.

2.1.3 Jumping Droplets

SAMs coatings (*i.e.*, thiols[62-64, 86] and silanes[32, 64, 87-90] discussed in Section 2.1.2) have been primarily deposited on nano/micro structured surfaces (*e.g.*, micropillar arrays and porous metal oxides) to create superhydrophobic surfaces, which promote the jumping droplet mode to enhance heat transfer during condensation. The jumping droplet mode of condensation was first demonstrated by Boreyko and Chen in 2009 by coating hexadecanethiol on a two-tier roughness surface with carbon nanotubes deposited on silicon micropillars.[91] They concluded that the droplet jumping/repelling is achieved by

the excess energy released from the coalescence of condensed microdroplets, and the out-of-plane motion was facilitated from the liquid bridge of the coalescing droplets impinging against the superhydrophobic substrate.[91, 92] Miljkovic *et al.* deposited trichloro(1H,1H,2H,2H-perfluorooctyl)silane (or TFTS) on a horizontal copper tube grown with cupric oxide (CuO) nanostructures, and the jumping droplet mode led to a 25% enhancement on heat flux and a 30% enhancement on heat transfer coefficient compared to the traditional dropwise condensation mode.[32] Wen *et al.* coated the same TFTS on a 3D copper nanowire network grown on a vertical copper condenser block and achieved a 100% higher heat flux compared to a flat hydrophobic surface, and the subcooling was sustained as high as 28°C.[93] Mukherjee *et al.* discovered that the jumping droplet size is one magnitude smaller for the inclined surfaces compared to a horizontal surface, and their heat transfer model showed a 40% HTC enhancement for a 45° tilted surface and a 100% HTC enhancement for a vertical surface.[94] Additionally, Miljkovic *et al.* found out that the jumped droplets gain net positive charges during the jumping that results in the droplets repelling each other due to electrostatic forces, which raised the possibility to further control/enhance droplet jumping with external electric fields.[95]

2.1.4 Hybrid Surfaces

In recent years, some researchers created hybrid surfaces comprising both hydrophilic and hydrophobic sections enabled by micro-/nanostructures and low surface energy coatings to further enhance condensate removal.[21-24, 96] Chatterjee *et al.* created a

patterned copper surface, where 25% of the surface is hydrophilic (circular bare copper) and the other 75% is coated with 200 nm thick Teflon AF, and the resulting heat transfer coefficient was significantly higher than filmwise mode but lower than the dropwise mode.[24] Peng *et al.* deposited n-octadecyl mercaptan (or octadecyl thiol) on the microgrooves of a polished copper surface, and reported the 23%, 11% and 7% enhancement in HTC compared to the traditional dropwise mode at the subcoolings of 2°C, 4°C and 6°C, respectively.[23] Hou *et al.* developed a hybrid surface with hydrophilic silicon dioxide micropillars and fluoropolymer coated hydrophobic nanograss, where filmwise condensation occurs on hydrophilic pillars first, transitions to dropwise as the droplets grow, and finally jumps off from the hybrid surface.[21] Lo *et al.* designed a hybrid silicon microchannel structure, where the grooves are hydrophilic and the ridges are silicon nanowires coated with 60 nm Teflon, and achieved the HTC enhancements of 184% and 84% compared to the hydrophilic surface and the hydrophobic surface, respectively.[22]

2.1.5 Slippery Liquid-Infused Porous Surfaces (SLIPS)

Slippery liquid infused porous surfaces (SLIPS) or lubricant-infused surfaces (LIS) imbibes low surface tension liquids (lubricants) into a textured solid surface functionalized with low surface energy coatings to promote dropwise condensation of an immiscible condensing liquid.[13, 14, 26, 97-105] The unprecedented water repellency (*i.e.*, extremely low contact angle hysteresis) was first demonstrated by Wong *et al.*[105] and Lafuma and Quéré[106] in 2011, and Anand *et al.*[97] captured the droplet growth and lubricant

cloaking with environmental scanning electron microscope (ESEM) in 2012. Since then, numerous work have leveraged SLIPS for self-cleaning, anti-icing and anti-fouling applications.[99, 104, 107]

Many studies developed theoretical description and numerical models to explain the droplet dynamics:[103, 108-110] Boreyko *et al.* reported a non-coalescence feature with a stable lipid bilayer replacing the thin oil membrane between the droplets;[108] Sun *et al.* demonstrated the non-traditional droplet motion that microdroplets move towards the big pseudo-stationary droplet at the oil rich region;[110] The model developed by Günay *et al.* specified the lubricant cloaking dynamics on condensed droplets with the incorporation of coalescence behavior, droplet formation and surface interactions.[109] There are also other works contributing to the optimization of designing SLIPS by validating the liquid-lubricant compatibilities with experiments.[101, 102] Sett *et al.* investigated the miscibility of a wide range of lubricants and impinging liquids with various liquid surface tensions and viscosities in order to verify the viability of the lubricant-liquid combinations.[102] Preston *et al.* developed an analytical model to predict the liquid-lubricant mixing, spreading and cloaking (*i.e.*, thin lubricant layer covering the condensate droplets) by incorporating the van Oss, Chaudhury, and Good (vOCG) model[111, 112] for polar components of surface tension, and they further validated the prediction with liquid displacement experiments.[101] The two works above provide guidelines for designing appropriate SLIPS and reveal that low surface energy coatings may not be required with proper selection of lubricant and condensing liquids when certain criteria are satisfied. More recently, Adera *et al.* used silica inverse opal structures

without hydrophobic coatings as the porous structure for SLIPS and achieved a 30% enhancement in HTC compared to the traditional dropwise mode.[113] It is worth mentioning that evacuating the chamber to a low pressure before starting a condensation experiment results in initial lubricant evaporation, and hence some non-condensable gases (NCGs) have to be included to facilitate an effective SLIPS.[26, 114] However, the presence of NCGs are known to decrease the heat transfer performance by forming a diffusion barrier near the condenser surface.[26, 115, 116]

Another important advantage of SLIPS besides the excellent water repellency, also highlighted by Sett *et al.*[102] and Preston *et al.*[101], is the capability of condensing low surface tension liquids in the droplet mode on the lubricant layer, while these low surface tension liquids exhibit the filmwise mode on low surface energy coatings.[15, 16, 26, 117, 118] Rykaczewski *et al.* utilized the alumina-silica nanotextures infused with Krytox perfluorinated oil (γ=17 mN/m) to promote dropwise condensation for toluene (γ=25 mN/m), octane (γ=21 mN/m), hexane (γ=18 mN/m) and pentane (γ=15 mN/m), however, ethanol (γ=25 mN/m) and isopropanol (γ=21 mN/m) exhibited a filmwise mode, though the surface tensions of these two liquids lie within the effective range.[117] They also showed lower predicted heat transfer coefficients of pentane, hexane and octane on SLIPS than on flat hydrophobic samples, while toluene has equivalent HTC with both surfaces. Preston *et al.* achieved a 450% HTC enhancement versus filmwise when condensing toluene (γ=25 mN/m) on TFTS-coated CuO nanoblades imbibed with Krytox GPL 101 fluorinated oil.[26] They also showed that the presence of non-condensable gases (NCGs) significantly impedes heat transfer performance with SLIPS. Sett *el al.* infused

Krytox 1525 oil into the same CuO nanoblade structures and obtained a 200% condensation HTC enhancement from SLIPS over the filmwise mode of condensation on a hydrophobic copper tube for both ethanol (γ=23 mN/m) and hexane (γ=19 mN/m).[118] Note that even if dropwise condensation of low surface tension fluids is achieved on SLIPS with proper lubricants, the contact angle hysteresis are not necessarily lower compare to those on traditional smooth hydrophobic surfaces.[117] However, a low contact angle hysteresis of low surface tension liquids on SLIPS is feasible if an appropriate lubricant is selected.[118]

2.2 Promoter Durability Tests

As summarized in Section 2.1, there have been extensive literature focusing on developing novel dropwise condensation promoters (low surface energy coatings, hybrid surfaces, SLIPS, *etc.*) to enhance heat transfer, however, these promoters are known to degrade (timescale relevant to the industry) during continuous condensation of water vapor. The condensation mode transitions to the inefficient filmwise mode once the surface modification fails to promote efficient dropwise condensation, leading to decreased heat transfer performance. The durability of these dropwise condensation promoters is the primary bottleneck preventing the adoption of efficient condensation enhancement methods in industries.

In this section, we briefly present the available literature work on the durability/lifetime of state-of-the-art condensation enhancement techniques, primarily focusing on low surface energy coatings (*i.e.*, polymers and SAMs) and SLIPS since their

robustness are more widely investigated. Although a number of studies have created hydrophobic-hydrophilic combinations on different substrates and various structures,[21-24] to our knowledge, there is no information on the durability of such hybrid surfaces during condensation. Also, there are assorted novel micro-/nanostructured materials and synthesis chemistry (*i.e.*, coating materials) developed to enhance the condensation *via* the jumping droplet mode, but the only available durability test in literature was reported very recently by Seo *et al.* (8 hours).[89] Note that the failure of the jumping droplet mode is also induced by the durability of corresponding coatings, which is discussed in Sections 2.3.1 and 2.3.2 below.

2.2.1 Polymers

Most studies focused on polymer coatings shared the consensus that increasing the coating thickness improved durability, but also led to a reduced enhancement in the heat transfer coefficient due to the large thermal resistance of low thermal conductivity coatings.[54] Marto *et al.* reported visual observations of both initial and long-term water dropwise condensation performance and the corresponding hours of operation for various polymer coatings on titanium, copper and copper-nickel surfaces at different roughness and thickness.[56] Thick No-stik (60 μm) and Emralon-333 (13 μm) coatings maintained excellent dropwise behavior after the long-term test (>16,000 hours), while most of the thinner (0.5-3 μm) coatings exhibited poor dropwise mode eventually, even if the durability of Fluoroacrylic (>16,000 hours, 2-3 μm), Parylene-D (>12,000 hours, 0.5-1 μm) and Parylene-N (<4,000 hours, 0.5-1 μm) are desirable. Interestingly, thicker

coatings in this work were not always more robust during condensation: 1 μm Parylene-D failed within 100 hours, while 0.5 μm Parylene-D survived for over 12,000 hours on copper, copper-nickel and titanium substrates.[56] This demonstrates the lack of consistency in coating quality. Similarly, Holden *et al.* showed that thick No-stik (60 μm), Emralon-333 (20 μm), Fluoroepoxy (1-10 μm) and Fluoroacrylic (1-10 μm) coatings sustained good dropwise condensation after >20,000 hours on the same metal substrates; while thinner coatings such as Nedox (5 μm, <1,000 hours), Pepco 6122 (5-10 μm, >2,000 hours), Isonel (5-10 μm, <24 hours), sputtered PTFE (0.4 μm, 2,000 hours) and Silicone (unknown thickness, <50 hours) are not as good.[55] Edwards and Doolittle coated 25.4 μm PFTE (nominal thickness) on copper, and the durability reported is 30 days with the HTC enhancement of 240-330%.[119] Ma and Wang reported 500 hours of continuous condensation and 1,000 hours of periodic condensation for PTFE coatings deposited on copper and stainless steel.[120] The 40 nm thick poly-(1H,1H,2H,2H-perfluorodecyl acrylate)-co-divinyl benzene (or p(PFDA-co-DVB)) coating deposited on copper surface by Paxson *et al.* demonstrated good dropwise mode for 48 hours without any decrease in HTC.[121] A 220-250 nm thick sol-gel coating with methyl triethoxysilane and tetraethyl-orthosilicate deposited on aluminum by Parin *et al.* failed within 3 hours of water vapor condensation.[122] Available durability tests of polymers promoting dropwise condensation are summarized in Table 1.

Table 1. Durability of common polymer coatings during water vapor condensation.

Coating	Substrate	Thickness (μm)	Durability (hr)	Reference
No-stik	Cu, CuNi	60	>18,000	
Emralon-333	Ti	13	>16,000	
Fluoroacrylic	Cu, Ti	2-3	>16,000	56
Parylene-D	Cu, Ti, CuNi	0.5, 1	>12,000	
Parylene-N	Cu, CuNi	0.5, 1	<4,000	
No-stik	Ti, CuNi	60	>22,000	
Emralon-333	Ti	20	>22,000	
Fluoroacrylic	Cu, Ti, CuNi	1-10	>20,000	
Fluoroepoxy	Ti	1-10	>22,000	
Pepco 6122	Cu, Ti, CuNi	5-10	>2,000	55
Nedox	Ti	5	<1,000	
Isonel	Cu, Ti, CuNi	5-10	<24	
Sputtered PTFE	Cu	0.4	<48	
Silicone	Cu	Unknown	<50	
PTFE	Cu	25.4	720	119
PTFE	Cu, SS	Unknown	1,000	120
p(PFDA-co-DVB)	Cu	0.04	48	121
Tetraethyl-orthosilicate with methyl triethoxy silane	Al	0.22-0.25	3	122

2.2.2 Self-assembled Monolayers (SAMs)

As a rule of thumb, a thinner low surface energy coating will facilitate higher enhancements in heat transfer performance,[54] thus self-assembled monolayer (SAMs) coatings are expected to be promising candidates to enhance condensation heat transfer, since the thickness of such coatings are typically <10 nm, depending on the monolayer structure or multilayer structure determined by the synthesis process.[67, 68, 123] Although self-assembled monolayers have been studied extensively as a promoter coating for dropwise condensation of steam,[13, 32, 47, 62-64, 88, 124] unlike polymer coatings, there is limited data on its durability during condensation (*i.e.*, the lifetime of promoting DWC).

Paxton *et al.* coated trichloro(1H,1H,2H,2H-perfluorooctyl) silane (or TFTS) on an aluminum substrate and demonstrated that the coating failed (*i.e.*, a transition to FWC) in ≈30 mins during condensation of saturated steam at 100 °C with the aluminum surface at 30 °C.[121] Preston *et al.* reported that the same TFTS coating on a copper surface degrades within 12 hours during water vapor condensation at 100 °C with a 5 °C subcooling (*i.e.*, the copper surface was at 95 °C).[125] Yang and Gu deposited a 3 nm docosanoic acid SAMs coating on copper and achieved the durability over a week.[126] Bonner demonstrated that heptadecafluoro-1-decanethiol coated on oxidized copper and gold plated copper promoted dropwise condensation for over 9 months, however, only initial heat transfer performance were reported.[49] Vemuri *et al*. coated n-octadecyl thiol SAMs on copper tubes, and the modified surface promoted good dropwise condensation for over 2,600 hours with the subcooling varying from 1-4 °C.[127] Even though DWC was maintained for ≈2,600 hours, the static contact angle decreased from 148° to 111°, which

indicated that the coating was degrading during condensation. They also noticed that the heat transfer coefficient decreased from ≈3× (compared to filmwise condensation) at ≈100 hours to ≈1.8× at ≈2,600 hours. Chang *et al.* demonstrated that an n-octadecyl mercaptan (octadecanethiol) SAM coated on a copper tube ceased to promote dropwise behavior after ≈2 days when condensing steam at 100°C with a 20°C substrate subcooling and in the presence of non-condensable gases (NCGs).[36] The only other known study on the durability of SAMs during condensation of water vapor was by Blackman *et al*.[59, 60] They showed good dropwise condensation over 500 hours for 16 different alkyl chain compounds, including n-octadecyl thiol, on copper and copper alloy surfaces, and this is the only known study that has demonstrated some level of coating durability, however, they did not report any heat transfer measurements.

Another desirable feature for low surface energy coating enhanced heat transfer is that the low contact angle hysteresis contributes to faster droplet shedding during condensation.[9, 48] Several studies investigated developing ultra-smooth SAM coatings in order to obtain a thin monolayer coating (<2 nm), instead of thicker multilayers up to 10 nm, because conformal coatings most likely lead to low contact angle hysteresis (less droplet pinning from coating defects). Wang and Lieberman deposited octadecyltrichlorosilane (OTCS) on silicon in a dry environment with the mixture of chloroform ($CHCl_3$), carbon tetrachloride (CCl_4) and Isopar-G fluid and dried with activated alumina, and obtained a RMS roughness ≈0.1 nm (2 μm × 2 μm).[128] Similarly, Wang *et al.* deposited OTCS in a dry box (water concentration <1 ppm) and attained a RMS roughness <0.05 nm based on line scans.[129] Equivalent level of coating roughness

was achieved by Ito *et al.* with OTCS and octadecyltrimethoxysilane (OTMS) deposited on silicon in chlorobenzene and toluene.[130] Lessel *et al.* also achieved excellent low roughness (<0.17 nm) for OTCS, hexadecyl-trichlorosilane (HTCS) and dodecyltrichlorosilane (DTCS) on silicon in a mixture of bicyclohexyl (BCH) and carbon tetrachloride.[131] Nevertheless, none of these ultra-smooth SAMs work have reported any heat transfer performance and the robustness during water vapor condensation. Available durability tests of SAM coatings promoting dropwise condensation are summarized in Table 2.

Table 2. Durability of common self-assembled monolayer (SAMs) coatings during water vapor condensation.

Coating	Substrate	Durability (hr)	Reference
Trichloro(1H,1H,2H,2H-perfluorooctyl)silane (TFTS)	Al	0.5	121
TFTS	Cu	12	125
docosanoic acid	Cu	3	126
heptadecafluoro-1-decanethiol	Cu, AuCu	6,480	49
n-octadecyl thiol	Cu	2,600	127
n-octadecyl thiol	Cu	500	59, 60
octadecanethiol	Cu	48	36

2.2.3 Slippery Liquid-Infused Porous Surfaces (SLIPS)

As discussed in Section 2.1.5, a number of researches have investigated crafting novel micro-/nanostructures,[103, 105, 108, 113, 114, 132] creating optimal liquid-lubricant combinations,[101, 102] and promoting dropwise condensation of low surface tension liquids

with SLIPS,[26, 117, 118] however, there are only a handful of papers reporting the durability of SLIPS when condensing water vapor in the dropwise mode. Weisensee *et al.* discovered that a low viscosity lubricant (12 cSt) experiences a relatively fast oil depletion ≈1 hour when condensing water vapor, while high viscosity lubricants (>140 cSt) can last over 10 hours.[133] Preston *et al.* observed the SLIPS transition to filmwise condensation within 1 hour when condensing toluene with the presence of NCGs (30 Pa), and the heat transfer coefficient degraded by 78% in the complete filmwise mode after ≈3 hours.[26] Sett *et al.* demonstrated good dropwise condensation of ethanol and hexane for 7 hours with a higher viscosity lubricant (>250 cSt), and NCGs are believed to exist (starting pressure ≈4 Pa, leak rate≈0.1 Pa/min) although claimed eliminated.[118] Adera *et al.* obtained the SLIPS durability of 3-4 hours repeatedly (>20 experiments) with inverse opal structures during condensation of water vapor.[132]

2.3 Promoter Degradation Mechanisms during Condensation

Given the limited lifetime promoting efficient dropwise condensation than what is desired in industries, studying the durability of these promoters, and more importantly the potential mechanisms for degradation, could contribute to overcoming this barrier to industrial applications. The failure mechanisms of SLIPS[134-136] and jumping droplet mode[32, 64] are well identified in literature, however, there have not been any significant advancements and validated methodologies in extending the lifetime other than using a non-cloaking lubricant and operating at lower subcoolings for SLIPS and the jumping droplet mode, respectively. Additionally, despite the extensive body of literature on

utilizing low surface energy coatings to enhance condensation *via* the traditional dropwise mode, jumping droplet mode, hybrid surfaces and SLIPS, there is little-to-no mechanistic understanding of how these low surface energy coatings (*i.e.*, polymers and SAMs) degrade and how to extend their lifetime.

2.3.1 Polymers

Marto *et al.* claimed that the durability of organic coatings to promote dropwise condensation depends on the molecular structure and roughness of the coating material, substrate roughness level and chemical activity of the substrate metal.[56] Oxygen diffusion through thin coatings exposes the substrate to a corrosive environment, which explains their observation of the substrate color change (bright to dark) on copper, brass and copper-nickel surfaces while good dropwise condensation was maintained. However, this explanation was not always well supported by their experiments (*i.e.*, no obvious difference shown on the reactive copper and less reactive titanium coated with fluoroacrylic).[56] Holden *et al.* made a similar conclusion that the chemical or electrochemical reactions at the coating interface, such as copper oxidation, change the adhesion of coatings, since the No-stik coated copper and brass substrates were speckled with green after condensing water vapor for 22,000 hours, and the Nedox coated copper-nickel turned noticeably dark after 24 hours of condensation.[55] Recently, Ma *et al.* created artificial pinholes by nanoindentation on the amorphous Teflon coating to expose the hydrophilic silicon substrate, and they experimentally showed that water vapor preferentially nucleates on those pinholes and condensed droplets grow from the

pinholes.[137] They concluded that the capillary pressure of the condensed water/blister generated by the pinned liquid-vapor interface delaminates the polymer coating from the pinholes. However, those artificial pinholes are normally different from typical defects on polymer coatings (*i.e.*, non-uniform coating), since nanoindentation may damage the coating-substrate interface by pushing the polymer aside.

2.3.2 Self-assembled Monolayers (SAMs)

Yang and Gu reported a similar color change as shown in Marto *et al.*[56] from light gray to black on a copper tube coated with docosanoic acid SAMs as continuous condensation goes on, but this observation was not explained or discussed in the work.[126] Luo *et al.* sprayed water droplets on octadecanethiol coated ZnO nanowire structures, and there were dried deposits left on the surface after droplet evaporation, resulting in the lower receding contact angle.[138] They claimed that the droplets destroy the coating by peeling off the adsorbed coating layer and leaving dried deposits of thiols during evaporation, however, those deposits were not verified to be the thiols and no detailed clarifications were included in their double-layer coating assumption. The only known work proposing the degradation mechanism of SAMs was reported by Pellerite *et al.* with the fluorinated trichlorosilane coating deposited in water-saturated heptane solution on silicon.[139] The receding contact angle reduced by ≈10-20° after storing the coated surface in a 100% relative humidity environment for 1-2 weeks, while storing the same samples in a 0% relative humidity did not change the contact angles. They proposed that water penetrates the monolayer film, which is hydrolyzed with adsorbed water on the surface,

and replaces the Si-OH bonds at the coating-substrate interface. Nevertheless, the SAMs coating they deposited in a water-saturated solvent was initially a multilayer (thickness≈4.5 nm) instead of the monolayer (thickness≈1.5 nm), and cross-linking of silane molecules would occur before bonding to the substrate due to the presence of moisture.[67, 139]

2.3.3 Failure Modes of Other Enhancement Techniques

Lubricant depletion during droplet shedding is regarded as the primary failure mechanism of SLIPS during condensation.[26, 97, 103, 113] Wexler *et al.* characterized the lubricant depletion with fluorescence imaging and showed that the lubricant drainage is caused by the shear stress from the external flow.[136] Their analytical model revealed that the steady state oil retention depends on the surface tension, contact angle and the geometry/aspect ratios of the microstructure, so that the lubricant depletion can be reduced by optimizing the textured surface and the lubricant. They also extended the work to study both shear-driven and gravity-driven drainage with different liquids at different length scales.[135] Liu *et al.* analyzed SLIPS in a similar longitudinal groove and proposed that less viscous lubricants lead to higher retention for a given external fluid.[134] However, Weisensee *et al.* reported reduced lubricant depletion with higher viscosity lubricant during water vapor condensation.[133] Preston *et al.* and Sett *et al.* suggested that choosing proper non-cloaking lubricant can minimize the shear stress induced lubricant drainage.[101, 102]

As for the jumping droplet mode, though a higher condensation HTC than the traditional dropwise mode is achieved, it is known to sustain only lower subcoolings: condensate flooding and the formation of pinned Wenzel droplet morphologies induced by higher subcoolings or supersaturations leads to the degradation of the jumping droplet mode and hence the significantly reduced heat transfer performance.[32, 90, 140, 141] Miljkovic *et al.* demonstrated that the surface flooding with pinned Wenzel droplets occurs within 30 seconds of water vapor condensation at the higher supersaturation (S=1.54, logarithm mean temperature difference =12°C, vapor temperature ≈2.7 kPa), while no flooding was observed at the lower supersaturation (S=1.08, logarithm mean temperature difference =4°C, vapor temperature ≈2.7 kPa).[32] They further showed the criterion for surface flooding that S=1.12 is the critical supersaturation (*i.e.*, flooding occurs at S>1.12) and the condensation HTC is degraded by 40% compared to the smooth hydrophobic condenser surface. Note that the corresponding critical subcooling at this critical supersaturation is 1.8°C when the vapor temperature is ≈2.7 kPa (saturation temperature at 22.3°C). Since then, several work investigated delaying or minimizing condensate flooding by optimizing the micro-/nanotextured substrates.[22, 89, 90, 93] Ölçeroglu and McCarthy created patterned hydrophilic islands on the hydrophobic surface to achieve preferential nucleation, so that the jumping droplet mode transitions to gravity-driven droplet shedding, instead of flooding the surface, at the higher supersaturation (S=1.54).[90] Similarly, Lo *et al.* fabricated a hybrid surface with hydrophobic nanowires and hydrophilic microchannels to guide condensate removal *via* dragging and sliding at higher subcoolings (8°C to 18°C).[22] Wen *et al.* further pushed the

boundary of the subcooling in the jumping droplet mode to 28°C by depositing TFTS on a uniform 3D copper nanowire network.[93] However, the presence of NCGs in the above two work (*i.e.*, leak rate at 24 Pa/hr from Lo *et al.* and 300 Pa NCGs from Wen *et al.*) in the system may lead to an overestimation of the actual subcooling,[115, 142, 143] since previous studies showed that the liquid-vapor interface temperature decreases to almost the cold wall temperature in the presence of 2% NCGs due to the diffusion barrier formed by accumulation of NCGs.[116, 143] Recently, Seo *et al.* optimized the textured substrate with a finer nanostructure and a more uniform coating, and they displayed the jumping droplet mode at the low supersaturation (S=1.03) and the good dropwise mode at higher supersaturations (S=1.2 and 1.8) without flooding.[89] Besides the condensate flooding at higher subcoolings, the jumping droplet mode fails once the low surface energy coatings degrade, which were discussed in Sections 2.3.1 and 2.3.2.

2.3.4 Summary on Degradation Mechanisms

A number of research works have focused on developing new coating materials for water/moisture repelling applications such as self-cleaning, anti-frosting/icing, and anti-fouling, and many works have demonstrated enhanced condensation heat transfer performance with low surface energy coatings, however, there are only a handful of research studies looking into understanding the condensation-mediated degradation mechanism and extending the lifetime of these coatings to promote efficient dropwise condensation. Lubricant depletion by shear stress is regarded as the primary failure mechanism of SLIPS. Degradation of polymer coatings during water vapor condensation

is suggested to be the oxygen diffusion through thin polymer coatings and a subsequent oxidation reaction at the coating-substrate interfaces. Evaporation induced degradation and moisture driven failure of SAMs coatings are proposed, however, there have not been any experimental validations for these proposed mechanisms.

2.4 Other Novel Condensation Enhancement Techniques

Besides the techniques discussed above, there are some recent advancements in enhancing water vapor condensation with novel methods in terms of coating materials[36, 144] and textured substrate structures.[54, 145-147] Oh *et al.* coated decomposed hydrophobic polyimide on a thin (<10 μm) nickel inverse opal nanostructure to promote filmwise condensation within the porous media, in which mode the droplets nucleate on the hydrophobic coating in the dropwise mode and wick into the hydrophilic porous structure.[145] Instead of depositing the low surface energy coatings, Wilke *et al.* developed a nanoscale reentrant cavity surface to repel water by preventing the nucleating droplets from spreading within the porous structure and forming Wenzel droplets.[146] Though it is shown to remain water repellent during condensation, local transition to Wenzel state (*i.e.*, individual cavity cells get wetted) is inevitable and irreversible, so that the surface failure occurs once a majority of the cavities are occupied by the condensate droplets. Cha *et al.* created a hydrophilic surface with 2-[methoxy(polyethyleneoxy)6-9propyl] trimethoxysilane and demonstrated dropwise condensation of water vapor with low contact angle hysteresis (θ_{adv}≈38°, θ_{rec}≈35°, CAH ≈3°), showing the potential to enhance heat transfer performance by faster droplet shedding (low CAH) and low thermal

resistance from droplets (low CA) on a hydrophilic surface.[148] Budakli *et al.* utilized 3-(triethoxysilyl)propyl isocyanate as an adhesion layer to deposit a polymer coating of perfluoro alcohol ($C_6F_{13}OH$, or PFA) around 270-780 nm thick, and this SAMs-polymer mixture coating exhibits a 16% HTC enhancement (compared to an uncoated copper surface) for 40 days without degradation.[149] Wilke *et al.* infused PTFE into nanostructures of a high thermal conductivity material to create a high thermal conductance thick (≈1.5 μm) composite layer, achieved a 700% condensation HTC enhancement over an uncoated surface, and maintained the dropwise mode for over 200 days.[54] They further demonstrated the self-repairing property of the composite by heating the damaged surface up to the polymer melting point to recover the hydrophobicity. Similar self-healing property was reported by Ma *et al.* with a vitrimer coating (thickness from 10 nm to 4 μm) on silicon, aluminum and copper surfaces made by mixing boric acid with polydimethylsiloxane (PDMS).[144] This coating promoted stable dropwise condensation for 17 days in the ambient condition, instead of a pure vapor environment, and heat transfer measurements were not reported. Preston *et al.* deposited a single layer graphene coating on copper surfaces *via* low-pressure chemical vapor deposition (LPCVD) and atmospheric pressure chemical vapor deposition (APCVD) to promote dropwise condensation, and achieved 4× higher heat transfer coefficient compared to the filmwise mode.[125] This graphene coating did not degraded over 336 hours of continuous condensation of water vapor. Similarly, Chang *et al.* deposited a few layers of graphene on nickel and copper to promote dropwise condensation with a contact angle hysteresis ≈40°.[36, 150] In the presence of a large amount of non-condensable gases (3.56% to 6.84%),

the graphene coated copper failed within 2 days, while the nickel surface coated with few-layer graphene maintained good dropwise for 36 months. The heat transfer coefficient they obtained on the graphene coated nickel surface in the absence NCGs was ≈2× higher than the filmwise mode, however, the HTC was close to the filmwise Nusselt model when a large amount of NCGs are included.[36]

2.5 Chapter Summary

This chapter summarizes the major advancements and challenges in enhanced liquid-vapor phase change heat transfer over the past few decades. A number of these enhancement techniques involve thin low surface energy coatings, however, the incapability of repelling low surface tension liquids and the deficient coating robustness during phase change processes are the primary limitation to industrial application of these well studied hydrophobic coatings. In this work, we present two methods (*i.e.*, surface geometry and surface energy) to overcome these obstacles and provide durable solutions to enhanced heat transfer applications. The surface geometry method leverages micro-/nanostructure materials/surfaces to optimize the contact between the liquid/vapor and the solid, enabling the improvement in heat transfer performance with an increased effective thermal conductivity for various low surface tension liquids. The surface energy method modifies the surface energy to promote long-term efficient dropwise condensation, which is facilitated by developing robust ultra-thin low surface energy coatings through an understanding of the degradation mechanism of thin coatings. The

surface geometry method and the surface energy method are presented in Chapter 3 and Chapter 4, respectively.

CHAPTER III

SURFACE GEOMETRY METHOD*

In this chapter, we present a unified framework for the modeling of steady liquid-vapor phase change processes in porous media, incorporating local liquid-vapor interfacial effects in terms of the local permeability and meniscus shape, which can be applied to modeling both condensation and evaporation heat transfer on/from porous materials to predict the condensation enhancement and the evaporation dry-out heat flux. When applying this model to condensation, we demonstrate a robust and scalable condensation enhancement method (capillary-enhanced filmwise condensation) where a high heat transfer coefficient is achieved by leveraging capillary forces within a high thermal conductivity porous wick to promote condensate removal. The capillary pressure is supported by a pump to sustain steady condensate removal, and the high thermal conductivity of the wick decreases the overall thermal resistance. This technique is capable of enhancing condensation heat transfer performance for both water and low surface tension fluids. When applying this model to evaporation, we accurately predict the dry-out heat flux for thin-film evaporation from micropillar arrays by obtaining a precise pressure profile and incorporating the local meniscus shape/curvature in discretized model cells. A permeability submodel with high accuracy is validated with CFD simulations, and the prediction on dry-out heat flux is verified with available

* Reprinted with permission from "Unified Modeling Framework for Thin-Film Evaporation from Micropillar Arrays Capturing Local Interfacial Effects" by Wang, R., Jakhar, K. and Antao, D.*, 2019. *Langmuir*, 35(40): p. 12927-12935., Copyright 2019 by American Chemical Society

* Reprinted with permission from "Capillary-Enhanced Filmwise Condensation in Porous Media" by Wang, R. and Antao, D.*, 2018. *Langmuir*, 34(46): p. 13855-13863., Copyright 2018 by American Chemical Society

experimental data from the literature. The unified modeling framework reported in this chapter is an accurate non-CFD-based methodology for modeling steady liquid-vapor phase change processes (*i.e.*, evaporation and condensation) in porous media, and can be utilized to optimize the design of porous media in phase change heat transfer applications.

This chapter includes a general modeling framework for flow through porous media capturing local meniscus shape, and the model applications in capillary-enhanced filmwise condensation and thin-film evaporation from micropillar arrays. Additional unpublished results from the condensation model predictions are currently under review:

1. Wang, R. and Antao, D.*, "Effect of Meniscus Curvature on Phase-Change Performance during Capillary-Enhanced Filmwise Condensation in Porous Media ". (*In Review*)

3.1 Modeling Fluid Flow through Porous Media

3.1.1 Governing Equations, Velocity Profiles and Pressure Profiles

In this section, we present a one-dimensional semi-analytical modeling framework for the prediction of phase-change heat transfer (evaporation and condensation) during capillary driven flows in porous media *via* accurate predictions of the spatially varying velocity and non-linear pressure drop. For the purpose of modeling, a micropillar array is used to simplify the model due to the uniform geometric parameters such as porosity ε and permeability κ. Specifically, we consider a porous wick of length L that is comprised of microscale pillars of diameter d, pitch l and height (or thickness) t arranged in a square pattern, and the overall model geometry is schematically shown in Figure 1 with the flow

direction being in the *x* coordinate direction. The blue, red and yellow arrows indicate the directions of evaporation, condensation, and the liquid flow, respectively. In the case of condensation, the porous media fills up with the condensate at steady state, and the condensate removal is enabled by the capillary pressure and a pump connected to the end of the wick acting as an external force. While in the case of evaporation, the beginning of the micropillar array is attached to a liquid reservoir to supply liquid. Due to interactions between the liquid condensate and solid wick material in the micro/nanoscale pores, a curved liquid-vapor interface (or meniscus) is formed[151-155] with the liquid pressure being lower than the vapor pressure for a wetting liquid. The effect of meniscus curvature on the condensate flow area is neglected in this section due to the assumption of constant permeability, and will be considered in Section 3.1.3 with an improved model.

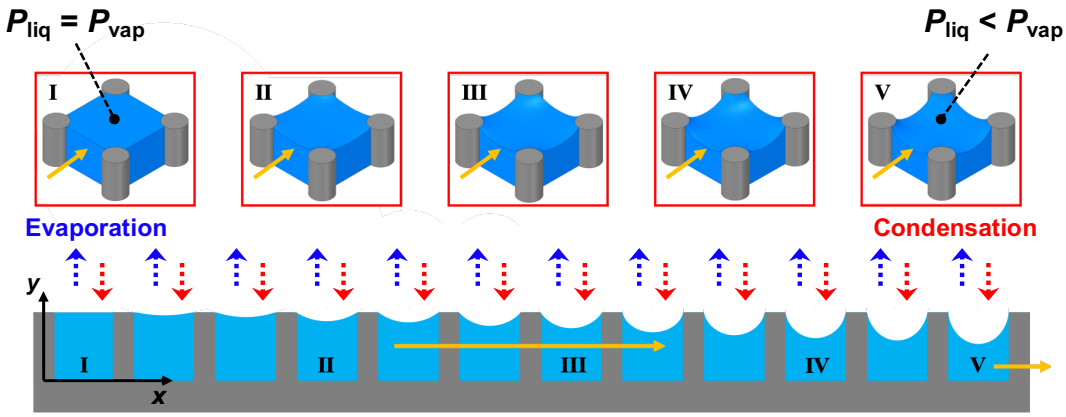

Figure 1. Schematic of the model geometry and simulation domain showing a side view of the physical domain in the current model and isometric views of unit cells (fluid region bounded by four micropillars) at different spatial locations with various meniscus curvature/contact angles. Reprinted from Wang *et al.*, Langmuir, 2019.

The velocity of the liquid flow through the wick is obtained by solving a form of the Brinkman equation with physical velocity as follows:[156]

$$\mu\frac{\partial^2 u}{\partial y^2}-\frac{\mu\cdot\varepsilon}{\kappa}u-\frac{\mathrm{d}P}{\mathrm{d}x}+\rho\cdot g=0 \tag{3.1}$$

where, μ is the dynamic viscosity of the fluid, u is the local x direction *physical* velocity in the wick, κ is the wick permeability and P is the local pressure. Note that this equation is in a form incorporating the *physical* velocity and can be derived from a simplification of the Navier-Stokes momentum equation, however, most traditional formulations of the Brinkman equation use the *superficial* velocity.[152, 156-160] We use this formulation with the physical velocity (as opposed to the superficial velocity) to maintain consistency between the various sub-models and for comparisons with CFD simulation predictions which are in the form of the physical velocity. The above equation is solved between the boundaries of no-slip at the bottom wall ($y = 0$) and no-shear stress at the top ($y = t$) of the wick:

$$\begin{aligned} &u=0,\ \text{at } y=0\\ &\frac{\partial u}{\partial y}=\frac{\mu_{\text{vapor}}}{\mu},\ \text{at } y=t \end{aligned} \tag{3.2}$$

where, μ_{vapor} is the viscosity of the vapor phase. The solution is found to be:

$$u=-\frac{\kappa}{\mu\cdot\varepsilon}\left(\frac{\mathrm{d}P}{\mathrm{d}x}-\rho\cdot g\right)\left(1-e^{-\sqrt{\frac{\varepsilon}{\kappa}}y}\right) \tag{3.3}$$

Averaged over the thickness of the wick, the average cross-sectional velocity ($\bar{u}$) of the condensate through the wick is:

$$\bar{u}=-\frac{\kappa}{\mu\cdot\varepsilon\cdot t}\left(\frac{\mathrm{d}P}{\mathrm{d}x}-\rho\cdot g\right)\left(t-\sqrt{\frac{\kappa}{\varepsilon}}+\sqrt{\frac{\kappa}{\varepsilon}}e^{-\sqrt{\frac{\varepsilon}{\kappa}}t}\right) \tag{3.4}$$

where, $\mathrm{d}P/\mathrm{d}x$ is the gradient in the pressure (∇P) along the wick and is negative in value.

To estimate the value of $\bar{u}$ (and finally the rate of condensation via a mass-energy balance), the pressure profile in the wick is required. We obtain this pressure profile from the conservation of mass in the wick for the incompressible condensate:

$$\frac{\partial u_{\mathrm{x}}}{\partial x}+\frac{\partial u_{\mathrm{y}}}{\partial y}=0 \tag{3.5}$$

where, u_{x} and u_{y} are the x and y direction velocities. The y direction velocity is assumed to be the liquid volumetric flux, v_{cond} and v_{evap} for condensation and evaporation, respectively. The resulting equation in terms of the pressure is:

$$\frac{\mathrm{d}^2 P}{\mathrm{d}x^2}=-\frac{\mu\cdot\varepsilon}{\kappa}\frac{v_{\mathrm{cond/evap}}}{\left(t-\sqrt{\frac{\kappa}{\varepsilon}}\left(1-e^{-\sqrt{\frac{\varepsilon}{\kappa}}t}\right)\right)}=-A \tag{3.6}$$

We solve for the pressure profile based on the expected Laplace pressure within the liquid at the entrance and exit of the wick.

For condensation, the exit pressure is determined by the capillary pressure since a pump was used to remove condensate from the micropillar array:

$$\begin{aligned} P&=0,\ \text{at } x=0\\ P&=P_{\mathrm{cap}},\ \text{at } x=L \end{aligned} \tag{3.7}$$

where, P_{cap} is the maximum capillary pressure that can be generated by the wick geometry and is given by:[151, 152, 155]

$$P_{\mathrm{cap}}=-\frac{\gamma_{\mathrm{lv}}\cdot p_{\mathrm{pore}}\cdot\cos\theta_{\mathrm{rec}}}{a_{\mathrm{pore}}} \tag{3.8}$$

where, γ_{lv} is the surface tension of the condensate, θ_{rec} is the receding contact angle of the condensate on the wick surface material, and p_{pore} and a_{pore} are the wick pore perimeter

and projected/cross-sectional area respectively. The resulting pressure gradient and profile are:

$$\nabla P = \frac{\mathrm{d}P}{\mathrm{d}x} = -\frac{A}{2}\left(2 \cdot x - L\right) + \frac{P_{\mathrm{cap}}}{L}$$
$$P = -\frac{A}{2}\left(x^2 - L \cdot x\right) + \frac{P_{\mathrm{cap}}}{L} x \tag{3.9}$$

For evaporation, similarly the pressure at the entrance of the wick exhibits zero pressure (relative to the vapor pressure above it) due to the connection with the liquid reservoir, however, the boundary condition at the exit is zero pressure gradient assuming liquid dry-out occurs at the end of the micropillar array at steady state:

$$P = 0, \text{ at } x = 0$$
$$\frac{\partial P}{\partial x} = 0, \text{ at } x = L \tag{3.10}$$

The resulting pressure gradient and pressure profile are:

$$\nabla P = \frac{dP}{dx} = A\left(x - L\right)$$
$$P = \frac{A}{2} x^2 - AL \cdot x \tag{3.11}$$

As can be seen from eq. 3.9 and eq. 3.11 above, the pressure profile is unaffected by gravity, however, the velocity profile from eq. 3.4 (and hence v_{cond} and v_{evap} from energy/mass conservation) will depend on whether gravity is accounted or neglected in the analysis.

3.1.2 Discretization & Iteration for Condensation and Evaporation

Both pressure profiles above have two unknowns, hence, in order to estimate the rate of condensation/evaporation (v_{cond} and v_{evap}), we discretize the wick (x direction) into a large number of elements and iterate to obtain a converged solution. The number of discretized elements needs to be sufficiently large to assume a linear pressure drop across one discretized element. The 3D view of a discretized modeling unit cell is shown in Figure 2a, and for the i^{th} discretized cell:

$$\bar{u}_i = -\frac{\kappa}{\mu \cdot \varepsilon \cdot t}\left(\nabla P_i - \rho \cdot g\right)\left(t - \sqrt{\frac{\kappa}{\varepsilon}} + \sqrt{\frac{\kappa}{\varepsilon}} e^{-\sqrt{\frac{\varepsilon}{\kappa}}t}\right) \tag{3.12}$$

where, $\bar{u}_i$ is the average liquid velocity at the outlet of the discretized element i and ∇P_i is the gradient in pressure across the discretized element i. For the first iteration, the pressure gradient across the wick length is assumed to be linear (or P_{cap}/L) and this linear pressure gradient is used to obtain the local condensate velocity $\bar{u}_i$. Balancing the mass into and out of each element as shown in Figure 2b, we then obtain the condensation/evaporation volumetric flux v_{cond}/v_{evap}:

$$\begin{aligned} \bar{u}_{i-1} \cdot t + v_{cond} \cdot \frac{L}{N} &= \bar{u}_i \cdot t \\ \bar{u}_{i-1} \cdot t &= v_{evap} \cdot \frac{L}{N} + \bar{u}_i \cdot t \end{aligned} \tag{3.13}$$

This condensation/evaporation volumetric flux is assumed to be uniform for all discretized elements (assumption of uniform condensation and/or evaporation above the micropillar array) and is used to update the pressure gradient given in eqs. 3.9 and 3.11. The updated pressure gradient is then applied to recalculate the condensation/evaporation volumetric flux, and the process is repeated till convergence is achieved (variation of ≈0.1% for v_{cond}

and v_{evap}). Note, the convergence criteria for condensation and evaporation are different, because the two-phase change processes have different boundary conditions for the pressure profile, and the iteration procedure updates the pressure profile. In the case of condensation, the iteration stops once the pressure gradient at the beginning of the wick reaches a zero gradient:

$$\frac{\partial P}{\partial x} = 0, \text{ at } x = 0 \tag{3.14}$$

because of the low total flowrate of the condensate near the start of the micropillar array, and as the flowrate through the array increases along it length (mass addition *via* condensation), the local pressure gradient increases to accommodate this higher flow rate. In the case of evaporation, however, the convergence criterion is that the pressure at the end of the micropillar array reaches the maximum capillary pressure, P_{cap}:

$$P = P_{cap}, \text{ at } x = L \tag{3.15}$$

since the liquid-solid contact angle within a unit cell at the end of the wick is expected to be the receding contact angle during dry-out at steady state.

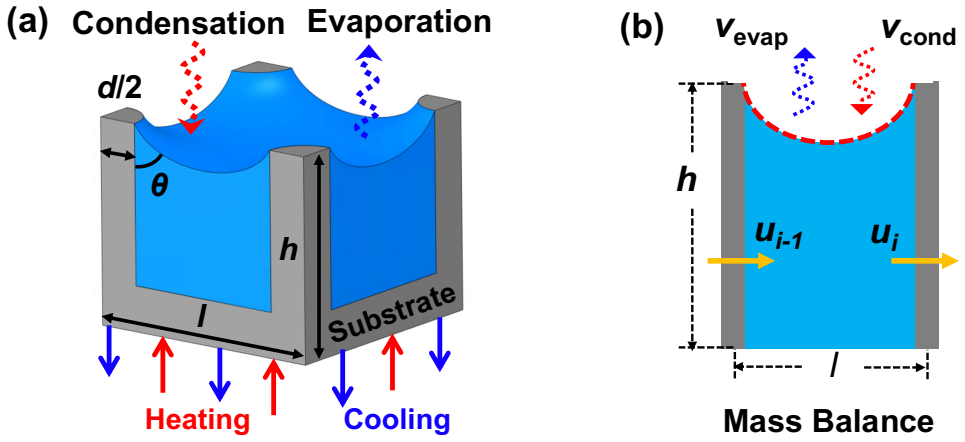

Figure 2. Schematic figures of (a) a 3D discretized modeling unit cell with meniscus curvature, and (b) the side view of the unit cell showing the mass balance. Reprinted from Wang *et al.*, *Langmuir*, 2019.

3.1.3 Local Meniscus Shape, Liquid Effective Height & Improved Framework

In literature, state-of-the-art analytical (or semi-analytical) models, including the model we reported in Section 3.1.2, assume a constant effective permeability over the porous wick and neglect the variation of the permeability (resulting from the changing meniscus curvature) along the length of the wick.[45, 145, 152, 159, 161, 162] However, for steady-state phase change processes (*i.e.*, evaporation and condensation) in a micropillar array, the liquid-vapor interface shape varies along the wick with the last unit cell having an interface with a higher curvature as compared to the first unit cell (previously shown in Figure 1). At the dry-out or maximum heat flux condition for evaporation and the capillary condensate removal condition for condensation, the contact angle of the liquid in the last unit cell is the receding contact angle,[151, 152, 155] while the meniscus in the first unit cell is nearly flat (contact angle with the micropillar side wall approaching 90°). This variation

in the local interface curvature (and resulting Laplace pressure difference) results from the viscous pressure loss being balanced by the Laplace pressure required to sustain the flow. In order to account for the local variation in the liquid-vapor interface and its effect on the micropillar array permeability, we captured the local meniscus curvature/shape for each individual cell after discretizing the modeling domain (*i.e.*, the micropillar array) into N elements (or unit cells, $N = L/l$) in flow direction as explained in Section 3.1.2.

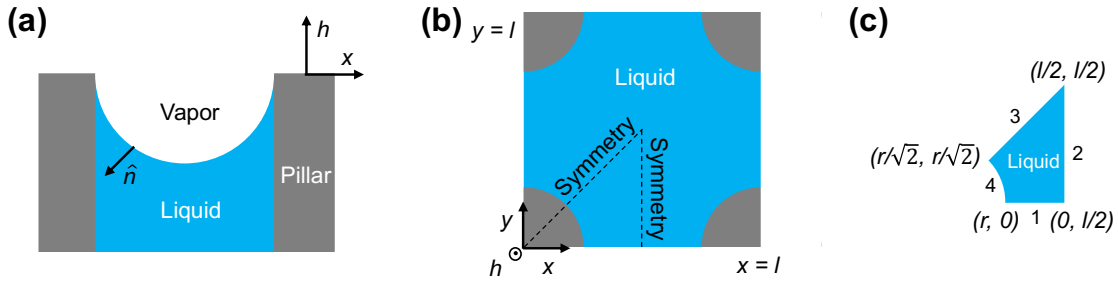

Figure 3. (a) Schematic side view of meniscus formed in the pillar arrays. (b) Top view of unit cell of a square-patterned cylindrical pillar array. (c) Problem domain for solving the meniscus shape.

The meniscus shape for a specific contact angle θ in a unit cell of pillars is simulated based on the model developed by Lu *et al.*[163] We denote the radius of pillars as r ($r = 1$, to normalize the pillar array dimension to its radius), center to center distance between pillars as pitch l, height h and establish a Cartesian coordinate system with center of one of the pillars as origin (Figure 3b). Considering symmetry of the meniscus shape we restrict the problem domain to 1/8th of the of the unit cell and define the meniscus shape by $h = f(x,y)$ (Figure 3c) which is obtained *via* the procedure outlined below. To obtain the meniscus shape as a function of the geometry, we need the boundary conditions for the geometry (1/8th unit cell) and the mean curvature of the meniscus. The average

contact angle around the pillar obtained through a force balance analysis. The vertical component of the line forces pulling the meniscus upwards is $\gamma_{lv} \cdot (2\pi r) \cdot \cos\theta$, where θ is the average contact angle around the micropillar and γ_{lv} is the liquid-vapor surface tension. The force is balanced by the downward component of the force from the pressure difference acting on the meniscus, $\Delta P^{lv} \cdot (l^2 - \pi r^2)$, where ΔP^{lv} is the pressure difference across the liquid-vapor interface of the meniscus. The force balance gives:[163]

$$\gamma_{lv} \cdot (2\pi r) \cdot \cos\theta = \Delta P^{lv} \cdot (l^2 - \pi r^2) \tag{3.16}$$

From the Young-Laplace equation:[15]

$$\Delta P^{lv} = 2 \cdot \gamma_{lv} \cdot K \tag{3.17}$$

where, K is the meniscus mean curvature, which is a constant for a unit cell. Combining the two equations above, we get:

$$\begin{aligned} K \cdot (l^2 - \pi r^2) &= \pi r \cdot \cos\theta \\ K &= \frac{\pi r \cdot \cos\theta}{l^2 - \pi r^2} \end{aligned} \tag{3.18}$$

K is obtained from the above equation for a specific value of θ and a specific geometry. Applying the concepts of differential geometry, the outward-pointing normal vector of the interface $\hat{n}$ (Figure 3a) can be determined from K:

$$\begin{aligned} \nabla \cdot \hat{n} &= 2K \\ \hat{n} &= \frac{\nabla f}{\|\nabla f\|} \end{aligned} \tag{3.19}$$

This equation governs the shape of the capillary surface $h = f(x,y)$. We solved this second order partial differential equation using the commercial software package MATLAB.[164] With the contact line fully pinned at the top of the pillar, we have Dirichlet condition

($h = 0$) on boundary 4 (*i.e.*, in contact with the pillar wall) and symmetric boundary conditions on boundaries 1, 2 and 3 (Neumann boundary condition set at 0). We used triangular meshes with quadratic elements while the relative tolerance for convergence was set to 10^{-6}. For $1/8^{th}$ of the of the unit cell, mesh with 20 boundary elements for boundary 4 was used (Figure 3c). The number of domain elements were scaled keeping the number of boundary elements constant for boundary 4. Table 3 contains the number of domain elements used for meniscus shapes for different *d/l* ratios.

Table 3. Quadratic domain elements for meniscus shape modeling with varying *d*/*l* ratios.

d/l	Domain elements
1.5	1033
2	2276
3	5856
4	10865
5	17385
6	25290
7	34605
8	45483
9	57644
10	71624

Figure 4a shows the trimetric view of the actual meniscus of the liquid-vapor interface in a discretized unit cell obtained by the model reported above. The transparent blue surface represents the actual meniscus area, while the red surface represents the projected area at the bottom, from which we define the area ratio, *AR*, where AR=1 for the first unit cell (*i.e.*, contact angle is 90°) and *AR*>1 for all other unit cells. Additionally, we define the local effective liquid height in the i^{th} discretized cell, h_i, by averaging the meniscus height along the center plane in the flow direction (Figure 4b). Note that given

the symmetry of the square geometry, the averaged meniscus heights are the same along the center planes in the flow direction and perpendicular to the flow direction, however, they are different for other geometries such as hexagonal and rectangular arrays. Both the area ratio and the local effective height are used in the improved mass balance (Figure 4c).

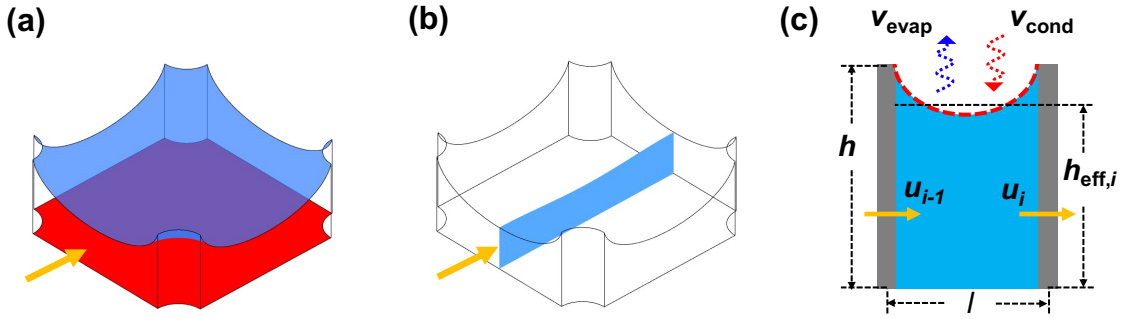

Figure 4. The trimetric views of (a) the actual meniscus area (transparent blue) of the liquid-vapor interface and the projected area (red), and (b) the unit cell depict the center plane in the flow direction used for obtaining the effective liquid height. (c) Schematic side view of one discretized unit cell with liquid effective height. Reprinted from Wang *et al.*, *Langmuir*, 2019.

A number of models for flow through micropillar arrays neglect the effect of the meniscus curvature and use a constant pillar height which leads to an over prediction in the heat flux due to a larger velocity resulting from a large permeability (or lower flow resistance).[159, 161, 162, 164-166] Byon and Kim[157] and Nam *et al.*[167] obtained correlations for the effective liquid height by fitting the results from Surface Evolver simulations, and Alhosani and Zhang[168] defined the effective height as the average of the pillar height and the minimum meniscus height based on a force balance on a projection of half of the interface. We use the center-plane in the flow direction for the average since the highest flow velocity is observed along that center plane and there is limited flow in the regions closest to the micropillar walls where the meniscus height approaches the micropillar

height. Here, we compare the current model (*i.e.*, center plane average in the flow direction) with the two models above with different definitions of the effective height for different geometric parameters (*i.e.*, diameter by pitch ratios, or d/l, and height ratios, or $h/(l\text{-}d)$) in Figures 5-9. The correlation developed by Byon and Kim[157] is intended to predict the effective height for any geometrical dimensions of micropillar array unit cell, since it has the contributions from micropillar diameter, pitch, height and liquid-solid contact angle. A first order test for accuracy of such a correlation should be that the effective height is equal to the micropillar height when the contact angle is 90° (Figures 5-9), however, this is not the case for the correlation provided by Byon and Kim.[157] The approach of Alhosani and Zhang[168] where an average of the micropillar height and the minimum meniscus height simplifies the analysis, however there are two requirements: (a) an accurate prediction of the meniscus shape is required, and (b) the contact angle is sufficiently high (*i.e.*, for a low contact angle, most of the liquid flow occurs near the minimum meniscus height and a simple average of the minimum meniscus height and the micropillar height over predicts the effective micropillar array height).

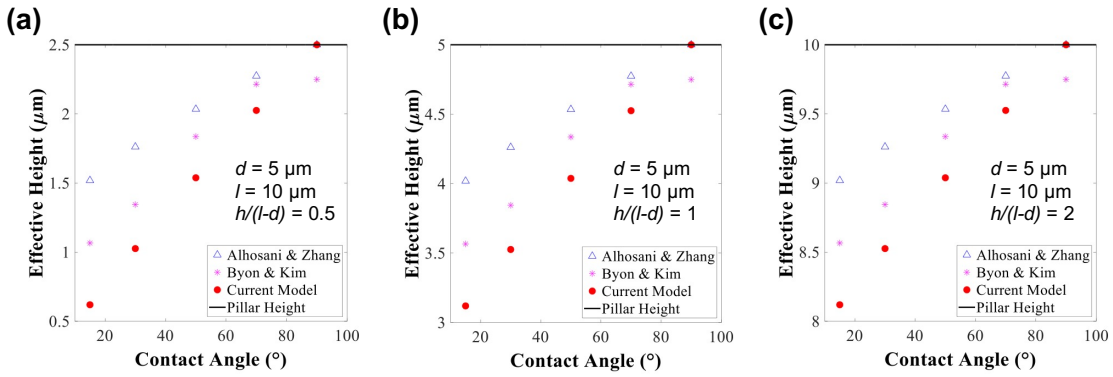

Figure 5. Comparison of the effective liquid heights from different models for d = 5 μm, l = 10 μm; $h/(l\text{-}d)$ = 0.5, 1 and 2.

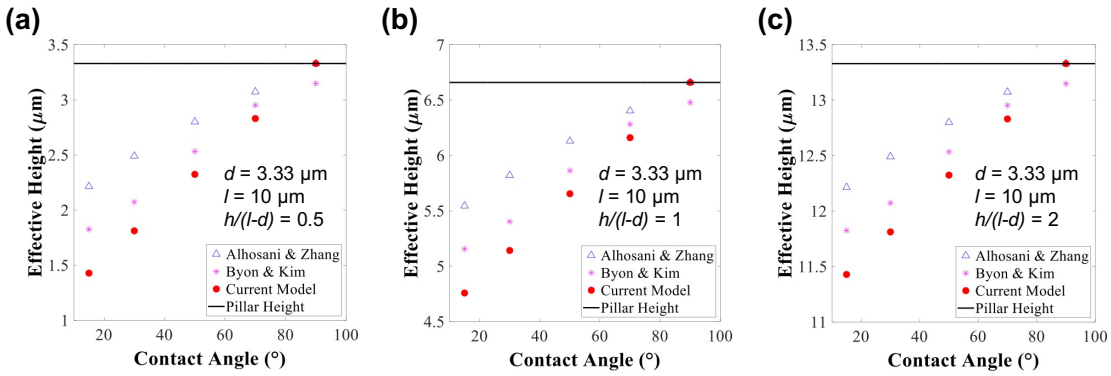

Figure 6. Comparison of the effective liquid heights from different models for d = 3.33 μm, l = 10 μm; $h/(l-d)$ = 0.5, 1 and 2.

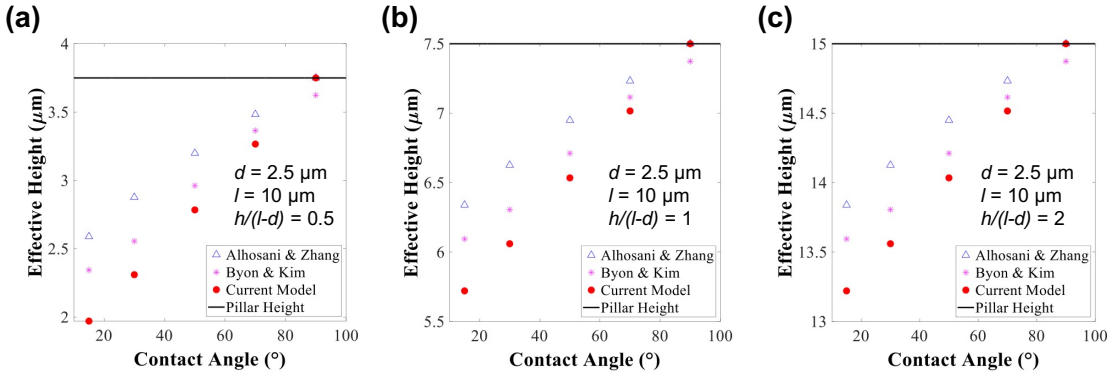

Figure 7. Comparison of the effective liquid heights from different models for d = 2.5 μm, l = 10 μm; $h/(l-d)$ = 0.5, 1 and 2.

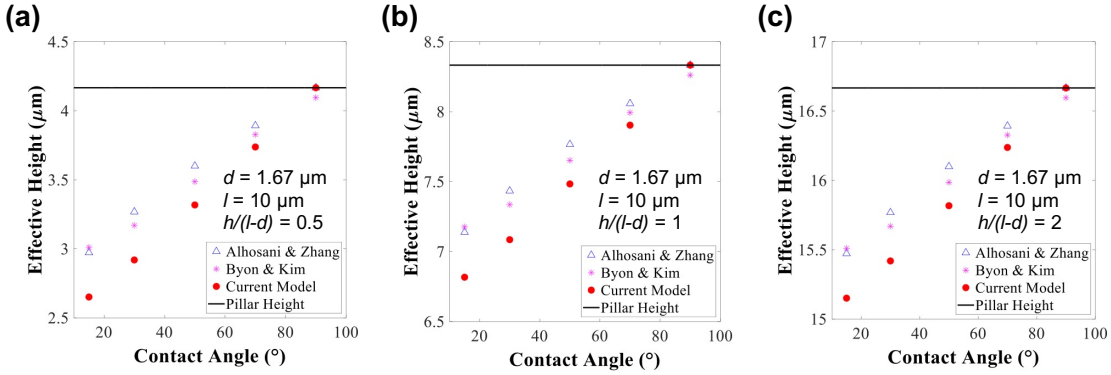

Figure 8. Comparison of the effective liquid heights from different models for d = 1.67 μm, l = 10 μm; $h/(l-d)$ = 0.5, 1 and 2.

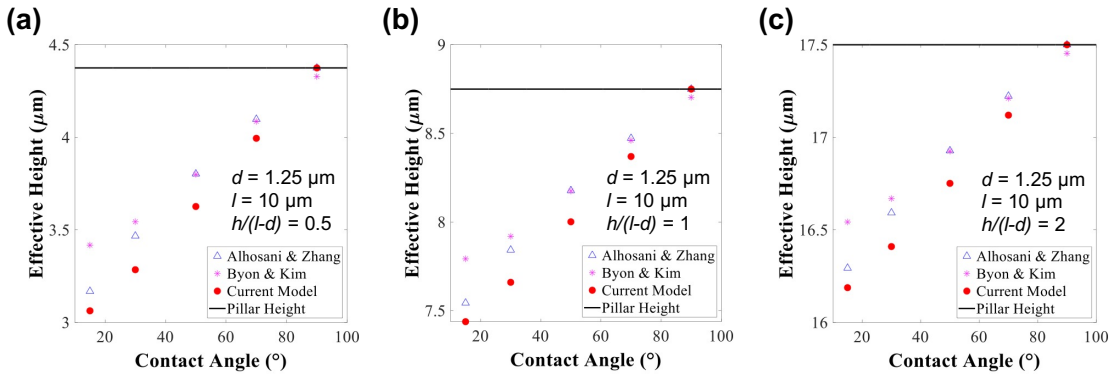

Figure 9. Comparison of the effective liquid heights from different models for d = 1.25 μm, l = 10 μm; $h/(l-d)$ = 0.5, 1 and 2.

We then update the model with the effective liquid heights for all discretized cells. The local effective height in each discretized cell is obtained from the local meniscus curvature, which is calculated based on the Young-Laplace equation (eq. 3.17) after a converged pressure profile is determined. Thus, for the i^{th} discretized element, integrating and averaging the x-direction velocity (u, eq. 3.20) in the height direction (y), the average cross-sectional velocity ($\bar{u}_i$) of the flow through the micropillar array can be updated to:

$$\overline{u_i} = -\frac{\kappa}{\mu \cdot \varepsilon}\left(\nabla P_i - \rho \cdot g\right)\cdot \Gamma$$
$$\Gamma = 1 - \frac{e^{2\sqrt{\frac{\varepsilon}{\kappa}}h_i} - 1}{\sqrt{\frac{\varepsilon}{\kappa}}h_i \cdot \left(e^{2\sqrt{\frac{\varepsilon}{\kappa}}h_i} + 1\right)} \tag{3.20}$$

where, h_i is the local effective height, and Γ is the bottom wall viscous effect factor from the solution of the Brinkman equation (eq. 3.1). Similarly, the mass balance (eq. 3.13) is updated with the local effective heights as shown in Figure 4c for both condensation and evaporation:

$$\begin{aligned} \bar{u}_{i-1} \cdot \varepsilon \cdot h_{i-1} \cdot l + v_{\text{cond}} \cdot \varepsilon \cdot l^2 \cdot AR &= \bar{u}_i \cdot \varepsilon \cdot h_i \cdot l \\ \bar{u}_{i-1} \cdot \varepsilon \cdot h_{i-1} \cdot l &= v_{\text{evap}} \cdot \varepsilon \cdot l^2 \cdot AR + \bar{u}_i \cdot \varepsilon \cdot h_i \cdot l \end{aligned} \tag{3.21}$$

where, AR is the area ratio of the curved meniscus area (*i.e.*, actual phase change interface area, Figure 4a) to its projected area ($\varepsilon \cdot l^2$) discussed earlier. The mass balance here assumes a generic porous media (we do not resolve the pillar or liquid/vapor volumes), and since $\bar{u}$ is the physical velocity, we correct for the actual flow area in the x-direction (flow direction) with the porosity.

3.1.4 Local Permeability Submodel

In porous media flow, permeability can be interpreted as the inverse of the viscous resistance to liquid propagation.[169, 170] To accurately estimate the permeability for flow through the micropillar array and account for the 3D shape of the meniscus, we estimate the two-dimensional (2D) viscous resistance from simulations and add a 3D correction based on the effective height of the micropillar array. We simulate the 2D velocity distribution within one unit cell (Figure 10a) for liquid passing through micropillar arrays for a large range of geometries ($d/l \leq 0.707$) using ANSYS Fluent,[171] and generate an equation for the 2D permeability based on simulation results:

$$\kappa_{2D} = \frac{l^2}{4\pi} \cdot \left[\log\left(\phi^{-0.5}\right) - 0.7105 + 0.6648\phi + 0.7086\phi^2 - 1.097\phi^3 \right] \tag{3.22}$$

where, l is the pitch and ϕ is the solid fraction (1-ε) of the pillar array given by:

$$\phi = \frac{\pi}{4} \cdot \left(\frac{d}{l} \right)^2 \tag{3.23}$$

This 2D permeability, κ_{2D}, is the permeability used in the Brinkman equation (eq. 3.1) and the resulting solutions (eqs. 3.4 and 3.12). In order to validate our 2D permeability, we compare the above result with available studies that have been used extensively in literature in the form of non-dimensional drag.[172, 173] Sangani and Acrivos[172] numerically studied creeping flow in 2D periodic pillar arrays and obtained the non-dimensional drag acting on the pillar. Yazdchi *et al.*[173] compared a few permeability models to finite element simulations, and created a hybrid equation based on the work from Gebart[174] and the model from Drummond and Tahir[175]. Figure 10b shows a comparison of the three models (the three lines overlap over much of the solid fraction range). Our proposed model (*i.e.*, the current model, red line) has a good agreement with the model of Yazdchi *et al.*[173] (green line). The discontinuity observed in the Sangani and Acrivos model[172] (blue line) arises from two formulae they reported which are applicable in two different solid fraction ranges. The black stars represent the geometries we simulated to generate the fitted equation for 2D permeability.

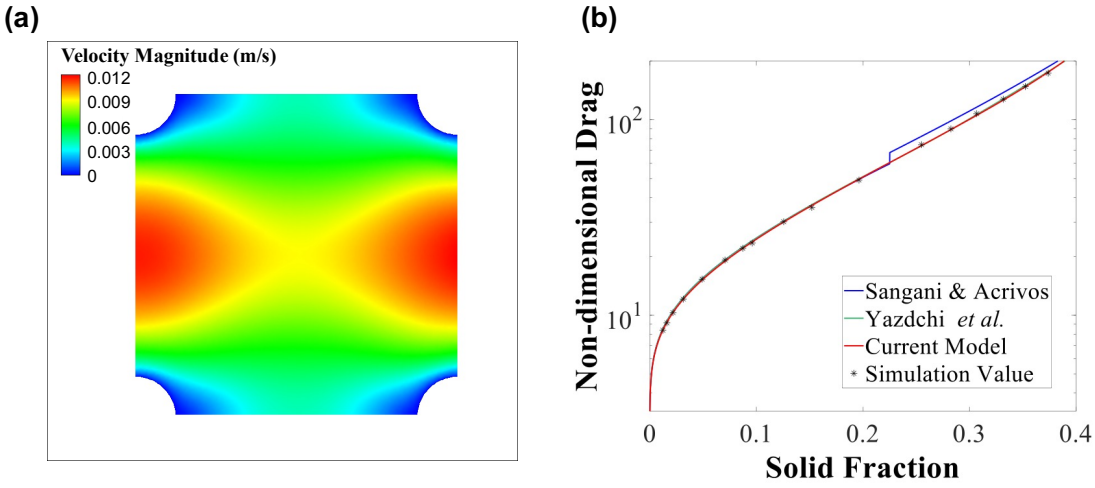

Figure 10. The top-view simulation contour plot in (a) shows the velocity distribution for a 2D unit cell with d = 2.5 μm, l = 10 μm. (b) Comparison of our 2D permeability prediction (red line) and the model developed by Sangani and Acrivos[172] (blue line) and Yazdchi *et al.*[173] (green line). Reprinted from Wang *et al.*, *Langmuir*, 2019.

The modeling of capillary driven flow through a thin porous material (micropillar arrays) can be alternatively solved using Darcy's law:[161, 176-179]

$$\frac{\mu \cdot \varepsilon}{\kappa} u = \rho \cdot g - \frac{dP}{dx} \tag{3.24}$$

The discretized solution to Darcy's Law after integrating and averaging the x-direction *physical* velocity in the height direction (y) is:

$$\overline{u}_i = -\frac{\kappa}{\mu \cdot \varepsilon}\left(\nabla P_i - \rho \cdot g\right) \tag{3.25}$$

Compared with the solution to the Brinkman equation (eq. 3.12), the only difference is the bottom wall viscous effect factor, Γ that results from the second order viscous term in the Brinkman equation (eq. 3.1). This is because the Brinkman equation accounts for the viscous resistance from the bottom wall (no-slip boundary condition) that the flow undergoes, while Darcy's law neglects the bottom wall viscous effect and assumes an

infinitely large porous media (or 3D pillars of infinite height).[156, 158, 180, 181] Therefore, when the Brinkman equation is used as the governing equation for modeling flow through micropillar arrays (*e.g.*, the current model), the 2D permeability κ_{2D} (eq. 3.22), must be used in the expression for the averaged velocity profile (eq. 3.12). This is because the Brinkman equation solution includes a viscous term that corrects for the flow resistance from the bottom wall (*i.e.*, Γ in eq. 3.20). However, if the governing equation is Darcy's law (eq. 3.24), the bottom resistance needs to be taken into consideration separately. This is done through a 3D permeability that is a product of the 2D permeability (eq. 3.22) and the bottom wall viscous effect factor, Γ (eq. 3.20):

$$\kappa_{3D,i} = \kappa_{2D} \cdot \left(1 - \frac{e^{2\sqrt{\frac{\varepsilon}{\kappa_{2D}}}h_i} - 1}{\sqrt{\frac{\varepsilon}{\kappa_{2D}}}h_i \cdot \left(e^{2\sqrt{\frac{\varepsilon}{\kappa_{2D}}}h_i} + 1 \right)} \right) \tag{3.26}$$

where, h_i is the local effective height and $\kappa_{3D,i}$ is the local permeability for the discretized element i from the local meniscus curvature K_i. Note, applying $\kappa_{3D,i}$ (eq. 3.26) in the Brinkman equation solution (eq. 3.1) will account for the bottom viscous effect two times leading to an under prediction of the average velocity in the flow direction.

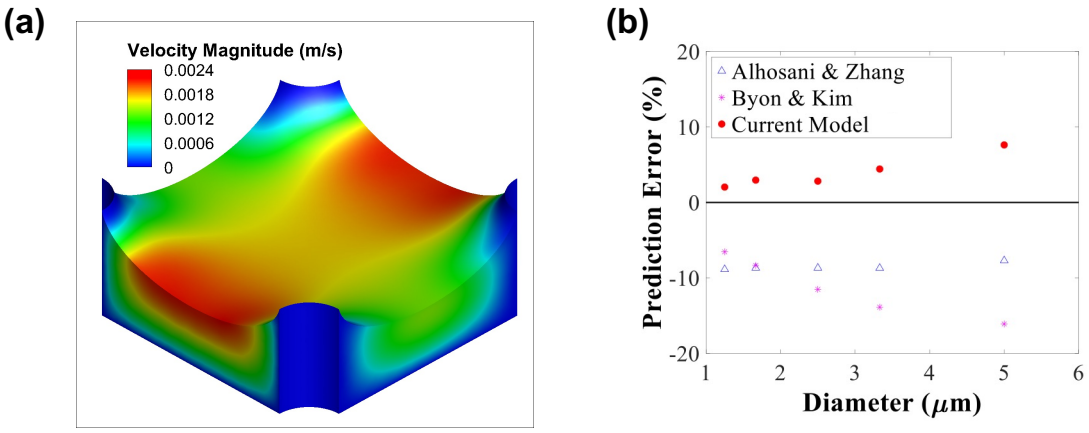

Figure 11. The numerical simulation contour plot in (a) shows the velocity distribution for a 3D unit cell with d = 2.5 µm, l = 10 µm, h = 3.75 µm, and θ = 15°. (b) The permeability prediction errors (θ = 15°) from different models for tall pillars at different diameters, l = 10 µm. Reprinted from Wang *et al.*, *Langmuir*, 2019.

To validate our methodology of correcting κ_{2D} with Γ to estimate a 3D permeability, we simulate (ANSYS Fluent) the 3D velocity fields (Figure 11a) in a unit cell for different contact angles (θ = 90°, 70°, 50°, 30°, 15°) which result in different meniscus shapes and 3D flow domains. In the CFD simulations, all the liquid-wall interactions were modeled with no-slip boundary conditions, the meniscus was modeled with a no-shear boundary condition, and a pressure gradient was applied across the inlet and outlet boundaries. Pressure drop is 10 Pa and the liquid temperature is 20 °C. Permeability predictions from our current model (eq. 3.26) and simulation values are also compared with available 3D permeability models reported by Byon and Kim[157] and Alhosani and Zhang[168]. We compare to these two models as both have considered the effects of the liquid-vapor interface and the effective liquid height within a unit cell on the permeability. We define the micropillar geometries based on a normalized height of $h/(l\text{-}d)$ = 0.5, 1 and 2, as short, medium and tall micropillars, respectively. The effect of

the liquid-vapor interface is smaller as this ratio increases, since meniscus variation (h-h_{min}) is determined by d, l and θ, and is relatively small compared to the height of taller pillars. The complete comparisons for all pillar diameters, heights and contact angles are shown in Figures 5-9. Our current model (eq. 3.26) predicts 3D permeability with an average relative error of 5.18% with respect to the 3D numerical simulation, and the corresponding average errors for Byon and Kim[157] and Alhosani and Zhang[168] have magnitudes of 8.43% and 9.11% respectively. Additionally, a large under prediction at a small contact angle (15°) is observed for both Byon and Kim (average relative error ≈-11.28% at different diameters) and Alhosani & Zhang (average relative error ≈-8.53%) as shown in Figure 11b, while the average relative error for our current model ($\theta \approx 15°$) is ≈3.98%. An analysis of the models reported by Byon and Kim[157], and Alhosani and Zhang[168] show that both use a κ_{3D} formulation similar to eq. 3.26, however, their permeability models use additional factors to correct for the variation of wetted area (Λ_1) and the channel cross section area (Λ_2):

$$\Lambda_1 = \frac{h_{eff} + \frac{\varepsilon \cdot d}{4(1-\varepsilon)}}{h + \frac{\varepsilon \cdot d}{4(1-\varepsilon)}} \;,\; \Lambda_2 = \frac{h_{eff}}{h} \tag{3.27}$$

where, h_{eff} is the effective liquid height that the two models define independently, and ε is the porosity of the micropillar arrays. Both these factors (Λ_1 and Λ_2) serve as a correction for the actual liquid volume in the unit cell (*i.e.*, they correct for the effective height). Due to the fact that the effective height has already been considered as part of the viscous resistance term in the solution of the Brinkman equation (factor Γ) which both models

solve, this over-correction leads to an under prediction of the permeability (Figure 11b), especially at smaller contact angles (*i.e.*, when Λ_1 and Λ_2 are small). In addition to the factors Λ_1 and Λ_2, another reason for the deviation between the semi-analytical predictions of the permeability where the meniscus shape is considered (past work[152, 157, 168] and our current model) and the numerical simulations is the methodologies/assumptions adopted to predict the effective height. Despite the fact that we reduce a 3D shape of the meniscus into an effective height, our predictions of the 3D permeability have the smallest error as compared to the numerical simulation predictions. We suggest that the reason for this favorable comparison is that we predict the actual shape of the meniscus as opposed to other methods used in literature.

Besides the models reported by Byon and Kim[157] and Alhosani and Zhang[168], we also included two models (Tamayol and Bahrami[166] and Srivastava *et al.*[165]) for cylindrical micropillar arrays with the assumption of a flat meniscus across the array in our complete 3D permeability comparison (Figures 12-16) for various micropillar diameter, heights and contact angles. The results predicted by Tamayol and Bahrami[166] and Srivastava *et al.*[165] do not vary with contact angle, since the meniscus curvature is not considered in either model; this results in a horizontal straight line in the figures. The model developed by Tamayol and Bahrami[166] over predicts the permeability at all d/l ratios and all $h/(l\text{-}d)$ ratios, while the model reported by Srivastava *et al.*[165] has close predictions compared to simulation values for tall pillars ($h/(l\text{-}d) = 2$), but it has larger error for short pillars ($h/(l\text{-}d) = 0.5$).

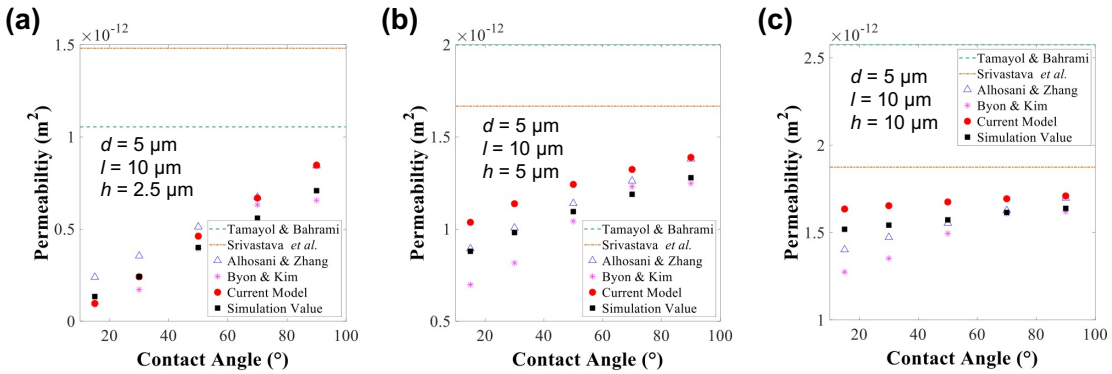

Figure 12. Comparison of permeability models for d = 5 μm, l = 10 μm; $h/(l-d)$ = 0.5, 1 and 2.

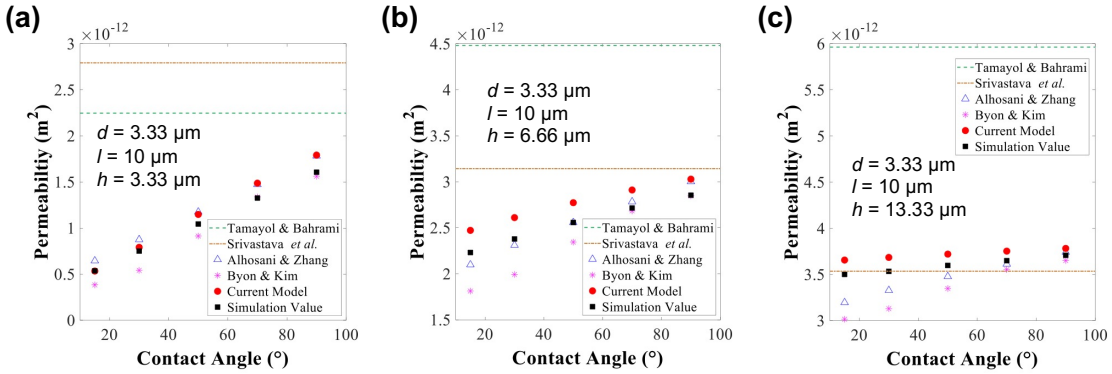

Figure 13. Comparison of permeability models for d = 3.33 μm, l = 10 μm; $h/(l-d)$ = 0.5, 1 and 2;

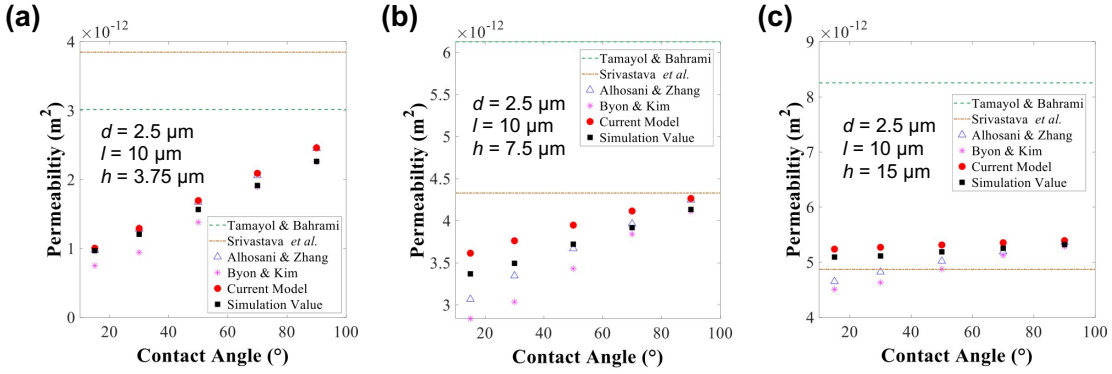

Figure 14. Comparison of permeability models for d = 2.5 μm, l = 10 μm; $h/(l-d)$ = 0.5, 1 and 2;

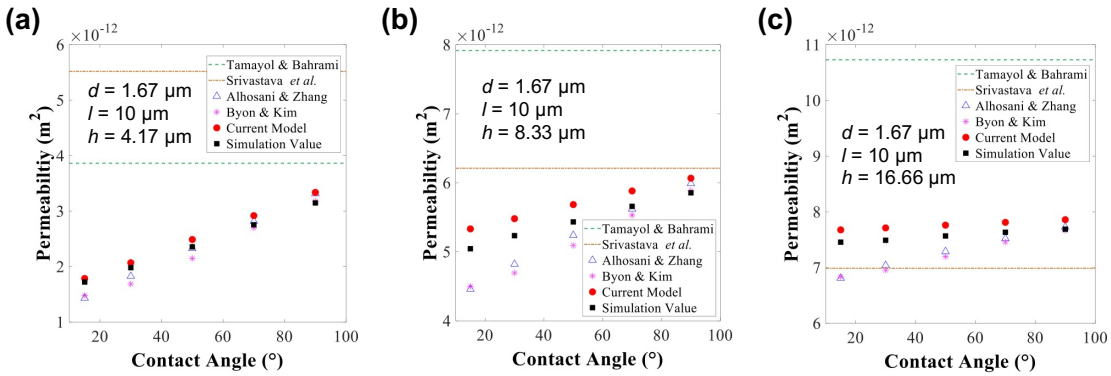

Figure 15. Comparison of permeability models for d = 1.67 μm, l = 10 μm; $h/(l-d)$ = 0.5, 1 and 2.

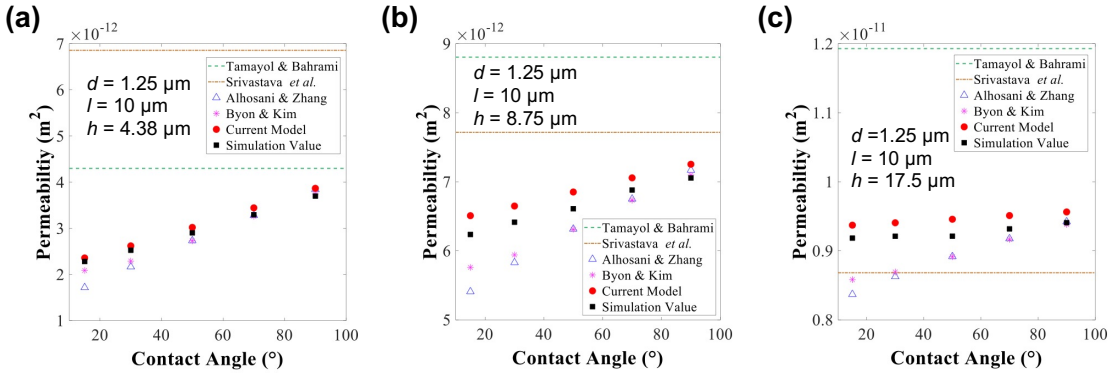

Figure 16. Comparison of permeability models for d = 1.25 μm, l = 10 μm; $h/(l-d)$ = 0.5, 1 and 2.

Additionally, we compare predictions from the current model with numerical CFD simulation values for a wide range of geometries and varying contact angles. Figure 17a shows the comparison of permeability for different height ratios (0.5, 1 and 2) and contact angles (90°, 50° and 15°) at micropillar diameters ranging from 1.25 μm to 5 μm with a pitch of 10 μm (*i.e.*, d/l ratio from 1/8 to 1/2). The comparisons illustrate the accuracy of current model and its extensive validity. In Figure 17b, the ±5% variation region (blue shaded area) and the ±10% variation region (yellow shaded area) in the Q-Q plot indicate that most of the permeability prediction errors are within ±5%.

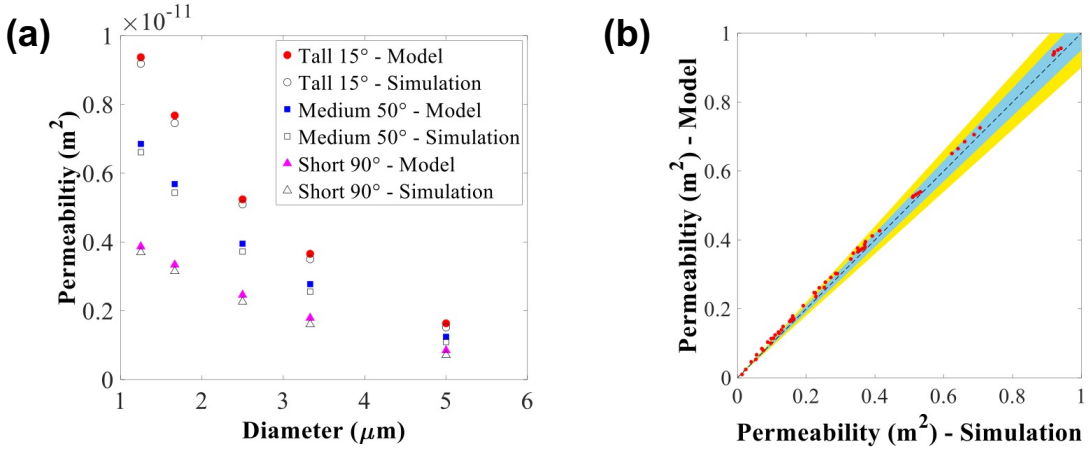

Figure 17. (a) Comparison of the current 3D permeability model and simulation values at different pillar diameters, heights and contact angles. (b) Quantile-quantile (Q-Q) plot for simulation and model prediction, the black dashed line (45° line) indicates full agreement (0% relative error), the blue and yellow shaded regions represent ±5% and ±10% variation/error, respectively. Reprinted from Wang *et al.*, *Langmuir*, 2019.

3.2 Model Application to Evaporation

3.2.1 Model Validation

As previously stated in Sections 3.1.1 and 3.1.2, this modeling framework for fluid flow through porous media can be used to calculate both evaporation and condensation heat transfer performance. The primary differences are the direction of the vapor flow and the pressure profile resulting from the pressure boundary conditions. In this section, we apply this model (*i.e.*, discretized and incorporated the local meniscus curvature/shape) to thin-film evaporation from micropillar arrays to predict the maximum heat flux at the dry-out condition in steady state. The 3D schematic of the evaporation process is shown in Figure 18a.

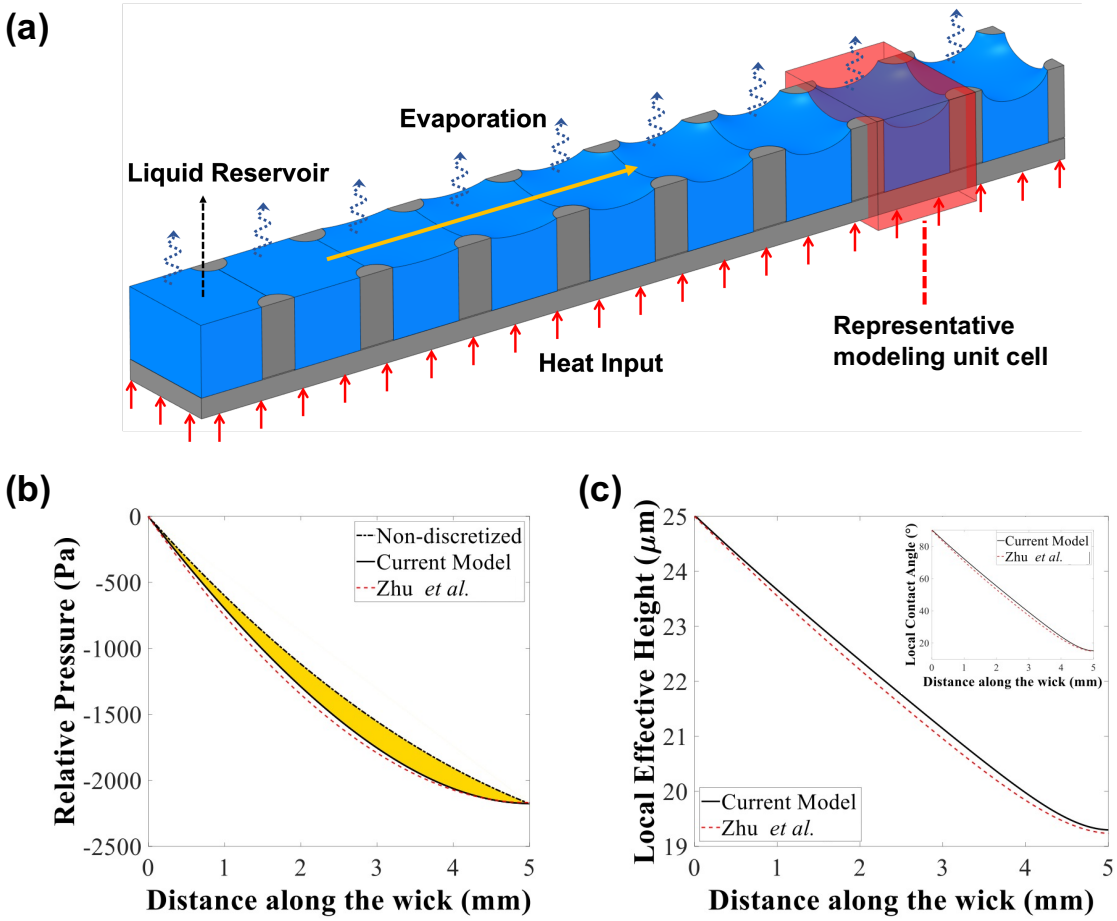

Figure 18. (a) 3D schematic for thin-film evaporation from micropillar arrays. Comparisons of (b) pressure profiles and (c) local effective height and local contact angle from different models/methods. The micropillar array geometry is d = 10 μm, l = 30 μm, and h = 25 μm. Reprinted from Wang *et al.*, *Langmuir*, 2019.

Figure 18b compares the pressure profiles predicted by a non-discretized model (black dash-dot line), discretized model (current model, black solid line) and the numerical model developed by Zhu *et al.*[151] (red dashed line). The reference model[151] is selected and assumed to have accurate predictions due to the extensive CFD simulations performed in terms of the geometric parameters (*i.e.*, diameter, pitch and height) and the liquid-solid contact angles. The near-linear pressure profile predicted by the non-discretized model is an over prediction, since the velocity prediction is a result of a linear pressure gradient

assumption. The pressure profile from the current model shows a minor variation from the reference model[151], and this discrepancy may be attributed to the error in prediction of the permeability which affects the pressure drop. Figure 18c compares the local effective height and the local contact angle along the micropillar array, the average variations for both parameters are less than 1%. The small variations in the predictions for h_{eff} and θ with the results from Zhu *et al.*[151] likely result only from the difference in pressure predictions: we use a common model to predict the meniscus shape[163], however, the local meniscus shape is calculated from the local pressure.

In addition to validating the pressure profile, local effective height, and local contact angle, we verify our evaporation model by comparing the dry-out heat flux with the experimental results from Zhu *et al.*[151] for three different micropillar array geometries at different dry-out length. The maximum dry-out heat flux q'' for evaporation is calculated from the converged solution of v_{evap} obtained from the mass balance (eq. 3.21), using a mass-energy balance for the entire micropillar array (*i.e.*, the total heat flux input from the heater balances the heat flux induced by the phase change):

$$q'' = \rho_l \cdot v_{\text{evap}} \cdot h_{\text{fg}} \tag{3.28}$$

where, ρ_{l} is the liquid density and h_{fg} is the latent heat capacity of the working fluid. Figure 19 shows average variations of 7.77%, 17.41% and -0.20% for samples A1, A2 and A3 respectively with most predictions lying within the experimental uncertainty bounds. We used the experimental results of Zhu *et al.* for model validation due to the experimental setup having a similar geometry to the current model.

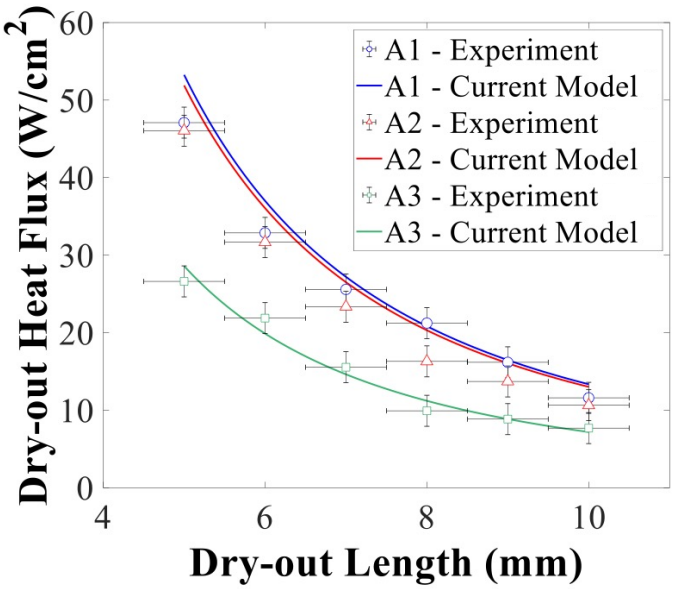

Figure 19. Model validation against experimental results from Zhu *et al.* The geometries are $d = 7$ µm, $l = 20$ µm, and $h = 20$ µm for sample A1, $d = 7$ µm, $l = 30$ µm, and $h = 19$ µm for sample A2, and $d = 6$ µm, $l = 50$ µm, and $h = 19$ µm for sample A3. Reprinted from Wang *et al.*, *Langmuir*, 2019.

3.2.2 Model Accuracy Discussion

To emphasize the importance of discretization and using local properties, we compare the current model (discretized model with spatially varying properties) with a non-discretized model and a discretized model with constant properties (*i.e.*, uniform effective height) at different d/l ratios and $h/(l-d)$ ratios. The uniform effective height applied to the constant property discretized model is the average of the height of the first and last unit cell. Using a uniform height ensures that the permeability is also uniform over the length of the micropillar array. The solid lines and the dash-dot lines in Figure 20a represent the heat flux predictions from the current model with spatially varying properties and the discretized model with constant properties respectively, at a

fixed d/l ratio. The variation between these two models are 3% for relatively shorter micropillars ($h/(l-d) = 1$) and 0.3% for relatively taller micropillars ($h/(l-d) = 4$), therefore the solid lines and the dash-dot lines are almost overlapped in the figure. This is expected, since the effect of the liquid-vapor interface, specifically the effective height resulting from the meniscus curvature, is negligible for taller micropillars (*i.e.*, the effective liquid height is closer to the height of micropillars). When the $h/(l-d)$ ratio approaches 0.5, the deviation between the two models increases to 13.3%, which we did not plot in the figure due to the different magnitude of the heat flux. Hence, for short micropillar arrays, it is necessary to apply locally varying properties (as presented in current model) to precisely predict the dry-out heat flux. For tall pillars, constant/average properties may be used, however, an accurate prediction of the meniscus shape is still required as it will result in the most accurate estimation of the effective height and permeability (κ_{3D}).

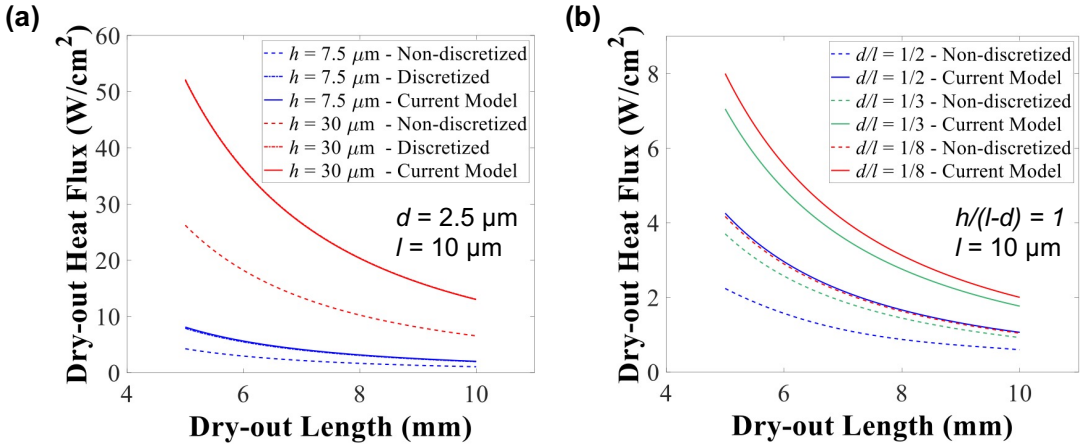

Figure 20. Comparison of dry-out heat flux predictions from the non-discretized model, the discretized model with constant properties (*i.e.*, constant effective height) and the current model (discretized model with spatially varying properties) (a) at different normalized heights with a fixed d/l ratio of 1/4, and (b) at a constant height ratio of $h/(l-d) = 1$ and varying d/l ratios. Reprinted from Wang *et al.*, *Langmuir*, 2019.

Since the variation is small for tall micropillars between the current model and the discretized model with constant properties, while the variation is large for the current model and the non-discretized model, we compare the current model and the non-discretized model at a constant height ratio and varying d/l ratios (1/2, 1/3 and 1/8) in Figure 20b. The predictions from the non-discretized model are inaccurate as compared to the current model results for all d/l ratios. This is because the non-discretized model has a near-linear pressure profile (dash-dot line in Figure 20a) generated from an assumption of a constant pressure gradient over the length of the micropillar wick. These comparisons indicate that discretization of the flow domain is required to predict an accurate pressure profile and an accurate dry-out heat flux for thin-film evaporation from micropillar arrays.

3.3 Model Application to Condensation

3.3.1 Concept of Capillary-Enhanced Filmwise Condensation

In this section, we first propose a robust and scalable capillary-enhanced filmwise condensation mode that enhances phase change heat transfer by increasing the effective thermal conductivity of the condenser and the condensate. A multi-layer sintered metal woven wire mesh is used to demonstrate the concept in Figure 21, and the constant properties are assumed to simplify the problem. Since no explicit unit cell can be used as the discretized cell as in micropillar arrays (liquid region within four pillars), we discretized the wick structure into 101 elements, which is sufficiently large number that the pressure drop can be assumed to be linear in each discretized element.

The concept of capillary-enhanced filmwise condensation leverages the capillary pressure within the pores of a wick to drive condensate removal from the surface. The enhancement is achieved *via* the use of a high thermal conductivity wick material that enables a higher heat transfer coefficient (HTC) than traditional filmwise condensation. In this mode of condensation, the top surface of the condenser is a micro/nanoporous wick material and as condensation occurs, this porous layer fills up with the condensate (Figure 21). Due to interactions between the liquid condensate and solid wick material in the micro/nanoscale pores, a curved liquid-vapor interface (or meniscus) is formed with the liquid pressure being lower than the vapor pressure for a wetting liquid. To enable steady state operation, the condensate has to be removed from the wick at the rate at which condensation is occurring. While the capillary pressure facilitates condensate flow through the wick and maintains a thin (≈ wick thickness) stable liquid film within the wick due to surface tension forces, condensate removal relies on an external force. As shown recently by Preston *et al.*,[45] this external force may be gravity. An alternate mechanism for condensate removal that we propose here is by the use of a pump.

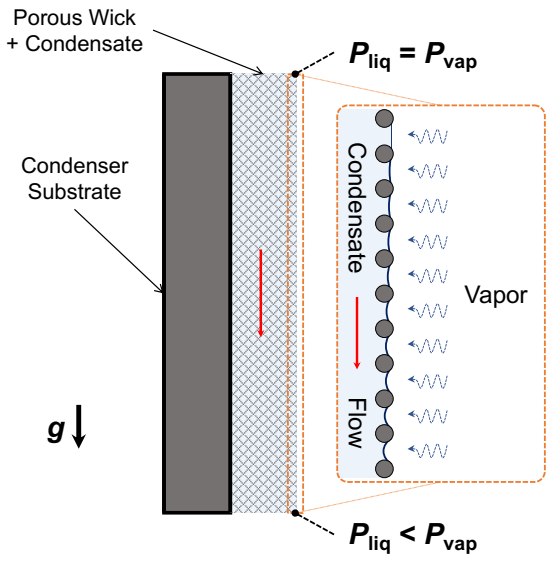

Figure 21. Concept of capillary-enhanced filmwise condensation representatively showed with woven mesh. Reprinted from Wang and Antao, *Langmuir*, 2018.

The failure mechanism for the enhancement achieved *via* this mode of condensation is when the wick *floods* and a low thermal conductivity liquid film covers the wick layer. This has the same detrimental effect as the liquid film in filmwise condensation, though with the added thermal resistance of the wick. Flooding will occur when the rate of condensation is higher than the maximum rate of condensate removal that can be sustained by the driving pressure force. In the case of the pump proposed in this study, we set the limit to be the maximum capillary pressure at the location where the condensate is removed from the wick. This maximum capillary pressure is the pressure difference that is generated across a liquid-vapor interface when the meniscus curvature is maximum and the contact angle between the liquid and solid is the receding contact angle.[15, 155, 163] In general, condensation is driven by the surface subcooling (*i.e.*, the temperature difference between the surface and the vapor) for any heat transfer coefficient.

We define the maximum subcooling as the maximum temperature difference beyond which the wick floods. The wick cannot support a condensate flowrate higher than that generated at the maximum subcooling since the maximum pressure drop has been achieved. Hence, the failure limit is the maximum subcooling which is balanced by the maximum capillary pressure that supports the resulting condensate flow (and rate of condensation). We note that this failure criterion is specific to the capillary-enhanced mode of condensation on a wick surface as the pump itself may be capable to supporting higher condensate flow (and higher subcooling or condensation rate). However, in the case where condensate removal is only dependent on the pump, condensation performance will be limited by the pump characteristics. This is a possible operating condition when the wick floods and a thin condensate layer/film forms above the wick. In this case steady state operation exists if the rate of condensation is balanced by the rate of condensate removal by the pump, which depends on the characteristic pump curve and the operating conditions. While we define the incipience of flooding as a failure criterion for the capillary-enhanced mode, condensation HTC is still expected to be higher than traditional filmwise condensation at the initiation of flooding (as observed by Renken and Mueller[44]). The HTC will be higher than filmwise condensation until the combined thermal resistance of the wick and the flooded layer/film above the wick equals that of the liquid film in filmwise condensation for the same condenser subcooling.

The benefit of this mode of condensation is that the condenser does not require low surface energy non-wetting coatings which have been shown to degrade over time. The wetting requirement of the wick material enables the enhancement of condensation in

applications where the condenser material has high surface energy: industrial condensers and heat pipes that use metals and vapor chambers for thermal management of electronics that use silicon, both of which are expected to be robust and highly wetting. It also enables the enhancement of condensation heat transfer in liquefaction of natural gas (and other hydrocarbons) where the low surface tension of the fluid prevents condensation in the dropwise mode with most low surface energy coatings (*i.e.*, hydrophobic coatings). While coatings are not necessary, they may be leveraged to enhance the condensation performance by delaying flooding when water is the condensing fluid, as shown by Oh *et al.*[145] Finally, this condensation enhancement technique can be applied in either gravity or zero/micro-gravity environments where condensate removal may be facilitated by the pump (*e.g.*, thermal management of electronics in space and in aircrafts).

3.3.2 Heat Transfer Coefficient (HTC) Enhancement

In order to estimate the heat transfer performance, a similar mass-energy balance as in evaporation is used to calculate the maximum condensation heat flux q'' from the converged solution of the condensation volumetric flow rate, v_{cond}:

$$q'' = \rho_l \cdot v_{cond} \cdot h_{fg} \tag{3.29}$$

where, ρ_l is the condensate density and h_{fg} is the latent heat capacity of the condensing fluid. The HTC for condensation h_c is obtained from a 1D thermal resistance network through the wick[45] and the subcooling ΔT_{max} is calculated from q'' and h_c:

$$h_c = \frac{k_{eff}}{t}$$
$$\Delta T_{max} = T_{wall} - T_{vap} = \frac{q''}{h_c} \tag{3.30}$$

where, T_{wall} and T_{vap} are the wall and vapor temperatures respectively, and k_{eff} is the effective thermal conductivity of the wick condensate layer given by:[182, 183]

$$k_{eff} = \frac{\left(2 \cdot k_{wick} + k_l - 2\left(k_{wick} + k_l\right)\left(1-\varepsilon\right)\right) \cdot k_{wick}}{2 \cdot k_{wick} + k_l + 2\left(k_{wick} + k_l\right)\left(1-\varepsilon\right)} \tag{3.31}$$

where, k_{wick} is the thermal conductivity of the solid mesh (≈100 W/m·K, a representative value for metals and silicon), k_l is the thermal conductivity of the working fluid (*i.e.*, pentane or water), and ε is the wick porosity. The results for the HTC are compared to the corresponding HTC for filmwise condensation as predicted by the Nusselt model for a thin falling film:[31, 184]

$$h_{Nusselt,\,x} = \left[\frac{\rho_l \cdot h_{fg} \cdot \left(\rho_l - \rho_v\right) \cdot g \cdot k_l^{\,3}}{4\mu \cdot \Delta T_{max} \cdot x}\right]^{\frac{1}{4}}$$
$$\text{HTC Enhancement} = \frac{h_c}{h_{Nusselt}} \tag{3.32}$$

where, ρ_l and ρ_v are the condensate and vapor densities, k_l is the condensate thermal conductivity. This expression for filmwise condensation (eq. 3.32) is a *local* HTC which depends on the specific location along the condenser surface (x direction) and provides an accurate local comparison of the HTC Enhancement expression. For the average enhancement over filmwise condensation, the local HTC is integrated over the length of the wick. The HTC Enhancement is a metric to characterize the increased HTC achieved *via* the capillary-enhanced mode of condensation over traditional filmwise condensation.

In the model, we assumed a multi-layer sintered metal woven wire mesh wick of length $L \approx 2.54$ cm with porosity 0.65 and hence an effective thermal conductivity of ≈55 W/m·K (obtained from eq. 3.31). The permeability range used here is typical for packed wire mesh screens (10^{-13} - 10^{-08} m^2).[185, 186] The working fluids modeled are pentane ($\theta_{rec} \approx 1°$) and water ($\theta_{rec} \approx 20°$) with temperature dependent saturation properties obtained from NIST REFPROP,[187] and the temperature of the wall/wick was assumed to be 30 °C. These two liquids are chosen due to their distinct thermophysical properties related to capillary driven flows (viscosity and surface tension) and phase change heat transfer (latent heat capacity). Water (relatively high surface tension) and pentane (relatively low surface tension) are also chosen to demonstrate the versatility of the concept (and the modeling framework) in enhancing condensation heat transfer for a variety of applications. Here we discuss some key results that emphasize the salient features of the model, including the importance of discretization in predicting an accurate pressure gradient and condensation rate, and the effects of gravity on the wick design/performance. We also highlight how the condensing fluid affects performance during this mode of condensation heat transfer, and the relationship between heat transfer performance (*i.e.*, HTC, h_c and surface subcooling, ΔT_{max}) and wick geometry (*i.e.*, thickness, t and permeability, κ).

For flow through a constant porosity and permeability porous medium, the pressure gradient along the porous zone is typically assumed (and expected) to be linear, and the velocity profile and the average velocity do not vary along the length of the porous medium. However, for capillary driven flow where mass addition (*e.g.*, condensation) or

mass loss (*e.g.*, evaporation) occur along the length of the porous medium, the linear assumption is not accurate for constant porosity and permeability. Consider the case when mass is being added *via* condensation to the porous medium or wick uniformly over its length, the fluid velocity increases linearly along the flow direction. When we discretize the wick (Figure 2 in Section 3.1.2), each discrete element has a higher fluid velocity than the preceding element due to mass addition. From the Brinkman equation (eq. 3.1), a higher fluid velocity requires a higher pressure drop across the element to sustain it. Hence, at the beginning of the wick, the pressure drop per element is small corresponding to the low fluid velocity, and the pressure drop for each element increases along the wick length due to the increasing local fluid velocity for each element. Since the pressure budget (or the maximum allowable pressure drop) is fixed by the maximum capillary pressure at the end of the wick, a linear pressure profile assumption will underpredict the maximum allowable fluid flowrate through the wick. This is because the linear pressure profile assumption utilizes more pressure drop at the beginning of the wick where the low fluid flowrate does not require the same pressure drop as the end of the wick with a high liquid flowrate. When the mass addition is in the form of condensation, this leads to an underprediction of the condensation rate. The opposite is true for evaporation (*i.e.*, mass loss) from porous media sustained by capillary driven flow where a linear pressure profile over-predicts the liquid flowrate or evaporation rate. This is because in the evaporation case, a higher flowrate exists at the beginning of the wick and a near-zero flowrate exists at the end of the wick (*i.e.*, the opposite of the mass addition or condensation case). The only exception to the requirement for a non-linear pressure profile in the above cases is

when the porous medium is infinitesimal in length and the linear approximation holds (*e.g.*, a small discretized element).

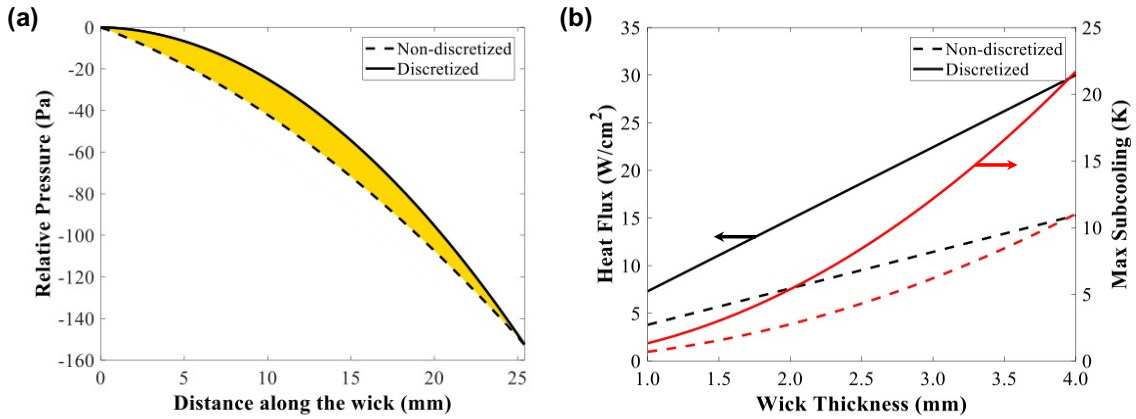

Figure 22. Comparisons of the non-discretized and the discretized model on (a) relative pressure profile along the wick length, and (b) condensation heat flux and maximum subcooling as a function of the wick thickness. The permeability of the wick is 1×10^{-10} m^2, the fluid is pentane, and the wick thickness in (a) is 2.0 mm. Reprinted from Wang and Antao, *Langmuir*, 2018.

Figure 22a compares the pressure profiles as predicted by the non-discretized and discretized models. Due to the low total flowrate of condensate near the start of the wick (*e.g.*, $\bar{u}_0 = 0$ for $i = 1$), we expect a low pressure drop and a near zero-gradient in the pressure profile (or low slope) at this location as explained earlier in Section 3.1.2 (eq. 3.7). As the flowrate through the wick increases along its length (mass addition *via* condensation), the local pressure gradient increases to accommodate this higher flowrate. This feature of a non-uniform pressure gradient is accurately predicted by the model with discretized elements after iteration convergence is reached. The non-discretized single-zone/element model does predict a non-linear pressure profile (as expected based on eq. 3.9), however, the profile does not appear physically accurate based on the discussion above. The near-linear pressure profile predicted by the non-discretized model is thus a

conservative estimate of the available pumping pressure force as compared to the physically accurate discretized model. This difference in the pumping pressure force as predicted by the two models directly affects the condensation heat flux and the maximum subcooling as can be seen in Figure 22b. For any given wick thickness, the predicted condensation flux v_{cond} is higher for the discretized model. Hence, we observe a higher prediction of the condensation heat flux from the discretized model. Similarly, the maximum subcooling also increases with the larger available pumping pressure force (discretized v/s non-discretized models), for a fixed wick thickness (eq. 3.30). As stated earlier, the maximum subcooling is the maximum temperature difference beyond which the wick floods. Above this, the pressure drop required to sustain higher condensate flowrate is higher than the maximum capillary pressure achievable. When the thickness of the wick increases (other geometric parameters constant), the condensation flux increases (Figure 22b) due to the increase in the capacity of the wick (eq. 3.29 and 3.30). To sustain this higher rate of condensation at larger thickness, the maximum subcooling also increases (Figure 22b). However, while the condensation flux is directly proportional to the thickness for the cases studied here, the maximum subcooling increases $\approx t^2$, since the heat transfer coefficient for condensation in this mode is inversely proportional to the wick thickness (eq. 3.29). A comparison of the discretized and non-discretized models in Figure 22b shows that there is a deviation in the predictions from the two models for both q'' and ΔT_{max} as the thickness increases. This can be attributed to the increased capacity as the wick thickness increases for a fixed wick permeability combined with the expected linear variation in the condensation mass flux v_{cond}.

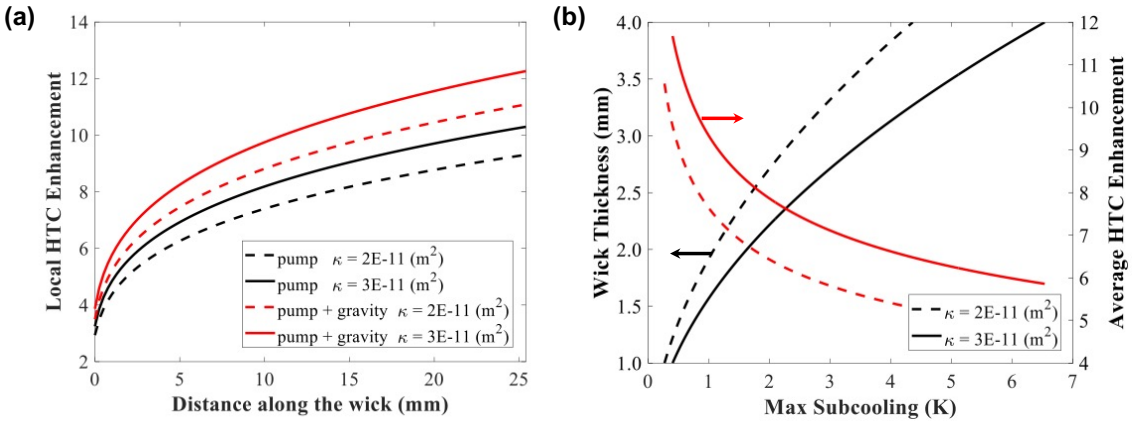

Figure 23. (a) Local HTC enhancement along the wick. (b) Average HTC enhancement at various wick thickness and subcooling. Reprinted from Wang and Antao, *Langmuir*, 2018.

The requirement for steady operation in this capillary-enhanced mode of condensation is the continuous removal of the condensate from the wick. As stated in the concept description, the capillary pressure provides the necessary pressure gradient to drive the flow through the wick, however, continuous operation requires the condensate to be removed where $P = P_{cap}$. This may be achieved by pump-driven, or pump- and gravity-driven (or pump-driven and gravity opposed and *vice versa*) flow. When designing for the mechanism of condensate removal, it is important to understand the relative potential offered by each (pump and gravity). We apply the model to predict the heat transfer performance of the wick during condensation and compare the cases of pump-driven and pump- and gravity-driven (pump and gravity acting in the same direction). We do not consider the situation of gravity-driven, as a model for that particular case has been developed and presented by Preston *et al.*[45] Additionally, we expect a linear gradient in the driving force for the gravity-driven case and hence discretization of the wick domain may not offer additional accuracy. The discretization,

however, allows us to predict the *local* HTC Enhancement along the wick. For a falling film during filmwise condensation, the film thickness varies as a function of length in the direction of gravity, hence locally, the filmwise HTC may be high due to the small film thickness. This leads to a variation in the HTC Enhancement along the wick length as seen in Figure 23a since h_c is constant for a fixed set of wick geometric properties. As the permeability increases, the condensation heat flux increases since $v_{cond} \propto \kappa$, which leads to an increase in ΔT_{max} and a reduction in $h_{Nusselt}$, hence the HTC Ratio increases with an increase in permeability. The effect of gravity is to increase the potential driving the flow (eq. 3.32), however, it does not affect the pressure profile. Leveraging gravity in addition to the pump for condensate removal doubles v_{cond}, and proportional enhancements are observed for both the condensation heat flux and the maximum subcooling since the pressure gradient and $\rho \cdot g$ are comparable for pentane as the working fluid. In Figure 23b we see the interplay between the permeability, thickness, maximum subcooling and the average HTC Enhancement. As the thickness of the wick is increased, the maximum subcooling threshold increases ($\Delta T_{max} \propto t^2$). The increase in the subcooling ΔT_{max} leads to a decrease in $h_{Nusselt}$ ($\propto (1/\Delta T_{max})^{1/4}$), however, the linear inverse dependence of h_c on t leads to an overall decrease in the HTC Enhancement with increases in both t and ΔT_{max}. Since a higher permeability can support higher ΔT_{max} for the same wick thickness, the HTC Enhancement increases with the permeability for any wick thickness and ΔT_{max} (Figure 23b).

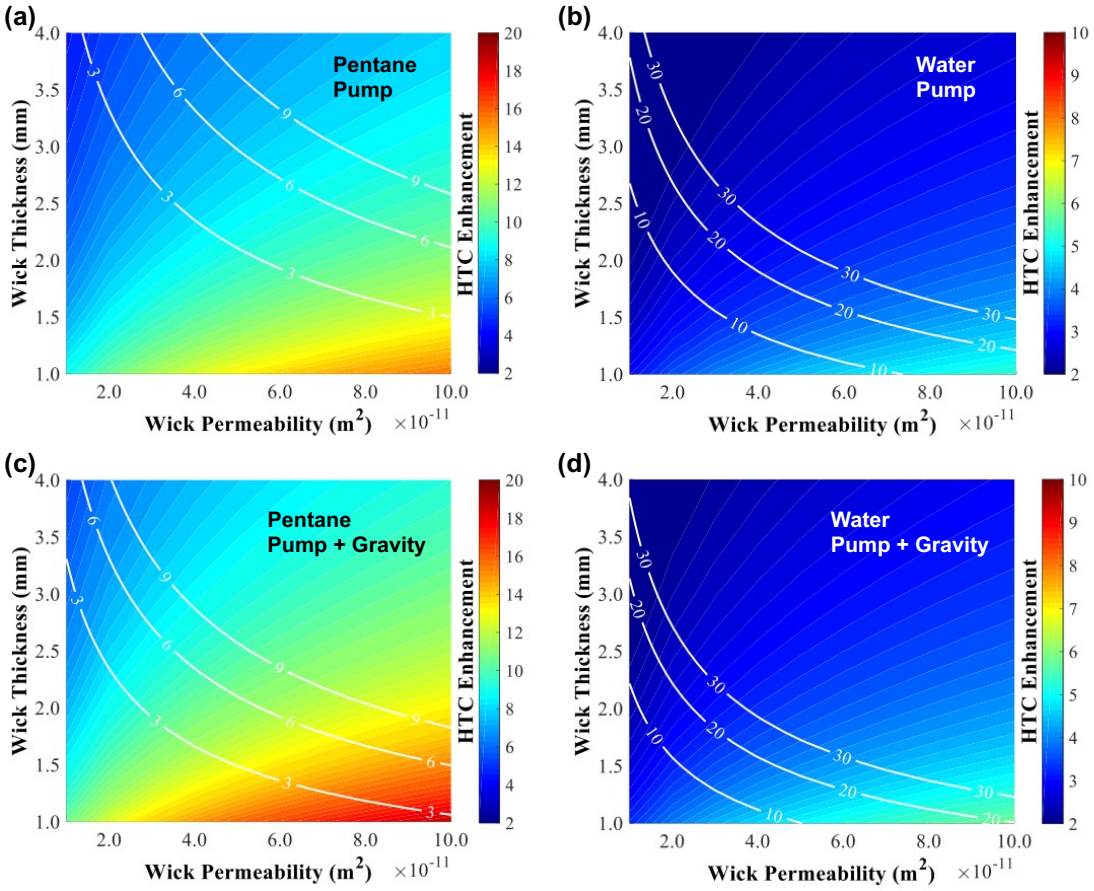

Figure 24. Regime maps for condensation heat transfer performance enhancement with the capillary enhanced filmwise condensation mode over traditional filmwise condensation: (a) pentane and (b) water in the absence of gravity, and (c) pentane and (d) water when gravity and the pump act in the same direction. Reprinted from Wang and Antao, *Langmuir*, 2018.

We created a regime map (Figure 24) to summarize predicted heat transfer performance during capillary-enhanced filmwise condensation in microporous wicks for different wick geometries. The color contour plots show the expected enhancement in the HTC over the traditional filmwise mode and the line contours for the maximum subcooling define the limits beyond which flooding occurs and condensation *via* this mode fails. Figures 24a and 24b compare the relative heat transfer performances for pentane

and water, respectively. Compared to traditional filmwise condensation, higher enhancements can be achieved with pentane (*versus* water) in the capillary-enhanced condensation mode. However it is important to note that the h_{Nusselt} for pentane is lower than water which has comparatively higher density, thermal conductivity and latent heat capacity. With a high thermal conductivity, the h_c for water is expected to be higher than the corresponding value for pentane despite having a lower relative enhancement over h_{Nusselt}. The favorable thermophysical properties of water, specifically the latent heat capacity and surface tension also support a higher limit for the maximum subcooling ($\approx$ 8-10×) as compared to pentane. We can hence expect similar performance comparisons for other dielectric and non-polar liquids with low latent heat capacity and surface tension as compared to water. Additionally, increasing the permeability increases the threshold for flooding at a constant wick thickness and a similar effect is achieved by increasing the thickness for a wick of constant permeability (*e.g.*, Figure 24a). However, the benefit of increasing permeability over increasing the thickness is that a higher HTC Enhancement can be achieved over traditional filmwise condensation. The reason for this trend is that while v_{cond} (and hence q'' and ΔT_{max}) can be increased by increasing either t or κ, increasing t also decreases h_c, hence it is more favorable to increase the permeability over the thickness of the wick.

As seen in Figure 24a, when the pump is supplemented by gravity-driven flow, there is an increase in the condensation heat transfer rate (v_{cond}) with no effect on the capillary pressure budget. This leads to an increase in the maximum subcooling limit which reduces the filmwise condensation coefficient. Thus, for the same ΔT_{max}, the

relative enhancement of h_c to $h_{Nusselt}$ is higher when gravity-driven flow supplements the pump (Figures 24c and 24d). While the effect of supplementary gravity-driven condensate flow is to increase the condensation rate and the maximum subcooling limit, the relative enhancement depends on the working fluid. As stated earlier, the pressure gradient from the capillary pressure and gravity are comparable for pentane (*i.e.*, ratio of P_{cap}/L to $\rho \cdot g \approx 1$). Hence the effect of gravity is to increase heat transfer performance $\approx 2\times$. However, for water, the corresponding ratio is > 2 since P_{cap} for water is much greater than that for pentane. Hence gravity does not have a similar impact on the enhancement of the heat transfer performance for different fluids, and the choice of fluid determines the overall performance enhancements.

With a better understanding of the factors affecting the enhancements over filmwise condensation, we briefly discuss some practical considerations in applying the proposed mode of condensation. The capillary enhanced mode of filmwise condensation may be applied to enhance the condensation process during liquefaction of gases, in liquid-vapor two phase electronics thermal management devices, and in vapor compression cycle systems. In addition to the sintered woven wire mesh used to model the wick here, alternate wick geometries include sintered particles,[45] inverse opal structures,[145] micropillar arrays[151], and hierarchical mini/micro/nanoscale wick structures. To accurately predict the operational limits for these various wick geometries, specific permeability sub-models that account for the wick geometry and dimensions will be required. In addition to the wick geometry and its pore-level dimensions, the wick thickness may also be optimized (*i.e.*, constant thickness *v/s* variable thickness) based on

the condensate removal mechanism, pump-driven or gravity-driven. When using a pump to facilitate condensate removal, a positive displacement (PD) pump may be used, however, the pump and system characteristics (defined by the required and available net positive suction head respectively, or $NPSH_R$ and $NPSH_A$) are important to the overall design. For example, the wick pore size and the maximum capillary pressure affect the $NPSH_A$, and the speed of the PD pump will determine its $NPSH_R$. Additionally, we suggest PD pumps since they are capable of suction lift, which is important in the event that transients in condensation heat transfer lead to the pump *disconnecting* from the wick. Finally, contamination and fouling (volatile and non-volatile) have the potential to impact performance in traditional phase-change systems. Volatile contaminants typically adsorb on the condenser surface and alter its wettability, however, for water and low surface tension liquids, this is not a concern since $\theta < 90°$. Non-volatile contaminants will clog the wick and reduce the effective permeability, however, this can be mitigated by adequate condenser surface preparation. The modeling framework discussed here identifies how the capillary-enhanced filmwise mode of condensation may be leveraged to increase condensation heat transfer over the traditional filmwise mode using high surface energy materials.

3.3.3 Incorporating Spatially Varying Properties for Condensation

We further incorporate the spatially varying properties (*i.e.*, meniscus curvature, liquid effective height and contact angle) into the capillary-enhanced filmwise condensation model to improve the accuracy of the prediction on HTC enhancement and

demonstrate the limitation of the model discussed in Section 3.3.2. We adopted the same micropillar array as shown in Section 3.1, since we can have better control on the geometric parameters and thus the meniscus curvature is obtained from the model reported in Section 3.1.2 and by Lu *et al.*[163] Similar to the comparison for evaporation in Section 3.2.2, we compare three different models (Figure 25a) to highlight the importance of discretization and applying local properties: (i) the non-discretized model assuming the porous media (i.e., condensate-pillar composite film) thickness as the pillar height and a uniform condensate flow velocity across the pillar array; (ii) the discretized model with a uniform effective height, which is calculated by averaging the liquid heights in the first discretized cell (*i.e.*, flat meniscus or pillar height) and in the last discretized cell (*i.e.*, the most curved meniscus obtained from the receding contact angle); and (iii) the discretized model with spatially varying effective liquid height, where each discretized cell has its individual local meniscus shape, local contact angle and corresponding effective height which result in a spatially varying permeability. Note that in literature, most analytical and semi-analytical models assume a constant effective permeability and thus a constant liquid height,[45, 145, 152, 159, 161, 162] which is similar to the first model discussed above. The average effective height from the first and the last cell in the second model is expected to give a more accurate prediction compared to using the pillar height, but the actual accuracy depends on the accuracy of the meniscus shape prediction. Accounting for the spatially-varying meniscus shape is important because the liquid vapor pressure difference increases in the direction of the condensate flow and hence leads to a larger meniscus curvature based on the Young Laplace equation (eq. 3.17). Figure 25b compares the

pressure profiles in a pillar array at a length of 25.4 mm and the pillar diameter, pitch and height of 100 μm, 300 μm and 200 μm, respectively. The near linear pressure profile for the non-discretized model is calculated using the condensate velocity which is updated from the original linear pressure gradient assumption after one iteration. Both discretized models give accurate predictions that the pressure gradient is zero at the beginning of the pillar array and the highest pressure gradient exists near the end of the pillar array. A larger deviation between the two pressure profiles is expected for short pillars since the relative difference in the effective height at each location increases as the pillar height decreases.

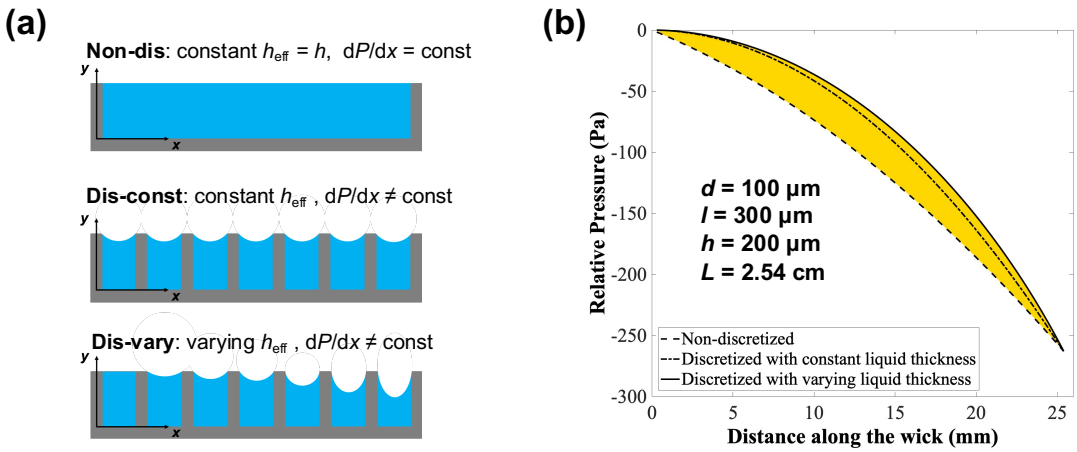

Figure 25. (a) Schematic figure of the micropillar arrays representing the non-discretized model and the discretized models with constant and varying properties. (b) Pressure profiles calculated by different models.

To emphasize the role and importance of the spatially varying effective height, we then maintain the same diameter, pitch and length of the pillar array (d = 100 μm, l = 300 μm, and L = 25.4 mm) and vary the pillar height in the model. Figure 26a presents the local HTC enhancement along the pillar array in the flow direction for three different height ratios, short, medium and tall, which we define based on the height ratio $h/(l\text{-}d)$=1,

2, and 5 respectively, to demonstrate the difference between the two discretized models with constant condensate film thickness (dashed lines) and spatially-varying condensate film thickness (solid lines). The local HTC Enhancement predicted by the two models overlap for tall pillars, which is expected because the variation in the two effective heights are negligible compared to the pillar height, or in other words, the effective heights themselves are close to the pillar height (*i.e.*, a flat meniscus height). Nevertheless, as the pillar height ratio reduces, the difference between the two models propagates and the model with constant condensate thickness leads to an overprediction in the local HTC Enhancement. Therefore, it is necessary to apply the locally varying effective liquid height to obtain an accurate prediction of the HTC Enhancement, especially for relatively short pillars. Furthermore, we demonstrate the difference between the varying height model and the constant height model by comparing the overall HTC Enhancement at different heights for d/l ratios of 1/3, 1/4 and 1/8 in Figure 26b. Similar to Figure 26a, the model with constant liquid height overpredicts the HTC enhancement noticeably at lower height ratios, and this overprediction is higher for dense pillars (*i.e.*, d/l = 1/3) due to corresponding larger area ratio AR of the actual curved meniscus to the projected area. Additionally, dense pillar arrays exhibit higher HTC enhancement, because of the larger volume of high thermal conductivity material in the condensate and surface structure composite at any given length (*i.e.*, more pillars for a dense array over a constant/fixed length of the pillar array wick), leading to a larger effective thermal conductivity and eventually the higher capillary enhanced HTC. Although increasing the d/l ratio of pillar arrays (*i.e.*, denser pillar array) improves the HTC enhancement, Figure 26c shows that

the condensation heat flux significantly decreases due to reduced condensation area (*i.e.*, liquid vapor interface) in denser arrays. Note, pillar diameter remains constant and pitch varies for different *d*/*l* ratios in Figure 26c, and the height ratio is kept constant at 1.

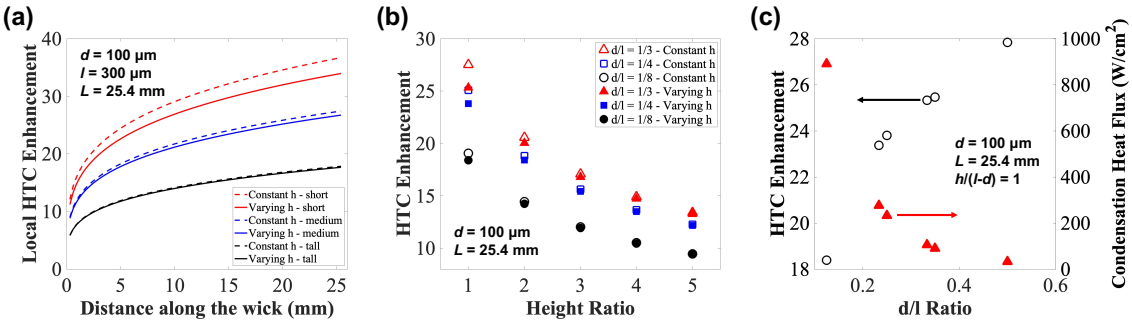

Figure 26. (a) Local HTC enhancement along the wick for geometries at different height ratio. (b) HTC enhancement for different *d*/*l* ratios. (c) HTC enhancement and condensation heat flux as functions of *d*/*l* ratios at a constant height ratio.

In the following sections, we representatively specify the thickness/height of the pillar array porous media as *wick thickness* to demonstrate the scalability of the model. In order to demonstrate the scalability of the model and the limit of predicting the HTC enhancement and maximum subcooling in a pillar array, we plot a regime map (Figure 27a) with the wick thickness and length as variables to display the maximum HTC enhancement and subcooling that can be achieved for specific geometries when using water as the working fluid. The colors represent the HTC Enhancement, the gray lines represent the maximum subcooling, and the condensate temperature is set to be 30 °C in the model. Generally, larger enhancement is achieved at small thickness and short overall length due to the smaller thermal resistance and the lower effective HTC as predicted by the Nusselt model. Quantitatively, the HTC Enhancement predicted by the model can be determined by the pillar array dimensions (*i.e.*, diameter, pitch, height, overall array

length), the condensate temperature and the condensate properties, thus the degrees of freedom for modeling HTC Enhancement for a pillar array is 6. In an actual application scenario, some parameters such as overall array length, subcooling and working fluid, may be limited by the equipment size, cooling/heating power available or required, and the required working fluid and its chemical compatibility, in which case an optimal HTC Enhancement may be determined by tuning other parameters. For example, Figure 27b shows the maximum subcooling and the HTC enhancement as functions of wick thickness for a wick length of 100 mm. Increasing the wick thickness significantly raises the maximum subcooling (black line in Figure 27b), however, the average HTC Enhancement (red line in Figure 27b) decreases as the wick thickness increases due to the larger thermal resistance of a thicker wick-condensate composite layer. Thus, a higher HTC Enhancement may be achieved by reducing the pillar height and sacrificing the maximum subcooling capability in the capillary-enhanced filmwise condensation mode without failure (*i.e.*, flooding of the pillar array). This model is scalable and provides guidance for designing the optimal surface structure geometry for enhanced condenser applications.

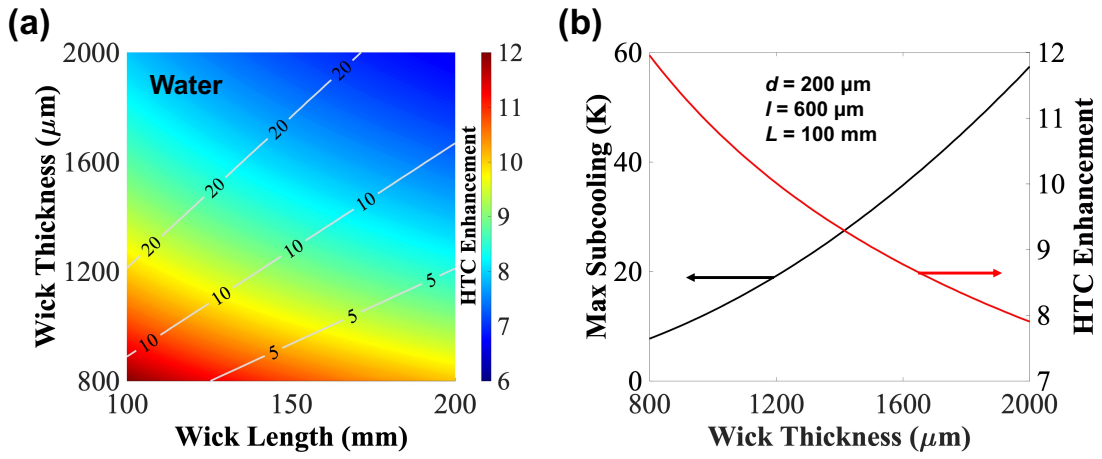

Figure 27. (a) Regime map for the HTC enhancement of water. (b) Maximum subcooling and HTC enhancement as functions of the wick thickness for a wick length of 100 mm. The geometry of the pillar array is d = 200 μm, l = 600 μm, and the condensate temperature is 30 °C.

Similar to regimes maps for water and pentane in Section 3.3.2, we demonstrate the versatility of the modeling by applying it to a few common hydrocarbon and fluorocarbon fluid refrigerants such as propane, HFE7100, R-245fa and R-134a with the same geometries in Figure 28. The magnitude of the HTC enhancement (≈18-35× compared to the traditional filmwise mode) for these refrigerants is noticeably higher than water (≈6-12×), because the lower thermal conductivity and latent heat of vaporization for these non-polar (or dielectric) fluids lead to a lower h_{Nusselt}. The maximum subcooling of these low surface tension liquids are also lower than the maximum subcooling for water because of their significantly lower latent heat of vaporization, which directly affects the maximum subcooling. Note that operating at a subcooling higher than the limit results in the failure of the capillary enhanced filmwise mode, where the pillar array is flooded by a layer of the condensate. Although the maximum HTC Enhancement cannot be achieved after flooding, some enhancement (lower than the HTC Enhancement) is possible, and this

enhancement is dependent on the thickness of the flooding condensate film which acts as a thermal resistance in series with the pillar array wick.

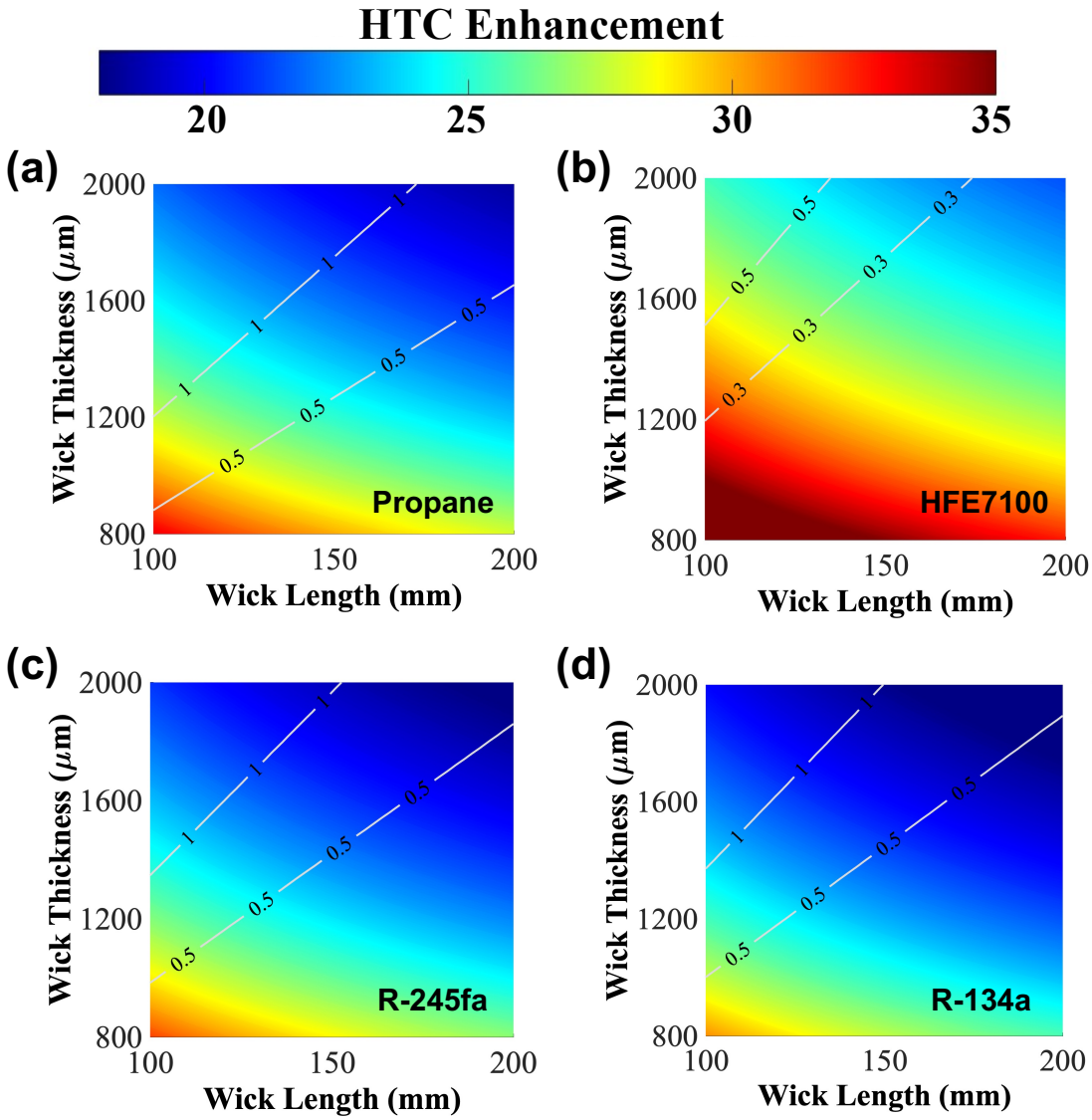

Figure 28. Regime maps predicting condensation HTC enhancement with the pillar array for various low surface tension liquids. The geometry of the micropillar array is d = 200 µm, l = 600 µm, and the condensate temperature is 30 °C.

3.4 Chapter Summary

In this chapter, we report an integrated modeling framework for solving fluid flow through porous media with accurate prediction of heat transfer characteristics during steady state liquid-vapor phase change processes (*i.e.*, condensation and evaporation). Specifically, the novel capillary-enhanced filmwise mode of condensation enables enhancement of condensation heat transfer coefficient (HTC) with low surface tension liquids, such as hydrocarbons and refrigerants, by leveraging the capillary pressure within the porous structure and the external pumping force to remove the condensate. This non-CFD based semi-analytical model is also capable of predicting the dry-out heat flux for thin film evaporation from wicks, where the prediction is validated with experimental data in literature and CFD simulations. The high accuracy of this model is facilitated by discretizing the modeling domain and capturing the spatially varying meniscus curvature, local effective liquid height and local permeability. Additionally, this model predicts the operational limits (*i.e.*, maximum heat input/dissipation) corresponding to the operational conditions (temperature, working fluid, *etc.*) for real-world engineering phase change problems in porous media. The advancements from this chapter provide guidelines to design and optimize heat exchanger material/surface structure geometric properties for liquid-vapor phase change heat transfer applications in thermal management and energy conversion systems.

CHAPTER IV

SURFACE ENERGY METHOD*

In this chapter, we report liquid-vapor phase change heat transfer enhancement techniques during water vapor condensation by improving the robustness of ultrathin low surface energy self-assembled monolayer (or SAM) coatings (*i.e.*, coating lifetime of promoting dropwise condensation) on typical metal/metal oxide materials for heat transfer applications, such as silicon and copper. The enhanced coating durability was addressed based on understanding the mechanism of coating failure/degradation (*i.e.*, transition from the efficient dropwise mode to the inefficient filmwise mode) in the process of water vapor condensation. We demonstrated the significantly prolonged SAM coating durability of promoting perfect dropwise condensation (*i.e.*, no coating failure) on both silicon (over 460 hours) and copper surfaces (over 360 hours) facilitated *via* (i) the controlled coating synthesis environment, and (ii) the stringent cleaning and surface preparation procedures. As a comparison, state-of-the-art SAM coatings on copper fail within one hour of water vapor condensation. We compared different types of coatings, separate coating conditions, diverse surface modification methods, and assorted substrate roughness levels to verify our hypothesized degradation mechanisms for silicon and copper substrates. The coating qualities were characterized by various surface characterization methods, condensation durability tests, and condensation heat transfer performance, and the pre- and post-condensation characterizations of molecular bonding and coating-substrate

* Reprinted with permission from "Elucidating the Mechanism of Condensation-Mediated Degradation of Organofunctional Silane Self-Assembled Monolayer Coatings" by Wang, R., Jakhar, K., Ahmed, S. and Antao, D.*, 2021. ACS Appl. Mater. Interfaces, 13(29): p. 34923-34934, Copyright 2021 American Chemical Society.

interfacial interactions also validated our proposed mechanisms for SAM coating degradation on silicon and copper surfaces. The work in this chapter elucidated the reasons for the formation of coating degradation nucleation sites, revealed the propagation of such defects, and reported methods to suppress the defect formation and minimize coating failure when condensing water vapor. This knowledge can be leveraged to extend the lifetime of low surface energy organofunctional silane SAM coatings in the enhanced phase change heat transfer technologies.

This chapter includes surface characterization methods, hypotheses and results on different coating conditions/environments, robust coatings on silicon substrates, and robust coatings on copper substrates. Additional unpublished results on coatings deposited on copper surfaces is currently under review:

1. Wang, R., Guo, J., Muckleroy, E. and Antao, D.*, "Robust Silane Self-Assembled Monolayer Coatings on Plasma-Engineered Copper Surfaces Promoting Dropwise Condensation"., (*In Review*)

4.1 Coating Conditions

4.1.1 Hypothesized Effect of Coating Conditions on Coating Quality

There are well known procedures to produce alkyl-silane SAMs such as vapor-phase deposition[121, 188, 189] and solvent-based deposition[69, 130, 190], however the reproducibility of these SAM coatings is still a challenge since the formation of the monolayer is extremely sensitive to reaction conditions, specifically, the water/moisture concentration in the deposition environment.[67, 68, 191, 192] Water in the synthesis environment hydrolyzes the functional groups, which leads to internal polymerization of

silane molecules to form Si-O-Si (siloxane) linkages (*i.e.*, cross-linking).[70, 71, 131, 193-195] Cross-linked structures randomly grow in both vertical and horizontal directions, forming non-uniform/rough multilayers and silane molecules agglomerates of arbitrary sizes and distributions.[131, 193, 195]

We hypothesize that the nuclei for the degradation of a SAM coating are defects in the coating resulting from: (i) cross-linking of silane molecules and the subsequent formation of agglomerates on the surface, and (ii) poor local wetting of the surface by the silane-solvent solution during the coating process. For the purpose of degradation, we define the defect or degradation nucleus as the uncoated substrate, not the cross-linked silane agglomerate. We show that the large number of defect sites resulting from an uncontrolled coating process lead to the degradation of SAMs during water vapor condensation. In an uncontrolled coating process, defect sites can form primarily by two means: (i) silane molecules hydrolyze and cross-link with each other in the presence of moisture/water in the coating environment (*e.g.*, dissolved water in base solvent and water vapor in atmosphere) and bond to the substrate in the form of bulk agglomerates that shield some regions of the substrate from un-bonded silane molecules in the solvent, and (ii) a polar or metal oxide substrate is preferentially wetted by moisture/water in the coating environment compared to the base non-polar solvent which contains the silane, leading to further shielding of the substrate from silane and cross-linking of the bonded silane molecules. For non-condensation heat transfer applications that use low surface energy SAM coatings, these large number of defects (either uncoated regions or agglomerates) formed during an uncontrolled coating process do not affect the liquid-coating interfacial

interactions beyond an observed higher contact angle hysteresis. However, this contact angle hysteresis is more likely due to randomly oriented agglomerates than any uncoated region of the substrate. We hypothesize that the actual degradation of the coating (and partial/complete removal from the substrate) during water vapor condensation is due to the dissolution of the silicon-oxygen bonds or the metal oxide-silane bonds by water and the nucleus for this reaction is the defect (*i.e.*, the uncoated substrate). The temperature and pressure gradients between the vapor and the substrate during water vapor condensation (Figure 29) actively drive water to the coating/substrate-vapor interface, which leads to water vapor penetrating the coating structural imperfections and reacting at the exposed substrate. Cross-linked silane agglomerates may partially detach from the substrate (as shown in the figure), or they are completely removed if all bonds to the substrate are broken. Steady state condensation with constant condensate shedding and re-condensation of the vapor continuously transports pure water to the defects causing the SAM coating to degrade over time due to the expanding size of the defects. Minimizing (or even eliminating) these original defect sites is essential to mitigating coating degradation and enhancing SAM coating durability during condensation of water vapor.

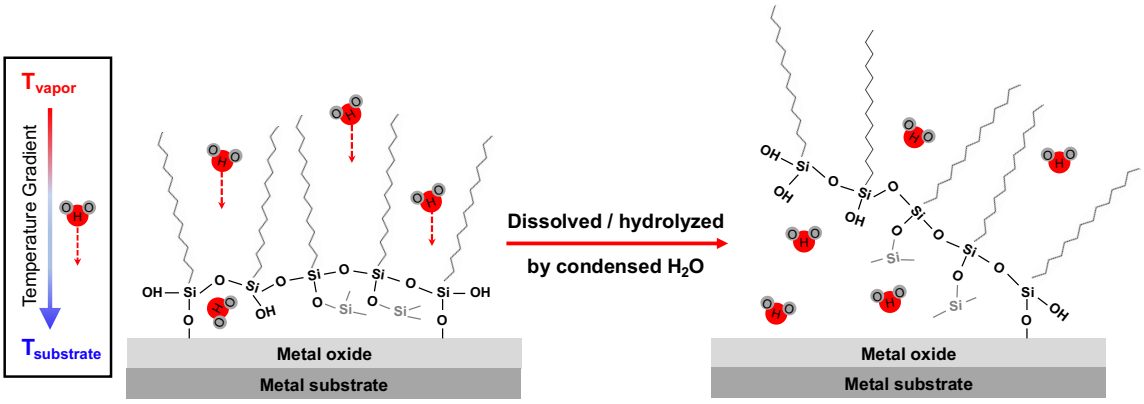

Figure 29. Schematic of degradation process of a SAM coating with defects, during water vapor condensation. Reprinted from Wang *et al.*, *ACS Appl. Mater. Interfaces.*, 2021.

Schematics of a tri-head group (specifically, TFTS) silane molecule alignment on a metal oxide substrate in an ideal case (*i.e.*, perfect alignment of SAMs bonded to the substrate; no degradation expected) are compared with those produced in a controlled coating/synthesis environment and an uncontrolled (ambient) coating/synthesis environment in Figure 30. The ideal coating situation (Figure 30a) is desirable from a degradation mitigation perspective, but highly unlikely due to the specific orientation requirements (*e.g.*, presence of gauche defects of the alkyl chain[196, 197]) for all silane molecules during the hydrolysis and surface hydroxyl/silanol bonding processes. This ideal coating is perfectly smooth with no defects or agglomerates, and hence will exhibit zero contact angle hysteresis (Figure 30b) due to the conformality of the surface hydrophobicity and tail group orientation. In a controlled anhydrous coating environment, there are minimal defects likely only caused by random SAM alignment, and this contributes to a more uniform coating with lower contact angle hysteresis (Figures 30c and 30d). In an uncontrolled coating environment, the uncoated surface defects and cross-

linked silane molecule agglomerates (Figures 30e and 30f) lead to the formation of multilayers instead of a monolayer, which results in high surface roughness and large contact angle hysteresis. Hence, in order to create conformal coatings with minimum number of defect nuclei, a controlled environment coating procedure is required. Top view and front view schematic figures of silane molecules alignment for different cases can be found in Figure 31.

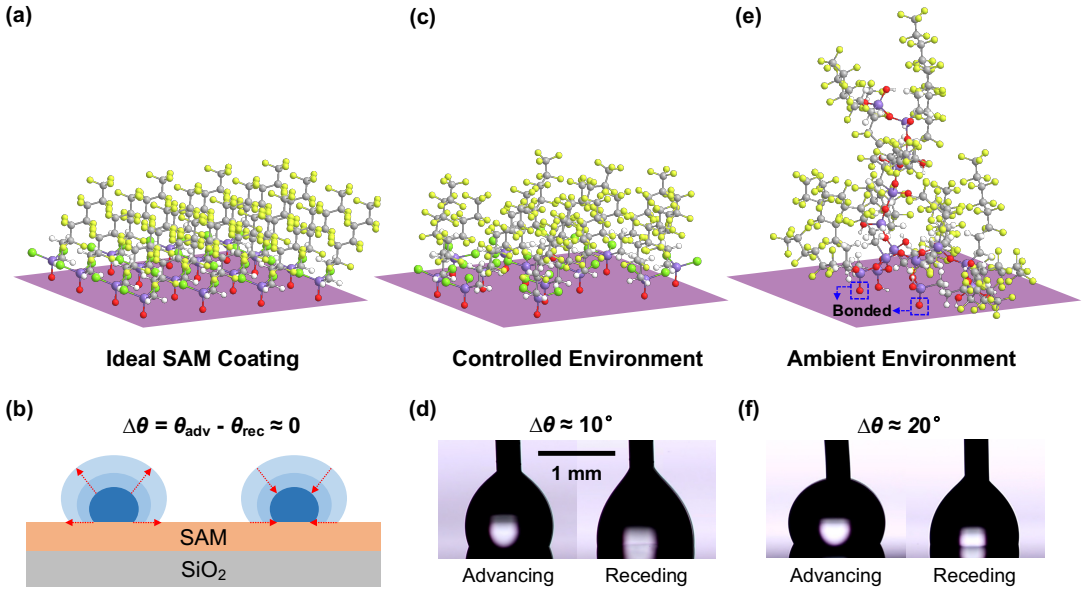

Figure 30. Schematic figures of silane molecule alignment (diagonal view) and the corresponding advancing and receding contact angles for (a, b) the ideal case, (c, d) a controlled coating, and (e, f) an uncontrolled coating. Reprinted from Wang *et al.*, *ACS Appl. Mater. Interfaces.*, 2021.

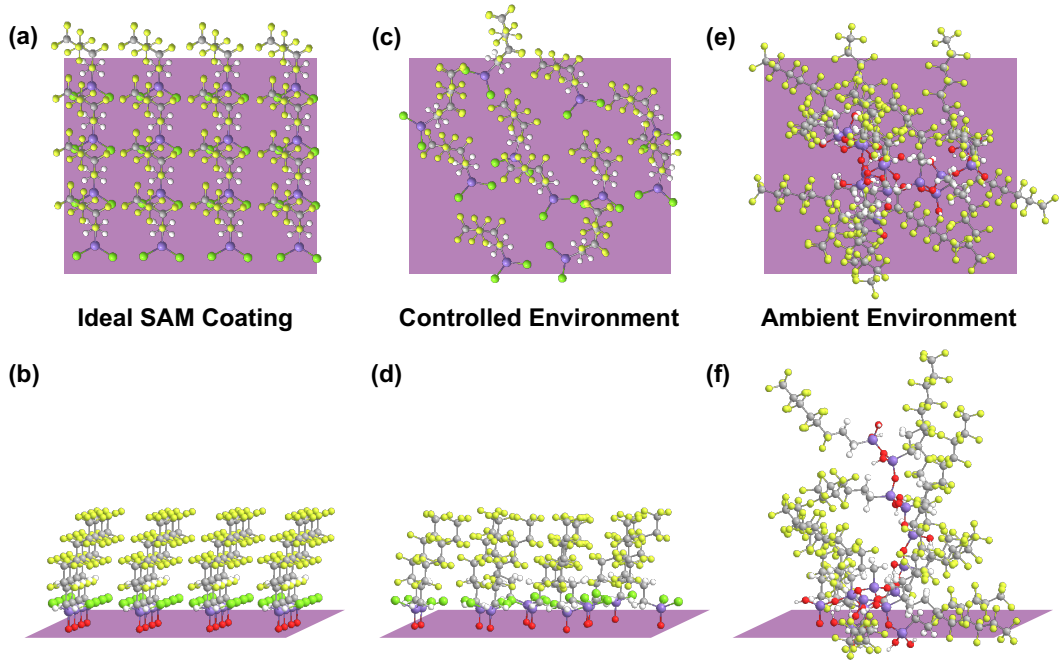

Figure 31. Top view and front view schematic figures of silane molecule alignment for (a, b) the ideal case, (c, d) a controlled coating, and (e, f) an uncontrolled coating.

4.1.2 Hypothesis Validation - Preferential Wetting of Substrate

We hypothesize that preferential wetting of the substrate by water/moisture in the coating deposition system as opposed to the silane-solvent solution leads to uncoated substrate areas. Here, we present the model of the wetting phenomena of water and hexane on the silicon substrate as an example. For an impinging liquid on a surface pre-wetted by another liquid, solid-liquid-liquid interactions dictate the impinging liquid and solid surface interaction through the spreading parameter:[15, 16, 151]

$$S_{ls(w)} = \gamma_{ws} - \gamma_{ls} - \gamma_{wl} \tag{4.1}$$

where, $S_{ls(w)}$ is the spreading parameter for the impinging liquid (*i.e.*, water) on a substrate (silicon dioxide as an example here) pre-wetted by another liquid (*i.e.*, hexane), and γ_{ws},

γ_{ls}, and γ_{wl} are the interfacial tension at water-silicon dioxide, hexane-silicon dioxide, and water-hexane interfaces, respectively. Note that this analysis assumes that all the interacting materials are immiscible, which is true at the macroscale and the relatively short timescales during coating procedures for the water-hexane-silicon dioxide system. These interfacial tension values are calculated by the van Oss, Chaudhury and Good (vOCG) approach of surface tension components, with both Lifshitz-van der Waals (LW) and polar (acid base) contributions:[111, 112, 198]

$$\gamma_{12} = \gamma_1^{LW} + \gamma_2^{LW} - 2\sqrt{\gamma_1^{LW}\gamma_2^{LW}} + 2\sqrt{\gamma_1^{+}\gamma_1^{-}} + 2\sqrt{\gamma_2^{+}\gamma_2^{-}} - 2\sqrt{\gamma_1^{+}\gamma_2^{-}} - 2\sqrt{\gamma_1^{-}\gamma_2^{+}} \qquad (4.2)$$

where, γ^{LW} is the Lifshitz-van der Waals (LW) component for the substance, and γ^{+} and γ^{-} are the Lewis acid and base (A-B) components, respectively. The subscripts 1 and 2 indicate two different materials/substances. For water making contact with a silicon dioxide surface pre-wetted by hexane, the criteria for water to displace hexane from the silicon dioxide substrate is given by:[151]

$$S_{ls(w)} + \gamma_{wl} \times R \leq 0 \qquad (4.3)$$

where, R is a geometric factor defined as $R = (r\text{-}1)/(r\text{-}\phi)$ varying from 0 (perfectly smooth surface) to 1 (extremely rough surface), r is the surface roughness (*i.e.*, the ratio of actual surface area to projected surface area), and ϕ is the solid fraction. Table 4 lists the values of the LW and A-B components for water, hexane, and silicon dioxide, and we show that water impinging on a silicon dioxide substrate pre-wetted with hexane will displace hexane (satisfying the criterion in eq. 4.3). For an atomistically smooth silicon dioxide surface which has been treated/cleaned in piranha solution, the geometric factor R should be 0, however we evaluate the criteria in eq. 4.3 assuming $R = 0.1$ as a conservative

estimate. In Table 4 we also present the calculated water-displacing criteria for other commonly used solvents in alkyl/fluoro-silane SAMs deposition processes. This analysis indicates that when water is present in the coating environment, either in the form of ambient water vapor adsorbing to the surface or dissolved water in non-anhydrous hexane, water will displace hexane and preferentially wet the silicon substrate. This will prevent silane molecules dissolved in the hexane solvent from bonding to the substrate at these water-occupied regions, and will result in a non-uniform layer. The presence of water in the coating system will also lead to the formation of agglomerates of cross-linked and hydrolyzed silane molecules, which will result in multilayer coatings instead of monolayers.

Table 4. Total surface tension, and the Lifshitz-van der Waals (LW) and Lewis acid-base (A-B) components for silicon dioxide (an example substrate), water and commonly used solvents in alkyl/fluoro silane SAMs deposition processes.

	γ^{Total} (mN/m)	γ^{LW} (mN/m)	γ^{+} (mN/m)	γ^{-} (mN/m)	$S_{ls(w)} + \gamma_{wl} \times R$	Displacement
Silicon dioxide	59.8	42.0	2.0	40.2	N/A	N/A
Water	72.8	21.8	25.5	25.5	N/A	N/A
Hexane	18.4	18.4	0	0	-74.87	Yes
Cyclohexane	25.24	25.24	0	0	-72.17	Yes
Toluene	28.5	28.5	0	0.72	-61.53	Yes
Chloroform	27.2	27.2	1.5	0	-45.14	Yes
Chlorobenzene	33.6	32.1	0.9	0.61	-44.35	Yes

To experimentally validate this semi-empirical analysis, we demonstrate that water can displace hexane from a silicon dioxide (SiO_2) surface (Figure 32). We filled a quartz (crystalline SiO_2) cubic cell with pure anhydrous hexane, and water (dyed red with Pylam

Pylaklor Dark Red LX-10659) was dispensed through a gauge 30 needle (outer diameter ≈0.312 mm) onto the SiO_2 surface. Figures 32a and 32b showed the side view and the front view of water droplets wetting the SiO_2 surface immersed in a hexane bath, and as additional water was infused through the needle, the water droplet first displaced hexane from the SiO_2 surface, and then preferentially wetted and spread on the SiO_2 surface (Figure 32c).

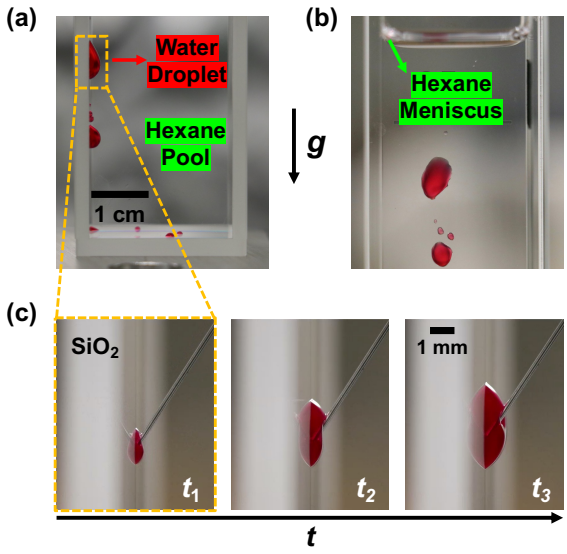

Figure 32. Liquid displacement experiments showing the wetting preference of water over hexane on a silicon dioxide (SiO_2) surface. Reprinted from Wang *et al.*, *ACS Appl. Mater. Interfaces.*, 2021.

4.1.3 Hypothesis Validation - Coating Synthesis Procedure

To test the second component of our hypothesis, we performed coating procedures in an anhydrous environment (*i.e.*, a nitrogen glovebox, H_2O < 0.1 ppm) with anhydrous solvents, and an ambient environment (*i.e.*, a chemical fume hood) with both anhydrous and non-anhydrous solvents. Test samples created *via* these methods are labeled as

"controlled", "ambient-A" and "ambient-NA", respectively. The step-by-step synthesis procedure in both the controlled and ambient conditions are reported below, and we used silicon as an example substrate for this demo.

Controlled condition: Coating procedures in the controlled (dry) environment were performed in a glovebox (UNILab pro SP, MBraun, H_2O <0.1 ppm, O_2 <0.1 ppm) with anhydrous chemicals. All glassware and tweezers were first rinsed (two times) with the anhydrous hexane solvent before using them. The silane coating solution (1 mMol/L) was prepared by adding the silane (*i.e.*, either TFTS or OTCS) to the anhydrous hexane solvent, and heating up the solution to 60°C. This temperature is sufficiently high to accelerate silane dissolution, but lower than the boiling point of hexane to avoid any loss of the solvent. We then immersed the samples in the solution and maintained the solution at 60°C for 1 hour. After removing the samples from the coating solution, the silane-coated samples were immersed in multiple baths of anhydrous hexane to remove any excess silane molecules on the surface, and subsequently annealed in a vacuum oven (P < 1 kPa) at 100°C for 1 hour to evaporate any unbounded silane molecules.

Ambient condition: Coating procedures in the uncontrolled ambient condition were performed in a fume hood with both anhydrous and non-anhydrous solvents. After the standard cleaning procedure mentioned above, all glassware and tools were first rinsed with the corresponding hexane two times before using them. The coating procedures and operation protocol remained the same as the controlled condition described above. After removing the coated samples from the silane coating solution, the samples were immersed into multiple baths of the corresponding hexane solution (*i.e.*, anhydrous or

non-anhydrous, depending on the solvent used in the silane coating solution) to remove excess silane molecules on the surface, and subsequently annealed in a vacuum oven (P < 1 kPa) at 100°C for 1 hour to evaporate unbounded silane molecules. For this ambient condition coating procedure, the anhydrous hexane was stored in the glovebox, and was only transferred out of the glovebox to the fume hood in beakers when needed. The typical exposure time for the anhydrous hexane to the ambient atmosphere (period of transferring the hexane) was typically <3 minutes prior to the start of the coating procedure.

4.1.4 Hypothesis Validation - Characterization of Coating Properties/Quality

In this section, we characterize and compare the properties of SAM coatings (TFTS and OTCS) deposited on silicon substrates in the controlled and the ambient conditions with both anhydrous and non-anhydrous solvents to highlight the effect of coating environment on coating quality. Both TFTS and OTCS SAMs prepared in the anhydrous/controlled environment exhibited minimal RMS roughness (or *Rq*, as shown in Figures 33a and 33d) obtained with AFM, the smallest coating thickness (measured *via* ellipsometry), and the lowest contact angle hysteresis (CAH). This true self-assembled monolayer synthesized in a controlled and anhydrous environment is very different from the coatings synthesized in ambient conditions with anhydrous (Figures 33b and 33e) and non-anhydrous solvents (Figures 33c and 33f), both of which exhibit larger RMS roughness, coating thickness, and a higher CAH. The OTCS ambient-NA sample has the highest RMS roughness and coating thickness, while the TFTS ambient-NA sample shows

the same level of RMS roughness and coating thickness as the TFTS ambient-A sample. This variation in the expected trend between the ambient-A and ambient-NA samples may result from the uncontrolled water concentration in the solution, given that both are prepared in an uncontrolled/ambient environment. Specifically, the RMS roughness, contact angles hysteresis, and ellipsometry thickness for samples shown in Figure 33 are reported below and also summarized in Table 6 in Section 4.3.4: TFTS controlled (Rq = 0.319 nm, CAH = 10.2°, thickness = 0.6±0.1 nm), TFTS ambient-A (Rq = 1.170 nm, CAH = 18.7°, thickness = 1.4±0.1 nm), TFTS ambient-NA (Rq = 0.624 nm, CAH = 21.4°, thickness = 1.1±0.2 nm), OTCS controlled (Rq = 0.416 nm, CAH = 7.3°, thickness = 1.5±0.0 nm), OTCS ambient-A (Rq = 0.811 nm, CAH = 15.5°, thickness = 1.6±0.2 nm) and OTCS ambient-NA (Rq = 2.28 nm, CAH = 21.8°, thickness = 2.1±0.1 nm).

Overall, the comparison of coatings resulting from synthesis procedures in a low moisture content environment (*i.e.*, the glovebox) and an unregulated moisture content environment (*i.e.*, the fume hood) clearly indicate that silane molecules cross-link and grow into disordered multilayers (*i.e.*, rougher and thicker self-assembled layers with silane agglomerates) instead of monolayers due to the existence of water in the environment. These agglomerate defects likely contribute to the higher measured contact angle hysteresis.

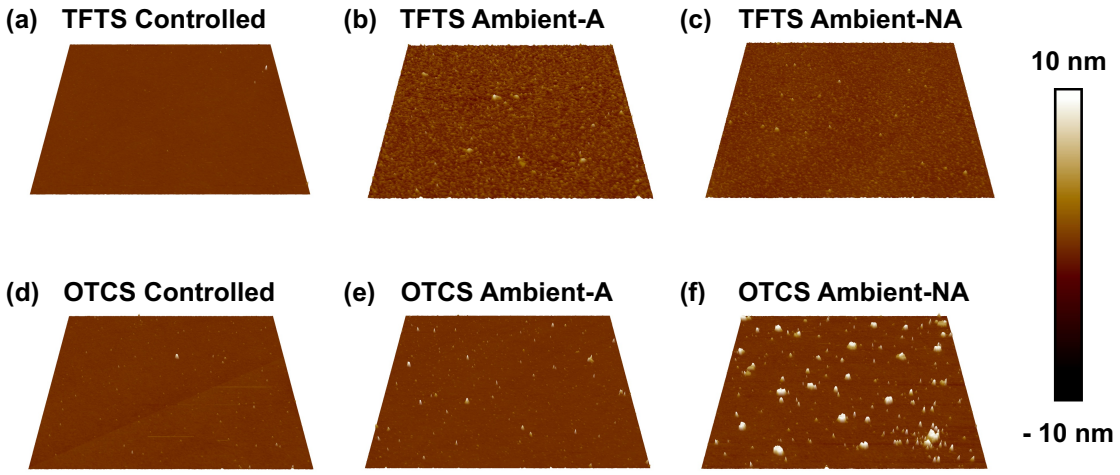

Figure 33. Surface topographies of 10 µm × 10 µm areas obtained with AFM for TFTS and OTCS coatings prepared in the controlled and ambient conditions and with anhydrous and non-anhydrous solvents after coating integration. Reprinted from Wang *et al.*, *ACS Appl. Mater. Interfaces.*, 2021.

Additionally, we compare the carbon profiles of an OTCS coating deposited in the controlled condition and a bare silicon wafer cleaned by piranha solution in Figure 34. Only a C-C bond peak is detected for the OTCS controlled sample, but the silicon wafer indicates both C-C bond and C-O bond. Contamination from ambient (*i.e.*, dust or volatile hydrocarbons in the environment) tends to adsorb onto high surface energy materials such as the piranha cleaned silicon wafer compared to a low surface energy coating. This leads to the appearance of the C-O bond in the XPS spectra for the piranha cleaned silicon substrate. The comparison also verified that OTCS deposited in the controlled condition is a pristine low surface energy coating.

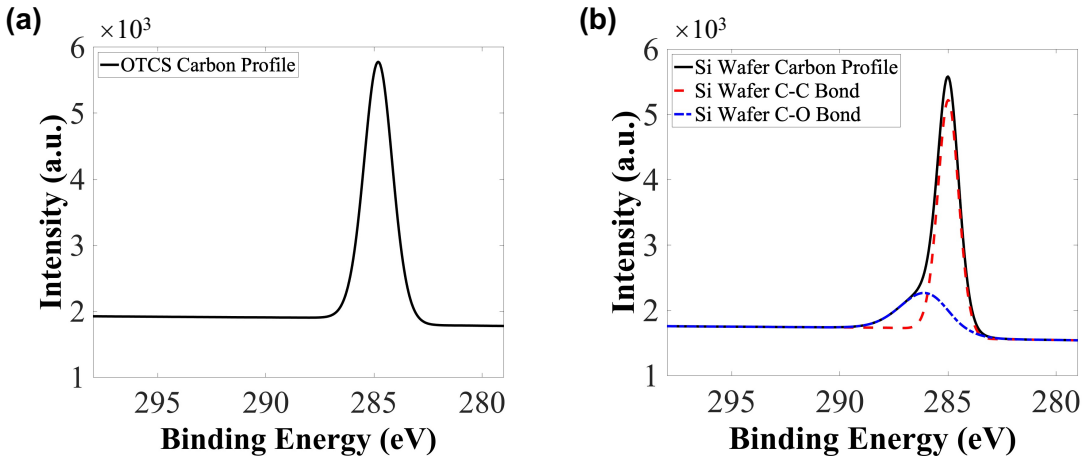

Figure 34. XPS carbon peaks of (a) an OTCS controlled sample and (b) a piranha cleaned silicon wafer.

4.2 Surface Characterization Methods

4.2.1 Contact Angle Measurement (CAM)

Contact angles were measured using a customized goniometry setup (Figure 35a) comprising a syringe pump (NE-1010, New Era Pump Systems, Inc.) and a camera (EOS 80D, Canon) with a macro lens (MP-E 65 mm, Canon). The sample was placed (accuracy in horizontal direction ≈0.1°) on the measurement stage, and water was infused and withdrawn through a 30 gauge needle (≈0.312 mm outer diameter) at a flow rate of ≈20 µL per minute. At this flow rate, no noticeable vibration of the needle was observed. The droplet diameter was maintained less than the capillary length of water (*i.e.*, 2.7 mm) to minimize the effects of gravity. Videos of droplet infusion and withdrawal were recorded with the camera at 60 Hz to characterize the advancing and receding contact angle, respectively. The contact angles were calculated by fitting a vector parametrized cubic spline over the digitized profile of the droplet.[199] The advancing and receding contact

angles were determined based on measurements of 4 different batches of coated samples and at 4 different locations on each sample. Additionally, left- and right-side contact angles were treated as separate droplets, since the advancing (and receding) did not necessarily occur at the same time for both the left- and right-side contact points.

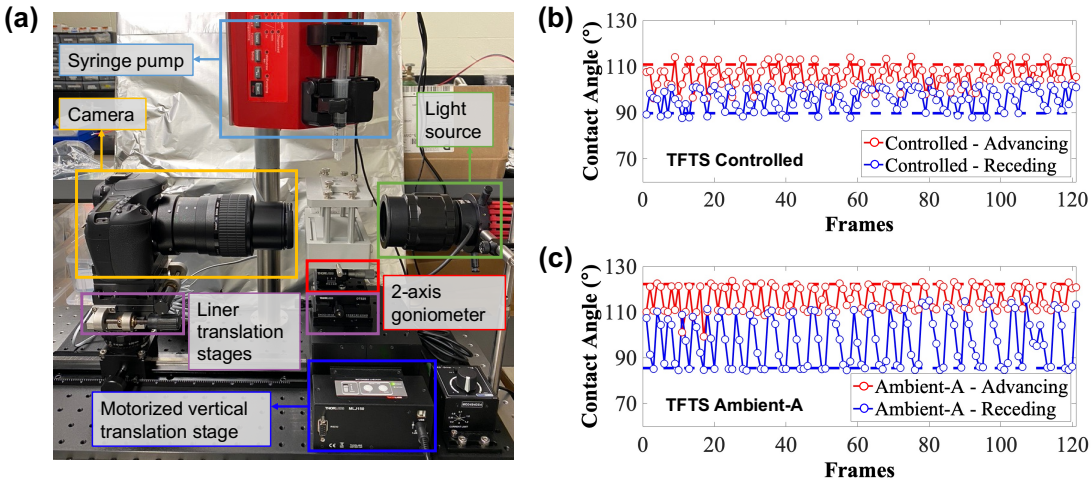

Figure 35. Image of (a) the experiment setup for contact angle measurement. Profiles of the advancing and receding contact angles for (b) TFTS controlled and (c) TFTS ambient-A samples.

We recorded the process of droplet infusion and withdrawal at 60 Hz for each measurement and selected 2 seconds of video each for the advancing and receding contact angle measurements. A total of 121 frames are captured and analyzed, and then the contact angles can be plotted as a function of time (or frame number). All contact angle profiles exhibit some level of fluctuation (or standard deviation), leading to different methods of defining the advancing and receding contact angles. For example, the advancing and receding contact angles, calculated by averaging all frames, for TFTS controlled samples (Figure 35b) are 105.2° ± 5.0° and 95.0° ± 5.0° (CAH =10.2°), while averaging the peaks and troughs of the profile leads to 110.9° ± 2.8° and 89.8° ± 2.8°

(CAH =21.1°) for the advancing and receding angles, respectively. While for TFTS ambient-A samples (Figure 35c), the average advancing and receding contact angles are 114.6° ± 7.1° and 95.9° ± 10.5° (CAH =18.7°), while averaging only the peaks and troughs gives 122.3° ± 2.8° and 85.5° ± 2.3° (CAH =36.8°). The method of using the peaks and troughs provides a conservative definition of the contact angles and contact angle hysteresis. The method of averaging all the data (*i.e.*, advancing mode and receding mode, separately) is commonly used to obtain the contact angles and the contact angle hysteresis, and it does lead to a lower contact angle hysteresis. However, such an approach (*i.e.*, averaging all data) does not represent the true local behavior since the advancing angle is the maximum angle as a droplet advances on a surface and the receding angle is the minimum angle as the droplet recedes on the surface. Hence the peaks and troughs method presented here provides a more conservative indicator of the surface characteristics. To justify this evaluation method, consider the droplet advancing process on a hydrophobic surface. As water is infused into the droplet and the droplet grows, the contact line typically de-pins and pins at surface heterogeneities as opposed to smoothly and constantly growing and moving (un-impeded) on the surface. Thus, for advancing droplets, the peak locations are where the droplet overcomes the maximum local energy barrier, and therefore, the contact line de-pins and moves. Similarly, the trough locations are where the receding droplet overcomes the minimum local energy barrier, and the contact line de-pins and moves. The peaks and troughs method enables reporting of conservative advancing and receding contact angles, as well as contact angle hysteresis with minimum measurement uncertainty, and it is possible due to the higher frequency (or frame rate)

image capture. Note that the averaging method commonly reported in literature using the same high frequency image capture process can provide similar conservative uncertainty bounds if higher order standard deviations (*e.g.*, 2σ, 3σ, or 4σ) are reported as the uncertainty. However, low frequency image capture during the advancing or receding processes may miss these local pinning and de-pinning events.

4.2.2 Atomic Force Microscopy (AFM)

Surface topography and roughness were measured with an AFM instrument (Dimension Icon AFM, Bruker) in the tapping mode to minimize any physical damage to the samples (compared to the contact mode) and eliminate ambient interference (*e.g.*, humidity/moisture). AFM cantilevers (HQ:NSC35/Al BS) with a cone angle of ≈40° and a tip radius <8 nm were used for scanning. The resonance frequencies were 150-300 kHz, and the spring constants were 5.4-16 N/m (for three different tips on one cantilever).

Adhesion forces were characterized using the same AFM in the peak force QNM (quantitative nanomechanics) mode. This mode directly controls the maximum peak normal force and minimizes the lateral forces on the probe. A rectangular AFM cantilever (RTESPA-150) was used for adhesion measurements. For these adhesion measurements, the tip radius is less than 8 nm, it has a resonance frequency of ≈150 kHz, and the spring constant is 5 N/m. The adhesion force measurements are highly dependent on the probe deflection sensitivity calibration which is affected by laser position on the cantilever and the prevailing environmental conditions such as humidity and temperature. For example, the calibration sensitivity we obtained for three different calibrations are 84.62 ±

0.51 nm/V, 73.67 ± 0.35 nm/V and 69.15 ± 0.02 nm/V, with the same peak force set point. Given this large variation in the sensitivity calibration, the reported adhesion force comparisons were obtained on the same date to ensure consistent comparisons of data, with the measured adhesion forces being relative values instead of absolute values.

AFM images were obtained in ambient conditions at a scan rate of 0.5 Hz and 256 lines per scan. The data was analyzed using NanoScope Analysis 1.9 to calculate the root mean square (RMS) roughness (*Rq*). Roughness values reported are based on scanning 3 samples and at least 3 different locations on each sample (a total of 9 measurements).

4.2.3 X-ray Photoelectron Spectroscopy (XPS)

An Omicron XPS system with a DAR 400 dual Mg/Al X-ray source was utilized to identify the materials (*e.g.*, CuO, Cu_2O, SiO_2) and chemical bonds (*e.g.*, metal oxide, metal hydroxide, CF_2, CF_3, C-O, C=O), and to measure the elemental compositions at the sample surface. XPS measurements were performed at a take-off angle of 40.05°, and at an analysis chamber pressure of 1.33×10^{-6} Pa. The emission current is 20 mA for the X-ray and the anode voltage is 15 kV, resulting in a total of 300 W of X-ray power. The constant analyzer energy (CAE) was set to be 20 eV for carbon and silicon, and 50 eV for copper, oxygen and fluorine. The dwell time was 0.1 s for copper, silicon and fluorine, and was adjusted to be 0.15 s for carbon and oxygen to improve the signal-to noise ratio (S/N) given the low amount of carbon on clean surfaces. To reduce charging on the sample, a CN10 charge neutralizer has an emission current of 10 μA and a beam energy of 2 eV. XPS measurements were typically conducted within one hour for the uncoated

samples after preparation (*i.e.*, polishing, chemical oxidation and plasma treatment), to minimize airborne contamination. For the coated samples, XPS analyses were conducted 3 days after the samples were prepared or removed from the condensation experiment, to enable other characterizations (*e.g.*, contact angle measurements and AFM) which needed to be performed prior to XPS measurements. XPS results were analyzed with CasaXPS to fit various peaks for each element and calculate the atomic ratios.

4.2.4 Ellipsometry

The thickness of the silane coating was measured on a coated silicon substrate with an ellipsometer (EP3-SE, Nanofilm Surface Analysis). The wavelength of the incident light was 630.5 nm, and the angle of incidence was 42°. The silane coating was assumed to have the same refractive index (as a function of wavelength) as silicon dioxide.[123, 128, 130] The thickness of native oxide was first measured, and then the total thickness of native oxide layer and silane layer was measured. The difference between the two is the thickness of the silane coating. In order to ensure consistency, the native oxide measurement sample and the silane coated sample were from the same wafer, and they were stored together and cleaned in the piranha solution at the same time. The thickness and +/- values were based on measurements at 4 different locations on each sample. The thickness of silane coatings on copper surfaces are assumed to be the same as the monolayer coatings deposited on silicon substrates.

4.2.5 Fourier-Transform Infrared (FTIR) Spectroscopy

Fourier Transform Infrared (FTIR) spectroscopy (Nicolet 380, Thermo Fisher Scientific) was used in the transmission mode in the open ambient laboratory environment to identify the silane SAM chemical bonds. A piranha cleaned double side polished silicon wafer was used as the background to obtain the absorbance of the SAMs coating over the spectral range ≈4000-1000 cm^{-1}. 128 scans were taken and averaged in each measurement to minimize the S/N. The resolution of the spectrometer is 4 cm^{-1}, resulting in a relatively large data spacing of 1.9 cm^{-1} (*i.e.*, each data point on the spectrum is 1.9 cm^{-1} away from the next).

4.2.6 Condensation Heat Transfer Tests

Water vapor condensation heat transfer experiments were conducted in a vacuum-capable environmental chamber (Figure 36a) with a measured leak rate less than 1.5 Pa/hr. Aluminum cold plate heat sinks were used to remove the heat of condensation for flat samples tested, and the test samples (coated silicon wafer and copper sheets) were mounted of the heat sink using carbon tape. Coolant water pumped through the cold plate was supplied by a refrigerated chiller (K6, Applied Thermal Control). Calibrated stainless steel probe thermocouples (SCPSS-062U-SHX, Omega Engineering) were used to measure the temperature at various locations inside the chamber (*i.e.*, vapor, sample surface and condensate) and to monitor the coolant temperature. The chamber pressure was measured with a Baratron® capacitance manometer (628F13TBE2B, MKS Instruments), and a Micro Pirani pressure transducer (925, MKS Instruments) was used to ensure that the chamber pressure was 10^{-3} Pa or lower before the start of each experiment.

Water was degassed and maintained in the degassed state in a high-vacuum sealed boiler. Degassing was performed by first heating up the boiler to 100°C with the vent valves open to atmosphere, maintaining the active boiling state for ≈30 seconds, and subsequently pulling vacuum on the boiler vapor space for at least 30 seconds with the vent valves closed. The vapor pressure in the boiler after degassing matched the saturation pressure of the liquid/vapor water temperature, within the measurement uncertainties, indicating a degassed state.

For the durability testing of the coated silicon wafers, the coolant was supplied through a cold plate insulated by customized Macor® ceramic pieces (Figure 36b) at a volumetric flow rate of 1.8±0.1 L/min measured using a liquid flow meter (L-5LPM-D/5V, Alicat Sci.) placed at the return line to the chiller. For copper substrates, the flow rate was adjusted to be 3.1±0.1 L/min measured by a different flow meter (FLR1012, Omega Engineering) due to the size difference of the cold plate for the coated copper substrates, and this cold plate was insulated with Kapton® polyimide plastic tape. Once the environmental chamber was evacuated and the coolant temperature and flow rate reached steady state, degassed water vapor was introduced into the chamber at 100°C for ≈30 mins in order to add sufficient water to the system that acts as the vapor source for the long term testing. The system temperature was controlled *via* PID controllers connected to multiple ultra-thin polyimide heaters and wire heaters attached to the chamber body, viewports, door, and chamber stand/base. To achieve steady state of the system, heat input via the chamber body heaters and heat removal by the chiller had to balance, and steady state (*i.e.*, sample surface temperature did not vary by more than

≈0.2°C and the saturation pressure did not vary by more than ≈0.2 kPa) was achieved within 1.5 hours.

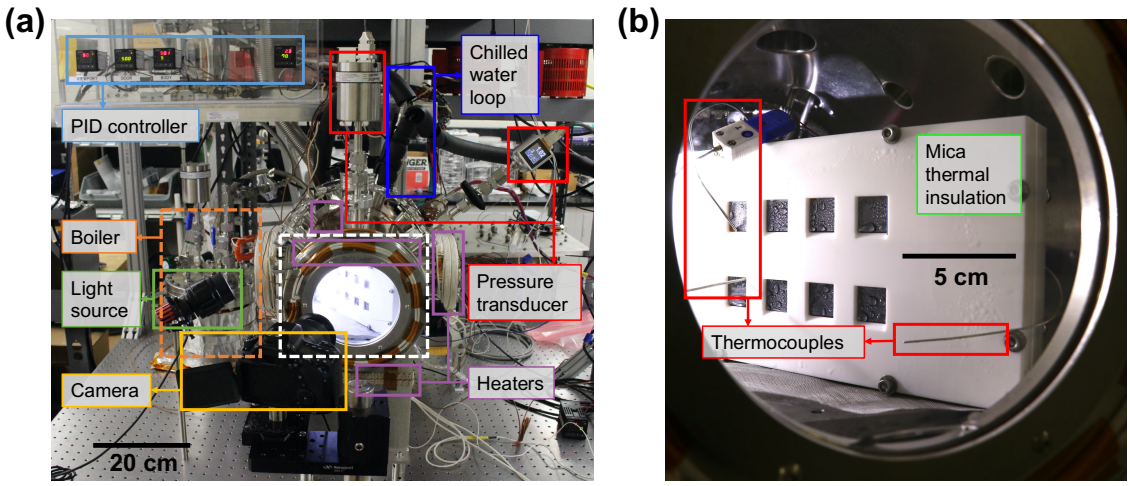

Figure 36. Images of (a) the experimental test setup for the long-term water vapor condensation tests, and (b) the cold plate for testing the coated silicon samples.

In order to obtain an accurate measurement of condensation heat transfer characteristics, we used TFTS-coated copper tubes and supplied a higher coolant volumetric flow rate ≈4.9±0.1 L/min to lower the internal convection resistance and thus make the measurement uncertainty more sensitive to the condensation HTC. While pure water vapor was introduced into the testing chamber at 100°C, the valve to the vapor line was kept slightly open during the experiment to provide extra heating power to the system. The wet-bulb temperature was sustained at a constant value (≈48.5°C, standard deviation <0.1°C) throughout the experiment by gently tuning the vapor line valve. The coolant temperature was varied from 45°C to 30°C to obtain a wide range of subcooling, and the data were recorded when the steady state was reached after each coolant temperature adjustment. The pressure in the condensation chamber always matched the saturation

pressure (standard deviation <0.02 kPa) calculated by the wet-bulb temperature, indicating that no non-condensable gases (NCGs) were present in the system.

4.2.7 Condensation Heat Transfer Calculation and Uncertainty Analysis

To estimate the condensation heat transfer rate/performance, we measured the sensible coolant temperature difference in the heat exchanger (*i.e.*, the copper tube) and the flow rate of the coolant (water) through it. The heat flux is given by:

$$q'' = \frac{\dot{m}_{\text{coolant}} \cdot c_{\text{p}}}{A_{\text{o}}} \cdot \left(T_{\text{out}} - T_{\text{in}} \right) \tag{4.4}$$

where q'' is the condensation heat flux, $\dot{m}_{\text{coolant}}$ is the mass flow rate of the coolant, c_{p} is the specific heat capacity at the average coolant temperature, A_{o} is the tube outer surface area where condensation occurs, and T_{out} and T_{in} are the coolant outlet and inlet temperatures, respectively. We calculate the overall heat transfer coefficient, $\bar{U}$ as:

$$\bar{U} = \frac{q''}{\Delta T_{\text{LM}}} \tag{4.5}$$

where, ΔT_{LM} is the logarithm mean temperature difference (or LMTD) defined as:

$$\Delta T_{\text{LM}} = \frac{\left(T_{\text{v}} - T_{\text{in}} \right) - \left(T_{\text{v}} - T_{\text{out}} \right)}{\ln\left[\frac{\left(T_{\text{v}} - T_{\text{in}} \right)}{\left(T_{\text{v}} - T_{\text{out}} \right)} \right]} \tag{4.6}$$

where, T_{v} is the vapor temperature (*i.e.*, the wet-bulb temperature). The subcooling ($\Delta T_{\text{subcooling}}$) is estimated *via* a 1-D thermal resistance network from the vapor to the coolant (and neglecting the thermal resistance of the ≈0.7 nm thick coating):

$$\Delta T_{\text{subcooling}} = T_{\text{v}} - \left[T_{\text{coolant}} + \frac{q'' \cdot A_{\text{o}} \cdot \ln\left(d_{\text{OD}}/d_{\text{ID}}\right)}{2\pi \cdot L \cdot k} \right] \tag{4.7}$$

where, T_{coolant} is the average coolant temperature in the tube, d_{OD}, d_{ID} and L are the outer diameter, inner diameter and length of the copper tube exposed to water vapor, respectively, and k is the thermal conductivity of the tube material (*i.e.*, 339 W/m·K for copper 122).

The condensation heat transfer coefficient, h_{c}, is calculated based on a similar 1-D thermal resistance network:

$$h_{\text{c}} = \left[\frac{1}{\bar{U}} - \frac{A_{\text{o}}}{A_{\text{i}} \cdot h_{\text{conv}}} - \frac{A_{\text{o}} \cdot \ln\left(d_{\text{OD}}/d_{\text{ID}}\right)}{2\pi \cdot L \cdot k} \right]^{-1} \tag{4.8}$$

where, A_{i} is the tube inner surface area in contact with the coolant, and h_{conv} is the coolant convection heat transfer coefficient given by the Gnielinski correlation:[141, 184]

$$h_{\text{conv}} = \frac{k_{\text{l}}}{d_{\text{ID}}} \frac{\left(\frac{f}{8}\right)\left(Re - 1000\right)Pr}{1 + 12.7\left(\frac{f}{8}\right)^{\frac{1}{2}}\left(Pr^{\frac{2}{3}} - 1\right)} \tag{4.9}$$

where, k_{l} is the coolant thermal conductivity, Re and Pr are the Reynolds number and Prandtl number, respectively, and f is the pipe friction factor given by:

$$f = \left(0.790 \ln\left(Re\right) - 1.64\right)^{-2} \tag{4.10}$$

We performed a detailed uncertainty analysis for all parameters in our heat transfer measurements including the independent parameters (*i.e.*, temperature, pressure and volumetric flow rate) and the dependent parameters (*e.g.*, heat flux and heat transfer coefficient). The overall uncertainty of each independent parameter comprises the device

accuracy (*i.e.*, a calibration uncertainty or manufacturer/device stated accuracy), one standard deviation of all measured data points (*i.e.*, 3 data points per second for at least 180 seconds in each data set), and the data acquisition card uncertainty. The uncertainties from device calibration and the data acquisition card are reported in Table 5, and the detailed uncertainty analysis procedure is listed in eqs. 4.11-4.22 below based on the analysis reported in Antao *et al.* for internal flow condensation of water.[141]

Table 5. Uncertainties from calibration/device accuracy for each measurement type and the data acquisition (DAQ) card for independent measured parameters.

Measurement Type	Uncertainty
Temperature (calibration- thermocouple, T-type), °C	0.02
Temperature (DAQ), °C	0
Pressure (manufacturer- transducer), kPa	0.25% of reading
Pressure (DAQ), kPa	0.002
Volumetric flow rate (manufacturer- flowmeter), m^3/s	1% of reading
Volumetric flow rate (DAQ), m^3/s	0
Convection correlation (Gnielinski)	5%

The uncertainty in independent (*i.e.*, temperature, pressure, coolant volumetric flow rate) variables are given by:

$$w_T = \left[\left(T_{UNC}\right)^2 + \left(T_{STD}\right)^2 + \left(T_{DAQ}\right)^2 \right]^{1/2}$$
$$w_P = \left[\left(P_{UNC}\right)^2 + \left(P_{STD}\right)^2 + \left(P_{DAQ}\right)^2 \right]^{1/2} \quad (4.11)$$
$$w_V = \left[\left(V_{UNC}\right)^2 + \left(V_{STD}\right)^2 + \left(V_{DAQ}\right)^2 \right]^{1/2}$$

where, w is the uncertainty, and the subscripts T, P and V represent temperature, pressure and coolant volumetric flow rate, respectively. The uncertainty in the pressure is only

used to check and validate the absence of non-condensable gases or NCGs. The uncertainty in the coolant flow temperature difference (T_{out} - T_{in}) is given by:

$$w_{\Delta T_{flow}} = \left\{ \left[\frac{\partial \left(\Delta T_{flow} \right)}{\partial T_{out}} \cdot w_{T_{out}} \right]^2 + \left[\frac{\partial \left(\Delta T_{flow} \right)}{\partial T_{in}} \cdot w_{T_{in}} \right]^2 \right\}^{1/2} \tag{4.12}$$

where,

$$\begin{aligned} \frac{\partial \left(\Delta T_{flow} \right)}{\partial T_{out}} &= 1 \\ \frac{\partial \left(\Delta T_{flow} \right)}{\partial T_{in}} &= -1 \\ w_{T_{out}} &= \left[\left(T_{out\text{-}UNC} \right)^2 + \left(T_{out\text{-}STD} \right)^2 + \left(T_{out\text{-}DAQ} \right)^2 \right]^{1/2} \\ w_{T_{in}} &= \left[\left(T_{in\text{-}UNC} \right)^2 + \left(T_{in\text{-}STD} \right)^2 + \left(T_{in\text{-}DAQ} \right)^2 \right]^{1/2} \end{aligned} \tag{4.13}$$

Similarly, the uncertainty in the subcooling is:

$$w_{\Delta T_{subcooling}} = \left\{ \begin{array}{l} \left[\frac{\partial \left(\Delta T_{subcooling} \right)}{\partial T_{v}} \cdot w_{T_{v}} \right]^2 + \left[\frac{\partial \left(\Delta T_{subcooling} \right)}{\partial T_{in}} \cdot w_{T_{in}} \right]^2 \cdots \\ + \left[\frac{\partial \left(\Delta T_{subcooling} \right)}{\partial T_{out}} \cdot w_{T_{out}} \right]^2 + \left[\frac{\partial \left(\Delta T_{subcooling} \right)}{\partial q''} \cdot w_{q''} \right]^2 \end{array} \right\}^{1/2} \tag{4.14}$$

where,

$$\frac{\partial\left(\Delta T_{\text{subcooling}}\right)}{\partial T_{\text{v}}}=1$$
$$\frac{\partial\left(\Delta T_{\text{subcooling}}\right)}{\partial T_{\text{in}}}=-\frac{1}{2}$$
$$\frac{\partial\left(\Delta T_{\text{subcooling}}\right)}{\partial T_{\text{out}}}=-\frac{1}{2} \tag{4.15}$$
$$\frac{\partial\left(\Delta T_{\text{subcooling}}\right)}{\partial q''}=-\frac{A_{\text{o}}\ln(\frac{d_{\text{OD}}}{d_{\text{ID}}})}{2\pi Lk}$$

The uncertainty in the coolant mass flow rate is:

$$w_{\dot{\text{m}}_{\text{coolant}}}=\left\{\left[\frac{\partial\left(\dot{m}_{\text{coolant}}\right)}{\partial V}\cdot w_{\text{V}}\right]^2\right\}^{1/2} \tag{4.16}$$

where, $\dot{m}_{\text{coolant}}=\rho_{\text{coolant}}\cdot V$, and

$$\frac{\partial\left(\dot{m}_{\text{coolant}}\right)}{\partial V}=\rho_{\text{coolant}} \tag{4.17}$$

The uncertainty in the condensation heat flux is calculated as:

$$w_{\text{q''}}=\left\{\left[\frac{\partial\left(q''\right)}{\partial\dot{m}_{\text{coolant}}}\cdot w_{\dot{\text{m}}_{\text{coolant}}}\right]^2+\left[\frac{\partial\left(q''\right)}{\partial T_{\text{out}}}\cdot w_{\text{T}_{\text{out}}}\right]^2+\left[\frac{\partial\left(q''\right)}{\partial T_{\text{in}}}\cdot w_{\text{T}_{\text{in}}}\right]^2\right\}^{1/2} \tag{4.18}$$

where,

$$\frac{\partial\left(q''\right)}{\partial\dot{m}_{\text{coolant}}}=\frac{c_{\text{p}}}{A_{\text{o}}}\cdot\left(T_{\text{out}}-T_{\text{in}}\right)$$
$$\frac{\partial\left(q''\right)}{\partial T_{\text{out}}}=\frac{\dot{m}_{\text{coolant}}\cdot c_{\text{p}}}{A_{\text{o}}} \tag{4.19}$$
$$\frac{\partial\left(q''\right)}{\partial T_{\text{in}}}=-\frac{\dot{m}_{\text{coolant}}\cdot c_{\text{p}}}{A_{\text{o}}}$$

Finally, the uncertainty in condensation heat transfer coefficient is given by:

$$w_{h_c} = \left\{ \left[\frac{\partial(h_c)}{\partial \bar{U}} \cdot w_{\bar{U}} \right]^2 + \left[\frac{\partial(h_c)}{\partial h_{conv}} \cdot w_{h_{conv}} \right]^2 + \left[\frac{\partial(h_c)}{\partial K_{conduction}} \cdot w_{K_{conduction}} \right]^2 \right\}^{1/2} \tag{4.20}$$

where,

$$\frac{\partial(h_c)}{\partial \bar{U}} = \left[\frac{1}{\bar{U}^2} \right] \cdot \left[\frac{1}{\left(\frac{1}{\bar{U}} - \frac{A_o}{A_i \cdot h_{conv}} \right)^2} \right]$$

$$\frac{\partial(h_c)}{\partial h_{conv}} = -\left[\frac{A_o}{A_i \cdot (h_{conv})^2} \right] \cdot \left[\frac{1}{\left(\frac{1}{\bar{U}} - \frac{A_o}{A_i \cdot h_{conv}} \right)^2} \right] \tag{4.21}$$

We assumed that there is no variation in $K_{conduction}$ (the conduction thermal resistance) during the experiment. Additionally, the uncertainty in the convection heat transfer coefficient $w_{h_{conv}}$ is assumed to be 5% of the correlation value. The other parameters related to the overall heat transfer coefficient ($\bar{U}$) uncertainty $w_{\bar{U}}$ are given as follows:

$$\bar{U} = \frac{\rho_{\text{coolant}} \cdot V \cdot c_{\text{p}}}{A_{\text{o}}} \left(T_{\text{out}} - T_{\text{in}}\right) \cdot \frac{1}{\dfrac{\left(T_{\text{v}} - T_{\text{in}}\right) - \left(T_{\text{v}} - T_{\text{out}}\right)}{\ln\left[\dfrac{\left(T_{\text{v}} - T_{\text{in}}\right)}{\left(T_{\text{v}} - T_{\text{out}}\right)}\right]}} = \frac{\rho_{\text{coolant}} \cdot V \cdot c_{\text{p}}}{A_{\text{o}}} \cdot \ln\left[\frac{\left(T_{\text{v}} - T_{\text{in}}\right)}{\left(T_{\text{v}} - T_{\text{out}}\right)}\right]$$

$$w_{\bar{\text{U}}} = \left\{ \left[\frac{\partial\left(\bar{U}\right)}{\partial V} \cdot w_{\text{V}}\right]^2 + \left[\frac{\partial\left(\bar{U}\right)}{\partial T_{\text{out}}} \cdot w_{\text{T}_{\text{out}}}\right]^2 + \left[\frac{\partial\left(\bar{U}\right)}{\partial T_{\text{in}}} \cdot w_{\text{T}_{\text{in}}}\right]^2 + \left[\frac{\partial\left(\bar{U}\right)}{\partial T_{\text{v}}} \cdot w_{\text{T}_{\text{v}}}\right]^2 \right\}^{1/2}$$

$$\frac{\partial\left(\bar{U}\right)}{\partial V} = \frac{\rho_{\text{coolant}} \cdot c_{\text{p}}}{A_{\text{o}}} \cdot \ln\left[\frac{\left(T_{\text{v}} - T_{\text{in}}\right)}{\left(T_{\text{v}} - T_{\text{out}}\right)}\right]$$

$$\frac{\partial\left(\bar{U}\right)}{\partial T_{\text{out}}} = \frac{\rho_{\text{coolant}} \cdot V \cdot c_{\text{p}}}{A_{\text{o}}} \cdot \left[\frac{1}{\left(T_{\text{v}} - T_{\text{out}}\right)}\right]$$

$$\frac{\partial\left(\bar{U}\right)}{\partial T_{\text{in}}} = -\frac{\rho_{\text{coolant}} \cdot V \cdot c_{\text{p}}}{A_{\text{o}}} \cdot \left[\frac{1}{\left(T_{\text{v}} - T_{\text{in}}\right)}\right]$$

$$\frac{\partial\left(\bar{U}\right)}{\partial T_{\text{v}}} = -\frac{\rho_{\text{coolant}} \cdot V \cdot c_{\text{p}}}{A_{\text{o}}} \cdot \left[\frac{1}{\left(T_{\text{v}} - T_{\text{in}}\right)} - \frac{1}{\left(T_{\text{v}} - T_{\text{out}}\right)}\right]$$

(4.22)

4.2.8 Sample Preparation - Polishing, Cleaning, Oxidation and Plasma Modification

Copper Polishing: A ≈0.81 mm thick mirror-like finish 110 copper sheet (purity ≈ 99.9% (99.9% of copper, 0.04% of oxygen, 0.005% of lead and 0.005% of bismuth), McMaster-Carr) was sheared into small square pieces (17 mm by 17 mm) and embedded in epoxy resin (EpoThin™ 2, Buehler) to facilitate uniform polishing across the surface. The samples were first polished in series by 400 grit, 1200 grit, 2500 grit and 4000 grit sandpapers. Then a mechanical polisher (LaboPol-5, Struers) was used to polish the samples with 1 μm and 0.5 μm polycrystalline diamond particle slurries (MetaDi Supreme, Buehler) on a synthetic fabric polishing cloth (MD-Floc, Struers), and finally buffed with

a new/clean polishing cloth without any polishing liquid to remove excess particles on the surface. A root mean square (RMS) roughness (*Rq*) less than 3 nm was achieved using this procedure on copper sheets.

Similarly, copper tubes (copper 122, purity ≈99.9% (99.9% of copper and 0.02% of phosphorus), McMaster-Carr) were first polished with 1200 grit sandpaper followed by 2400 grit and 4000 grit sandpaper, and subsequently with a 0.5 μm polycrystalline diamond particle slurry (MetaDi Supreme, Buehler) and a microfiber cloth (McMaster-Carr). To avoid physical damage to the polished surfaces during sample transport and the condensation heat transfer setup assembly, Swagelok® compression tube fittings were incorporated on the copper tubes before polishing, and these fittings were capped for the polishing, coating synthesis and the plasma treatment steps. A root mean square (RMS) roughness (*Rq*) less than 8 nm was achieved using this procedure on copper tubes.

Sample cleaning: The polished copper samples were cleaned in a methanol sonication bath (P1100D, Crest Ultrasonics), rinsed with deionized (DI) water, and dried with 99.99% pure nitrogen to remove the particles from polishing and minimize the potential for ambient atmosphere contamination of the surfaces.

Silicon wafers used for coating depositions were first diced into small pieces (17 mm × 17 mm) by either a diamond pen scribe or an automated dicing saw. A custom PTFE holder containing the diced wafers was then immersed in piranha solution (sulfuric acid, 95-98% and hydrogen peroxide, 30 wt.% in water, ratio 3:1) for 20 minutes to remove any organic contamination. The dipper (*i.e.*, the PTFE holder) was gently shaken

during this process to avoid wafers overlapping and to ensure that both sides are completely wetted by the piranha solution. Then the dipper with wafers was immersed in six consecutive pure DI water baths to remove excess piranha solution. After drying with pure nitrogen gas, clean wafers were stored in a piranha-cleaned glass petri dish. The importance of piranha cleaning for silicon surfaces is discussed in Section 4.3.1.

Utensils cleaning: All utensils used were first cleaned with acetone, methanol, isopropanol and deionized (DI) water, and dried with pure nitrogen. Glassware, including crystalizing dishes for the coating solution, the petri dishes used to transfer/store samples and glass thermometers, were then cleaned with piranha solution and rinsed multiple times with pure DI water. After drying in a forced convection oven at 70°C for at least 2 hours, the glassware were further cleaned by an argon (Ar) plasma at 75 W for 30 minutes (EM-KLEEN, PIE Scientific LLC).

Chemically oxidation: Chemically oxidized copper samples were prepared by first cleaning with methanol and DI water, followed by immersion in 30 wt.% hydrogen peroxide solution for 20 minutes, and finally rinsing with DI water and drying with pure nitrogen. The container for hydrogen peroxide solution was shaken gently during chemical oxidation to aid with bubble detachment from the sample surfaces (pinned bubbles lead to non-uniform surface oxidation).

Plasma modification: The copper samples were modified by oxygen (O_2) plasma in a large chamber tabletop plasma cleaner (Tergeo, PIE Scientific LLC). The chamber was first pumped down to ≈66.7 Pa, flushed with pure oxygen gas, and then pumped down again to ≈6.7 Pa. The oxygen flushing step removed any excess air in the system and

guaranteed a pure oxygen environment before plasma activation. Oxygen plasma was activated in the chamber with a constant oxygen flow rate (≈5.0 sccm, operating chamber pressure ≈20.0 Pa) at 75 W of input RF power for 10 minutes. The determination of this optimal plasma treatment time is discussed in Section 4.4.1.

4.3 Robust Coating on Silicon Substrates

4.3.1 The Role of Piranha Cleaning

Previous studies[200, 201] have shown using BET method from low temperature adsorption of krypton that piranha cleaning hydroxylates the silicon surface and creates a saturated density of hydroxyl (-OH) groups on the silicon surface (*i.e.*, silanol groups, or Si-OH), facilitating the bonding of silane molecules to the substrate *via* Si-O-Si bonds. Some other work claimed that air plasma[202] and oxygen plasma[203, 204] can also hydroxylate silicon substrates by demonstrating the low static water contact angles on plasma treated silicon wafers. We have measured the advancing and receding water contact angles on TFTS coatings deposited on single side polished (SSP) silicon wafers cleaned by piranha solution and air plasma (Figure 37). Both coatings were deposited at the same time in an anhydrous condition, and the contact angles were calculated by averaging the measurements from 3 different spots on the samples. Plasma bombardment is expected to remove airborne contaminants and adsorbed hydrocarbons,[148, 202, 205] thus a lower RMS roughness was achieved on the air plasma treated sample. However, the sample cleaned by piranha solution exhibited a lower contact angle hysteresis (≈14.2°), denoting that a better coating quality than the coating deposited on the air plasma treated sample. Note,

the SSP wafers have larger roughness compared to double side polished (DSP) wafers used in Section 4.2.

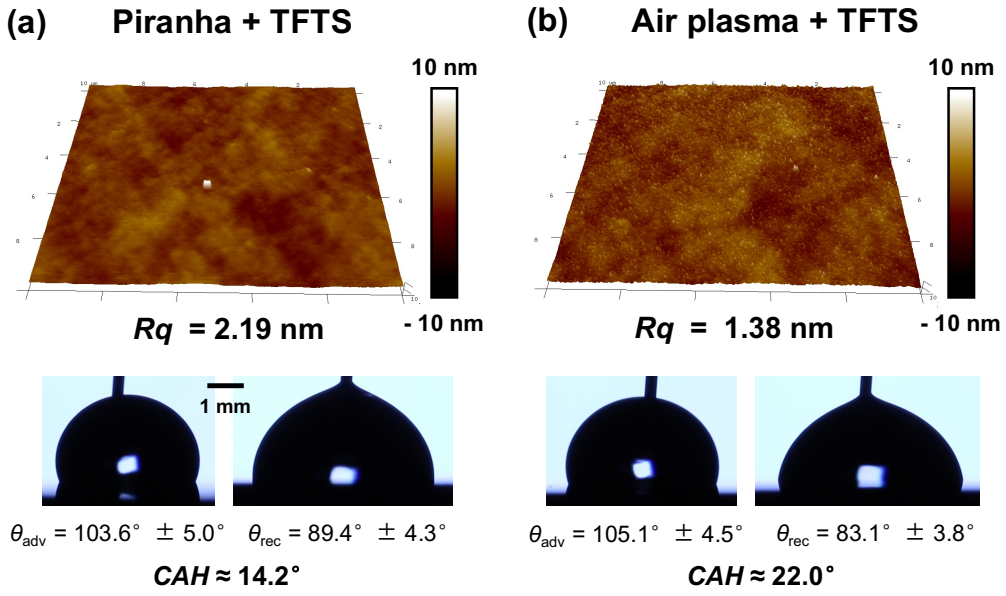

Figure 37. AFM topography scans (10 µm by 10 µm) and representative images of advancing and receding droplets on (a) a piranha cleaned silicon wafer coated by TFTS, and (b) a silicon wafer cleaned by air plasma and coated by TFTS.

4.3.2 Coating Repeatability

We tested the repeatability of our coating procedures by performing coating experiments on different days with different batches of chemicals (*i.e.*, hexane and organofunctional silane) on separate double-side polished (DSP) silicon wafer substrates. Four different types of organofunctional silanes (trichloro(octadecyl)silane or OTCS, trichloro(1H,1H,2H,2H-perfluorooctyl)silane or TFTS, chloro(dodecyl)dimethylsilanes, or MNCS, and 1H,1H,2H,2H-perfluorododecyl trichlorosilane, or OTDS) were integrated in the controlled/anhydrous environment in at least 4 trials. The measurements of

advancing and receding contact angles for these four different silanes are plotted in Figure 38 using both the "averaging all data" and the "peaks and troughs" methods reported in Chapter 4.2.1 (red and blue, respectively). For both methods, the data from different coating batches all lie within the uncertainty bars. These consistent contact angle results for various batches of coated samples and for four different types of organofunctional silanes confirm that our coating procedure is reproducible. In addition to the contact angle measurements, the reproducibility of the coating procedure was also validated *via* the RMS roughness obtained using atomic force microscopy (AFM). The average RMS roughness and standard deviation (1σ) are 0.203 ± 0.054 nm, 0.219 ± 0.039 nm, 0.200 ± 0.044 nm and 0.178 ± 0.037 nm for a 2 μm × 2 μm region for OTCS, TFTS, TFDS and MNCS coatings respectively, prepared under the moisture/water-free conditions in four different trials. The consistently low roughness level and the small standard deviation for all coatings further validate that the coating procedure is reproducible.

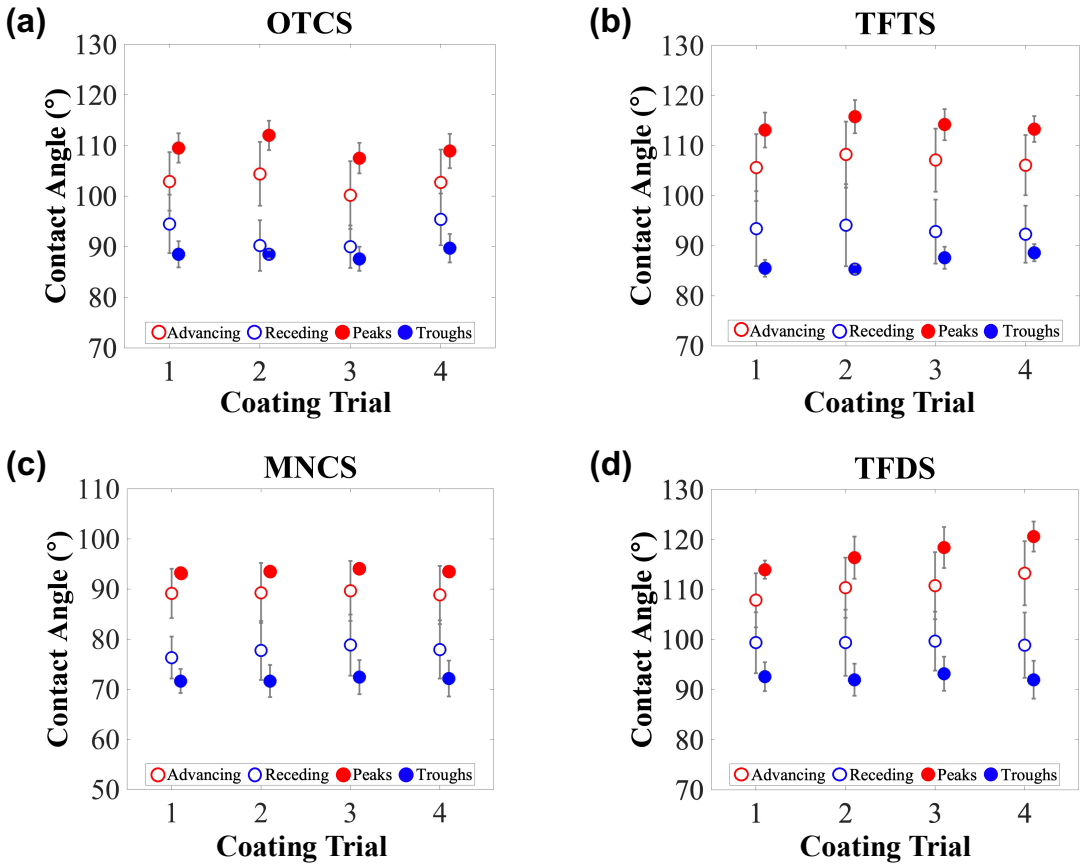

Figure 38. Advancing and receding contact angles calculated by averaging all 120 frames (hollow points) and only peak and trough values from the profile (solid points) for (a) OTCS, (b) TFTS, (c) MNCS, and (d) TFDS.

In addition to the repeatability test with four different silanes in the controlled environment, we present additional data here to compare the reproducibility of the coatings integrated in the controlled condition and the ambient condition. Representative scans at various locations on the samples from different coating trials for TFTS controlled, TFTS ambient-A, OTCS controlled and OTCS ambient-A are presented in Figure 39. Besides the difference on average RMS roughness resulted from the different synthesis environment shown earlier in Section 4.1.4, the controlled coating environment contributes to a higher coating conformality as compared to the ambient environment

which ultimately affects the coating quality in the roughness and the wetting behavior. The non-uniform surface topographies for the ambient-A coatings result from an uncontrolled water concentration which leads to randomly cross-linked silane agglomerates.

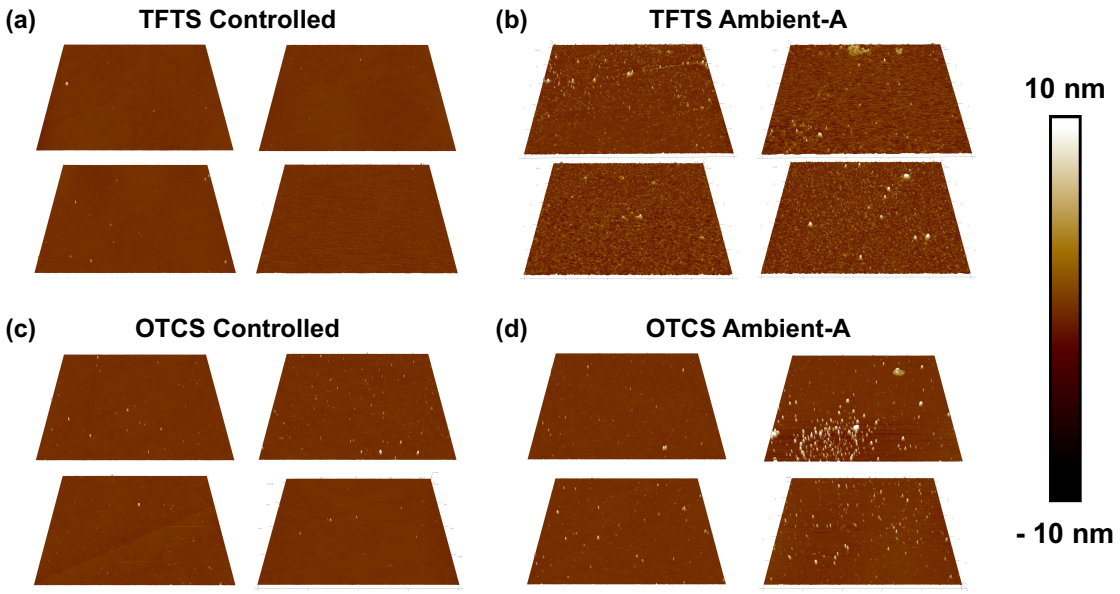

Figure 39. Representative AFM scans for (a) TFTS controlled, (b) TFTS ambient-A, (c) OTCS controlled and (d) OTCS ambient-A samples coated in different trials. The scanning area is 10 µm × 10 µm.

4.3.3 Durability Test during Water Vapor Condensation (Silicon Surfaces)

To test our hypothesis on the SAM coating degradation under active water vapor condensation reported in Section 4.1.1, we performed condensation heat transfer experiments for silicon test samples coated with two different silane coatings: TFTS and OTCS. These coatings were integrated on silicon substrates in both controlled and ambient (with anhydrous hexane solvent) conditions (*i.e.*, controlled and ambient-A samples). Condensation experiments were performed in a pure and saturated water vapor

environment, with the vapor temperature around ≈54-55 °C. The TFTS-(controlled and ambient-A) and OTCS-(controlled and ambient-A) coated samples were tested on separate runs, each lasting ≈460 hours (Figure 40), and hence the operating conditions were a little different across the two runs. Although all the experimental settings and steps were kept the same for both runs, the subcooling (*i.e.*, the temperature difference between the vapor and the substrate) was marginally different: ≈11 °C ($T_{substrate}$ ≈44 °C and T_{vapor} ≈55 °C) for TFTS, and ≈8 °C ($T_{substrate}$ ≈ 46 °C, T_{vapor} ≈54 °C) for OTCS. For each test run, we tested three specimens each of the controlled and ambient A samples. Each run also contained one uncoated silicon sample to ensure that the observed dropwise condensation behavior was not due to any contamination within the vapor environment. We stopped the tests prior to complete failure of the coating (*i.e.*, we only tested up to ≈460 hours) to facilitate meaningful surface characterization (*e.g.*, coating thickness, surface roughness, chemical composition) post water vapor condensation. If we perform the tests until complete failure of the coatings, only a binary pass/fail result would be possible since total failure results in complete removal of the coating. Additionally, in order to prevent this binary pass/fail result, we also tested the ambient-A samples as opposed to the ambient-NA samples which we expect to fail quickly.

For coatings synthesized in a controlled environment (*i.e.*, the glovebox with anhydrous hexane solvent), both TFTS- (Figure 40a) and OTCS- (Figure 40c) coated samples visibly promoted perfect dropwise condensation of water vapor for ≈460 hours without degrading and transitioning to the filmwise mode. However, TFTS ambient-A samples (Figure 40b) started to fail around ≈240 hours and the droplet departure diameter

increased noticeably over time. Here, we define failure as regions of the substrate transitioning to exhibit filmwise condensation (FWC), or the presence of large pinned droplets. By ≈460 hours when the experiment was terminated, the TFTS-coated ambient-A samples almost predominantly (>75% of surface, Figure 40b) exhibited FWC. For the OTCS-coated ambient-A samples (Figure 40d), partial failure was observed from around ≈145 hours, however, the failure region did not propagate (*i.e.*, increase in size) significantly more up to the termination of the experiment at ≈460 hours.

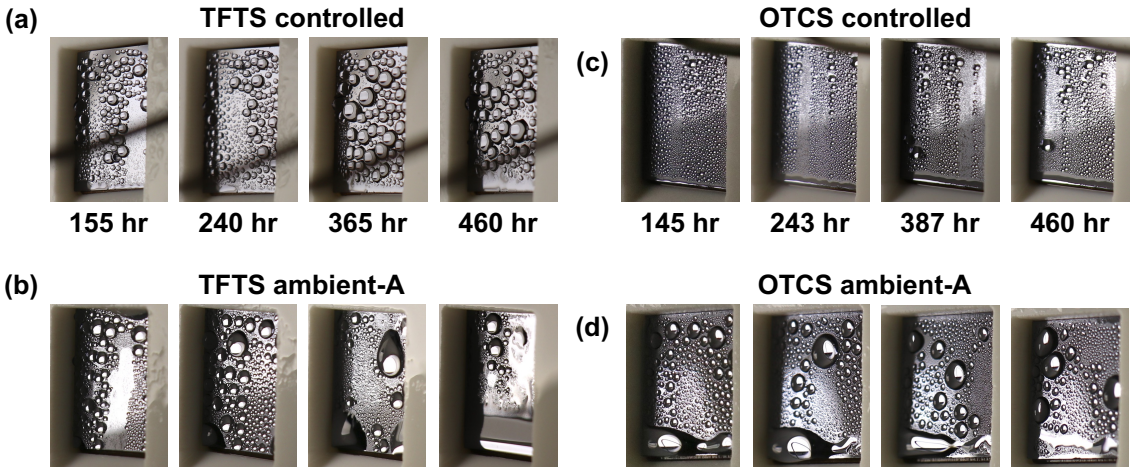

Figure 40. Time-lapse images of continuous condensation of water vapor on (a) TFTS controlled, (b) TFTS ambient A, (c) OTCS controlled and (d) OTCS ambient A samples. The sample size is 17 mm by 17 mm. Reprinted from Wang *et al.*, *ACS Appl. Mater. Interfaces.*, 2021.

In order to demonstrate the reproducibility of the coating robustness during water vapor condensation, we included multiple test samples each of OTCS controlled, OTCS ambient-A, TFTS controlled and TFTS ambient-A (3 each) in the condensation heat transfer experiments. Overall, of the 3 samples tested for each coating-environment combination, the controlled environment coated samples (both TFTS and OTCS) exhibited higher durability after condensing water vapor for ≈460 hours. Specifically, two

of three TFTS controlled samples (Figure 41a) exhibited ≈30% coating failure (*i.e.*, FWC on ≈30% of the surface, which is estimated based on surface area) and ≈15% coating failure. For the TFTS ambient-A samples (Figure 41b), one of three exhibited complete dropwise condensation or DWC, while the other two had ≈70% failure and ≈50% failure. This inconsistency in coating failure observed for the ambient-A samples is expected since cross-linking and preferential wetting in any uncontrolled coating condition may lead to random molecule alignment and hence variability in coating quality. All three OTCS controlled samples (Figure 41c) maintained perfect dropwise condensation throughout the experiment, and two out of the three OTCS ambient-A samples (Figure 41d) exhibited filmwise condensation partially (*i.e.*, at the bottom edge, ≈20% in area), denoting an early stage of coating degradation. These coating durability tests provide further validation of our hypothesis: alkyl/fluoro-silane SAM coatings synthesized in a controlled water/moisture-free environment have superior robustness during water vapor condensation as compared to those synthesized in the uncontrolled environment, and such higher robustness is reproducible as long as the stringent coating procedure is followed.

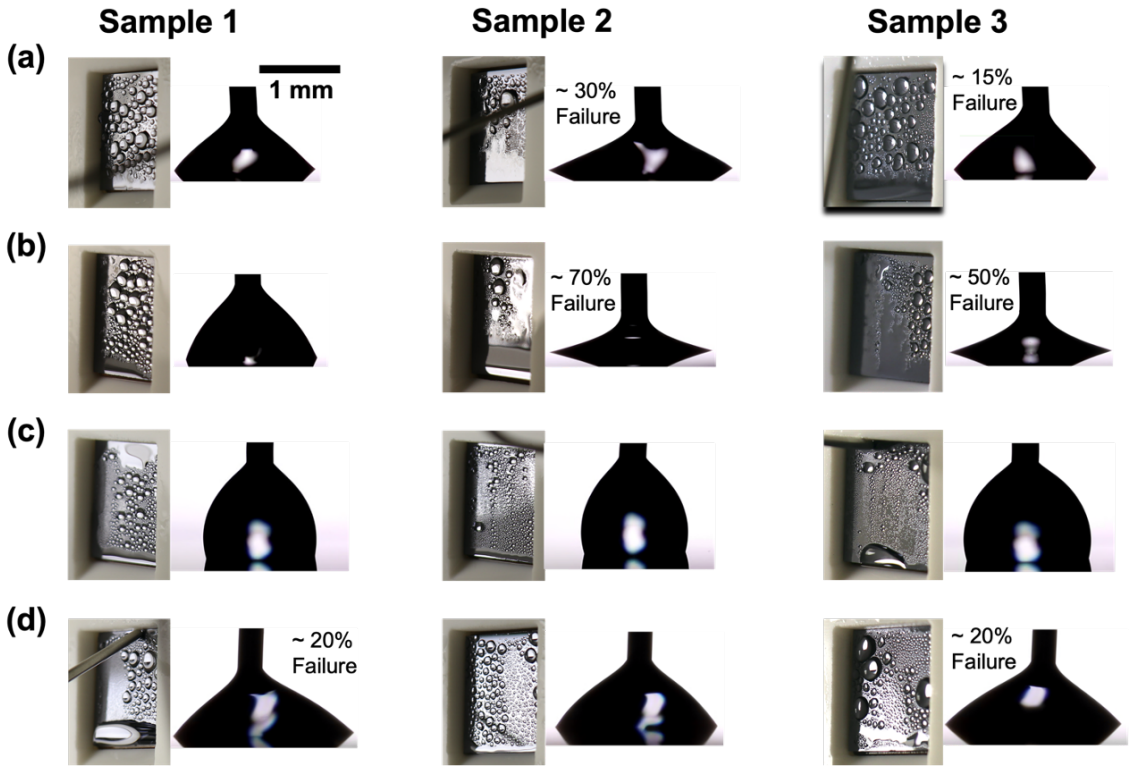

Figure 41. Optical images of water vapor condensation at ≈460 hours and the corresponding receding contact angles for (a) TFTS controlled, (b) TFTS ambient-A, (c) OTCS controlled, and (d) OTCS ambient-A samples.

The heat flux into the test samples during condensation is estimated by calculating the sensible heat gained by the coolant flowing through the cold plate:

$$q'' = c_p \dot{V} \rho (T_{inlet} - T_{outlet}) \tag{4.23}$$

where, q'' is the heat flux, c_p is the heat capacity, $\dot{V}$ is the flow rate, ρ is the liquid density, and T_{outlet} and T_{inlet} are the coolant outlet and inlet temperature measured by thermocouples. The estimated heat flux for TFTS and OTCS are ≈23.8 kW/m^2 and ≈42.9 kW/m^2, respectively. This is estimated from the heat transfer rate and the number of test samples on the cold plate. The heat transfer coefficient (HTC) is estimated by:

$$h = \frac{q''}{\Delta T} \tag{4.24}$$

where, ΔT is the subcooling (*i.e.*, the temperature difference between the substrate and the vapor). The corresponding heat transfer coefficients are ≈2.16 kW/m^2·K and ≈5.36 kW/m^2·K for TFTS and OTCS, respectively. This estimate of the HTC does not account for any thermal contact resistances in the substrate temperature measurements, and hence is lower than expected for traditional dropwise condensation.

These above estimates are based on all the test samples mounted on the cold plate, however, each experiment included 8 test samples. For the TFTS condensation experiment run, there were 6 silane coated test samples and 2 uncoated test samples (*i.e.*, plain silicon wafers with no coating), while for the OTCS condensation experiment run, there were 7 silane coated test samples and 1 uncoated test sample. A consequence of this cold plate-insulation design is that the individual sample heat transfer rate cannot be estimated or decoupled from that of other test samples connected to the heat sink. Since the above calculation treats all 8 test samples the same, we correct for the variation in DWC and FWC to obtain a corrected heat flux and HTC for the coated samples promoting dropwise condensation. This new estimate assumes that the HTC for DWC is 8× that of FWC. The corrected heat flux for TFTS and OTCS are ≈30.4 kW/m^2 and ≈48.1 kW/m^2, and the HTC are ≈2.76 kW/m^2·K and 6.02 kW/m^2·K, respectively. The trends for both the original and corrected estimates for heat flux and HTC are consistent with the droplet departure sizes; TFTS coated samples with larger droplet departure diameters exhibiting lower heat flux and HTC as compared to the OTCS coated samples with smaller droplet departure diameters. It is important to note that these estimates are averaged over multiple

test samples, and hence are an average heat transfer performance for coatings that did fail and those that did not.

We also monitored and quantified the departure diameters of droplets on each surface over time, and the results are presented in Figure 42a. The droplet departure diameter on the OTCS controlled sample maintained fairly constant during the 460 hours of continuous condensation of water vapor, and the rest three samples showed an increase in departure diameter over time. This further validates the better coating quality and robustness of the OTCS coating deposited in the controlled environment.

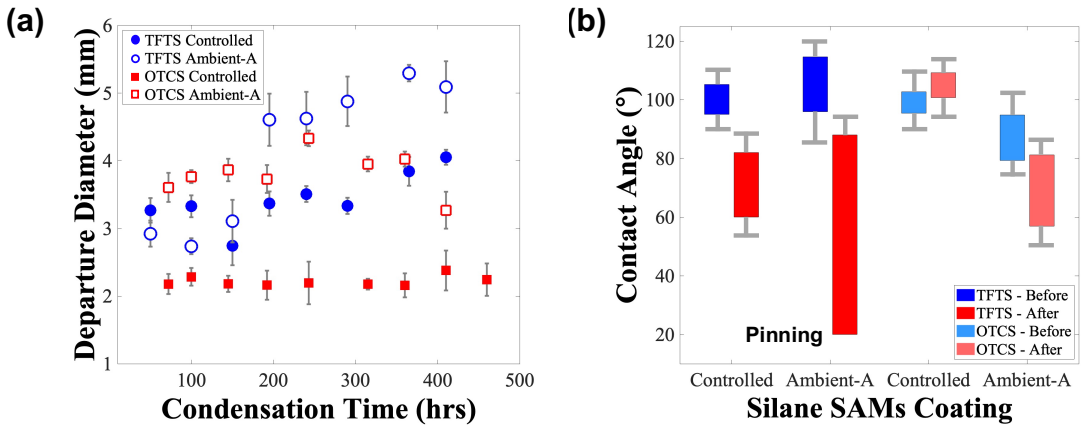

Figure 42. (a) Droplet departure diameters for the condensate droplets on the four samples as a function of condensation time. (b) The advancing and receding contact angles before and after condensation for ≈460 hours. Reprinted from Wang *et al.*, *ACS Appl. Mater. Interfaces.*, 2021.

4.3.4 Pre- and Post-Condensation Surface Characterization

We performed surface characterization for all samples after the ≈460 hours of water vapor condensation testing. In Figure 42b we compare the changes in contact angles of water for all four groups of samples tested (data summarized in Table 6). The upper

and lower bounds of the boxes in the plot represent the advancing and receding contact angles, respectively. Coatings synthesized in the controlled environment exhibit smaller changes in contact angles and lower contact angle hysteresis than those prepared in uncontrolled ambient conditions. These quantitative contact angle measurements confirm what was qualitatively apparent from the images/videos of the surfaces during active water vapor condensation.

From a nanoscale perspective, Figure 43 shows atomic force microscopy (AFM) scans of the TFTS- and OTCS-coated samples after condensation testing (≈460 hours). The controlled samples exhibited the same level of RMS roughness as before condensation experiments (Figures 43a and 43c). Interestingly, the RMS roughness of the OTCS ambient-A sample did not increase noticeably, which is consistent with the fact that it only underwent a partial transition to FWC at the bottom edge (Figure 43d). For the TFTS ambient-A sample, numerous agglomerates were observed which raised the RMS roughness by almost an order of magnitude (*i.e.*, ≈1.17 nm *v/s* ≈10.69 nm). We suggest that these agglomerates are delaminated silane molecules (due to the dissolution of the Si-O bond in water[206]) which remain cross-linked to other surface bonded silane molecules. We propose this explanation since this TFTS-coated ambient-A sample exhibited FWC over large areas and had a receding contact angle lower than 20°, however the advancing angle was ≈88.7°±5.5°. Pinning of the receding (or leaving) droplets likely originates from such agglomerate defects or the exposed substrate.[207]

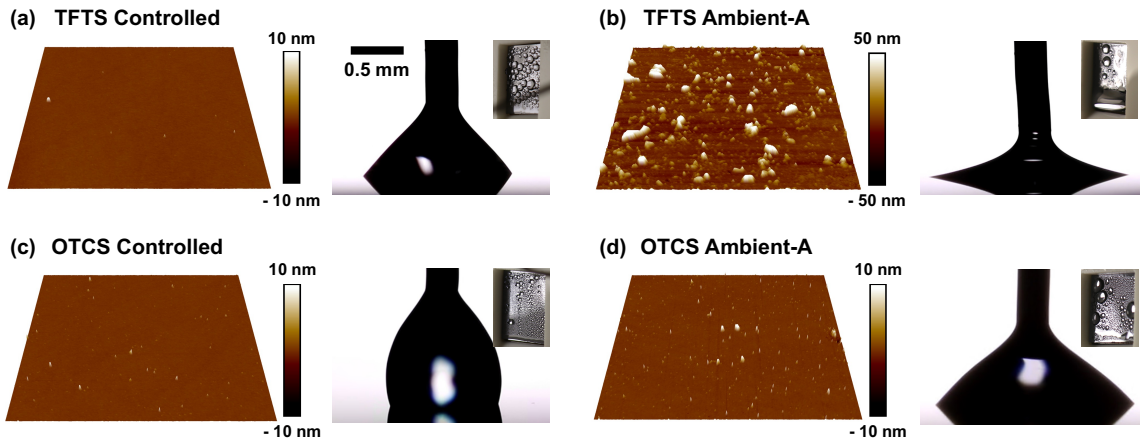

Figure 43. AFM topography scans (10 µm by 10 µm) and corresponding images of receding water droplets on (a) TFTS controlled, (b) TFTS ambient-A, (c) OTCS controlled, and (d) OTCS ambient-A after ≈460 hours of water vapor condensation. Reprinted from Wang *et al.*, *ACS Appl. Mater. Interfaces.*, 2021.

Table 6 lists all surface characterization results, including AFM, ellipsometry, contact angle measurement, and x-ray photoelectron spectroscopy (XPS), of all samples tested in the condensation experiments. The TFTS ambient-A sample has a receding contact angle lower than 20° (pinning of the droplet), and hence the standard deviation is not available. For the uncoated silicon wafer, water instantly wets the silicon surface as a thin water film, and hence contact angles cannot be measured. After water vapor condensation, the significant increases in CAH for the ambient-A samples indicated an attenuated hydrophobicity either through a loss of coating and/or a decrease in coating quality. The former factor (*i.e.*, loss of coating bonded to the substrate) likely occurred on the TFTS-coated ambient-A samples, and the latter factor (*i.e.*, decrease in coating quality) likely occurred on the OTCS-coated ambient-A samples since water vapor was condensing on these latter surfaces in the DWC mode, but with larger droplet departure

diameters. Both these observations confirmed that the silane coatings degraded during water vapor condensation on the surfaces coated in an uncontrolled ambient environment.

Table 6. Surface characterization results for all coatings (TFTS controlled, TFTS ambient-A, OTCS controlled and OTCS ambient-A) tested, pre (≈0 hours) and post (≈460 hours) water vapor condensation experiments.

	Coating	TFTS Controlled		TFTS Ambient-A		OTCS Controlled		OTCS Ambient-A		Uncoated Silicon	
	Measurement	Pre	Post	Pre	Post	Pre	Post	Pre	Post	Pre	Post
AFM	10 µm Rq (nm)	0.319	0.285	1.170	10.69	0.416	0.401	0.811	0.612	< 0.3	0.104
	2 µm Rq (nm)	0.196	0.128	0.989	3.91	0.258	0.164	0.263	0.237	< 0.2	0.078
Ellipsometry	Thickness (nm)	0.6	1.0	1.4	0.6	1.5	3.2	1.6	2.1	4.2	5.1
	Std. Dev. (nm)	0.1	0.0	0.1	0.2	0.0	0.1	0.2	0.1	0.1	0.1
Contact Angle	Advancing (°)	105.2	82.5	114.6	88.7	102.7	109.2	94.8	81.2	N/A	N/A
	Std. Dev. (°)	5.0	5.8	7.1	5.5	6.5	4.8	7.3	5.2	N/A	N/A
	Receding (°)	95.0	60.1	95.9	< 20	95.4	100.7	79.3	56.9	N/A	N/A
	Std. Dev. (°)	5.0	5.8	10.5	N/A	5.1	5.7	4.4	5.8	N/A	N/A
	Hysteresis (°)	10.2	22	18.7	> 68	7.3	8.5	15.5	24.3	N/A	N/A
XPS	C Atomic %	17	19	20	35	24	24	40	53	16	37
	O Atomic %	21	24	16	29	26	25	20	16	30	22
	Si Atomic %	41	46	29	31	50	51	40	31	54	41
	F Atomic %	21	11	35	5	0	0	0	0	0	0

After condensation of water vapor, the TFTS-coated controlled samples have a relatively small increase in CAH and a small decrease in fluorine content compared to the ambient-A samples. These estimations and comparisons of the TFTS coating fluorine content were obtained from XPS measurements of the test samples pre- and post-

condensation (Figure 44). Specifically for the TFTS-coated ambient-A sample, the CF_2 and CF_3 peaks disappear and the F peak amplitude reduces substantially (*i.e.*, atomic ratio reduced from 35% to 5%) after condensation of water vapor. The TFTS-coated controlled sample has a comparatively smaller decrease in CF_2 peak and F peak amplitude (*i.e.*, atomic ratio reduced from 21% to 12%). The OTCS-coated ambient-A sample had a 13% increase in carbon atomic ratio with 4% and 9% decrease in oxygen and silicon atomic ratios, respectively. Conversely, for the OTCS-coated controlled samples which showed negligible increases in CAH (≈1°), the constituent chemical component ratios obtained from XPS changed negligibly (≈1%), confirming their excellent robustness to water vapor condensation.

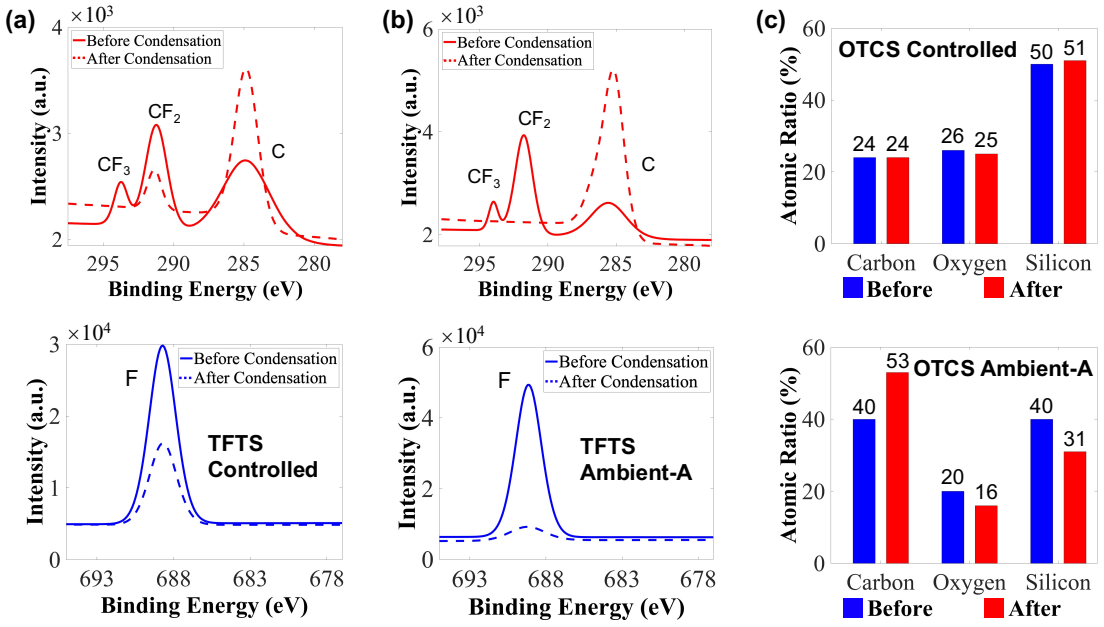

Figure 44. X-ray photoelectron spectroscopy (XPS) carbon and fluorine peaks for (a) TFTS controlled sample, and (b) TFTS ambient-A sample. (c) Atomic ratios before and after 460 hours of condensation obtained by XPS. Reprinted from Wang *et al.*, *ACS Appl. Mater. Interfaces.*, 2021.

4.3.5 SAM Degradation Mechanism on Silicon

Previously in Sections 4.1.2 and 4.1.4, we proved that the silane SAM coatings deposited in the controlled condition exhibit higher coating conformality (*i.e.*, lower contact angle hysteresis and minimal RMS roughness). In Sections 4.3.3 and 4.3.4, we demonstrated that the controlled coatings are more robust during water vapor condensation, while the uncontrolled/ambient coatings typically fail and propagate on silicon substrates, and this failure was manifested as a transition to filmwise condensation from the more efficient dropwise condensation that was observed on all surfaces at the start of the condensation heat transfer tests. This result further validated our hypothesis proposed in Section 4.1.1 that the organofunctional silane SAM coatings degrade during water vapor condensation because of the expansion of defects within the SAM coating on the silicon/silicon dioxide substrate. These degradation nucleation site defects are likely uncoated substrate regions that dissolve in the presence of pure water that is actively and continuously transported to the substrate surface during condensation.

4.4 Robust Coating on Copper Substrates

4.4.1 The Role of Oxygen Plasma Modification

It is well known that surface hydroxide is favorable for uniform formation of silane and thiol self-assembled monolayer coatings, since the molecules bond to hydroxyl groups (-OH) on the substrate. However, we cannot use piranha solution to hydroxylate metal surfaces, because piranha solution can vigorously dissolve/react with metals. Prior research studies have introduced plasma treatment (either air or oxygen) of copper

surfaces prior to SAMs coating integration for the purposes of removing surface hydrocarbons[148, 202, 205, 208] and hydroxylating the substrate (*i.e.*, creating -OH groups)[203, 204, 208]. Nevertheless, beyond demonstrating low *static* contact angles on bare air/oxygen plasma treated substrates (*i.e.*, complete wetting indicates good -OH termination coverage), there is rarely any evidence provided for the role of the plasma in creating pristine SAM coatings, and the surface chemistry of oxygen plasma treatment on metal surfaces remains unknown.

To understand the effect of plasma treatment on the copper substrate, we first performed x-ray photoelectron spectroscopy (XPS) scans on a polished copper surface immediately (<10 minutes) after polishing, and the copper XPS profile (Figure 45a) indicates a cuprous oxide (Cu_2O) surface with a $Cu2p_{3/2}$ peak at 932.4 eV, a $Cu2p_{1/2}$ peak at 952.3 eV, and a weak satellite peak in between.[209, 210] When treated by a low pressure ($\approx 20 \pm 0.4$ Pa) pure oxygen plasma for 10 minutes, the polished surface is oxidized to cupric oxide (CuO) with a $Cu2p_{3/2}$ peak at 934.5 eV, a $Cu2p_{1/2}$ peak at 954.3 eV, and two satellite peaks. This profile (Figure 45b) and the equivalent intensities of the $Cu2p_{1/2}$ peak and its corresponding satellite peak at 962.0 eV confirm a complete CuO surface.[211] Oxidation of copper surfaces to cupric oxide also occurs gradually in ambient conditions in air (Figure 45b shows the XPS profile for an ambient air-oxidized CuO surface). The $Cu2p_{3/2}$ peak at 932.5 eV and the $Cu2p_{1/2}$ peak at 952.2 eV each with small satellite peaks to their left indicate the transition from Cu_2O to CuO (*i.e.*, shifting towards higher binding energy and closer to a CuO profile). However, this oxidation in ambient air is a partial

oxidation as evidenced by the relatively lower intensities of the two satellite peaks in Figure 45b.

Copper surfaces can also be chemically oxidized in hydrogen peroxide (H_2O_2) solution, resulting in a complete CuO profile (Figure 45c) which is equivalent to that of a surface oxidized by oxygen plasma. The key difference between a copper surface oxidized by O_2 plasma and one oxidized in H_2O_2 solution is a metal oxide peak (*i.e.*, CuO at 529.3 eV) and a metal hydroxide peak (*i.e.*, $Cu(OH)_2$ at 531.4 eV) for the former as shown in Figure 45d, and a metal oxide peak at 529.4 eV, a metal carbonate peak (*i.e.*, $CuCO_3$ at 531.1 eV) and a weak organic peak (*i.e.*, C=O bonds at 532.4 eV) for the latter as shown in Figure 45e. The observed organic C=O bonds most likely result from dissolved carbon dioxide in the hydrogen peroxide solution and any airborne contaminants. By treating the H_2O_2 oxidized copper surface with a low pressure oxygen plasma (≈10 minutes), the metal carbonate and organic C=O bonds peaks are suppressed, and the metal oxide (at 529.3 eV) and metal hydroxide (at 531.6 eV) peaks typically seen after an O_2 plasma treatment, are recovered (Figure 45f). Interestingly, the various copper surfaces treated by O_2 plasma for 10 minutes, either directly after surface polishing or with an intermediate H_2O_2 solution oxidization step, have a constant area ratio of hydroxide to oxide distributions ≈72:28%. Therefore, oxidation and hydroxylation by pure oxygen plasma is expected to result in better SAM coating quality on copper substrates. In an oxygen XPS spectrum, the metal oxides, the metal carbonates and the metal hydroxides peaks have the corresponding ranges of binding energies at 528.0 eV ~ 531.0 eV, 530.5 eV ~ 531.5 eV, and 530.9 eV ~ 532.0 eV, respectively.[209-211]

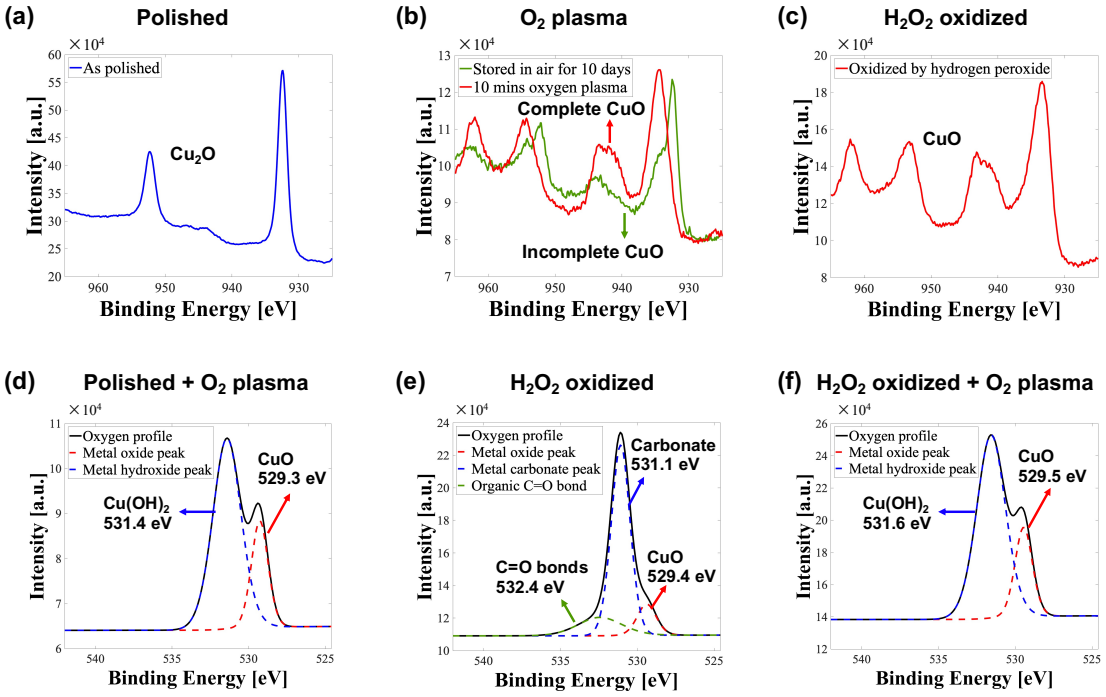

Figure 45. X-ray photoelectron spectroscopy (XPS) copper peaks (a, b, c) and oxygen peaks (d, e, f) for copper substrates treated with various polishing and oxidation methods.

In order to study the effect of oxygen plasma treatment on the SAM coating quality, we varied the oxygen plasma treatment time from 30 seconds to 2 hours (11 different time periods tested) and deposited the two most commonly used silane SAM coatings in condensation studies (*i.e.*, trichloro(1H,1H,2H,2H-perfluorooctyl)silane, or TFTS, and trichloro(octadecyl)silane, or OTCS). The coatings were integrated on copper substrates in a controlled environment immediately after the plasma modification. These copper substrates were created by depositing thin copper films (≈400 nm) on double-side polished silicon wafers *via* electron beam (e-beam) evaporation with titanium as an intermediate adhesion layer. The e-beam evaporated copper samples were used for this test due to the excellent RMS roughness level achievable (Rq <4 nm) and the convenience of the method

to produce a large quantity of samples as compared to mechanical polishing. The results for the measured water contact angles as a function of oxygen plasma treatment time are plotted in Figure 46. Here, the top and bottom of the box plots represent the advancing and receding angles, respectively, and the box height indicates the contact angle hysteresis. A treatment time from 10 minutes to 45 minutes was shown to be the optimal range in terms of achieving a low contact angle hysteresis. In this work we adopted 10 minutes of oxygen plasma treatment for all our coating procedures.

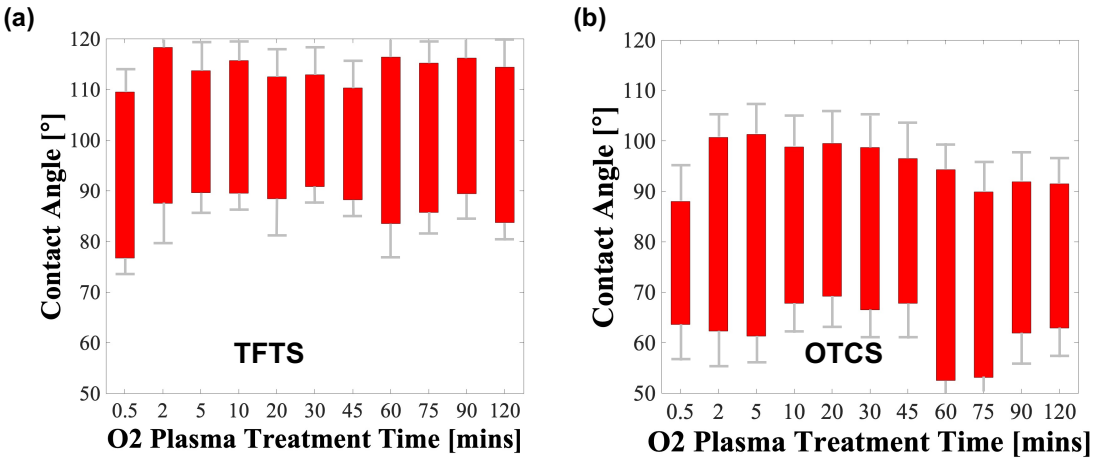

Figure 46. The effect of oxygen plasma treatment time on contact angle hysteresis for (a) TFTS and (b) OTCS. The top and bottom of the boxes represent the advancing and receding angles, respectively, and the box height indicates the contact angle hysteresis.

With an understanding of the resulting surface chemistry from a pure O_2 plasma treatment (Figure 45, *i.e.*, creating favorable bonding sites for silane molecules) and the determination of the optimal plasma treatment time (Figure 46, *i.e.*, 10 minutes plasma treatment leads to lower contact angle hysteresis), we coated trichloro(1H,1H,2H,2H-perfluorooctyl) silane (or TFTS) on (i) a polished copper surface without an intermediate O_2 plasma treatment step and (ii) a polished copper surface first treated with O_2 plasma

for 10 minutes. Silane integration on the copper substrates was primarily done in a controlled environment using procedures we have reported in prior work. A comparison of the XPS carbon profiles and contact angle measurements for these two samples are shown in Figure 47. For TFTS directly deposited on polished copper, the advancing and receding contact angles are 121.6° ± 6.2° and 64.1° ± 6.5°, respectively, and the elemental atomic ratio obtained with XPS is C:Cu:F:O ≈30:8:20:42%. Comparatively, the polished copper surface when treated with an O_2 plasma just prior to TFTS coating exhibits a much lower contact angle hysteresis (≈18.1°) with advancing and receding contact angles being 106.9° ± 5.8° and 88.8° ± 6.5°. This contact angle hysteresis is similar to that achieved for TFTS deposited on an ultra-smooth silicon surface. The corresponding XPS atomic ratio is C:Cu:F:O ≈49:3:35:13%. The higher atomic ratios for fluorine and carbon (originating from the TFTS coating), and the lower contact angle hysteresis on the oxygen plasma modified sample indicate a conformal SAM coating layer (*i.e.*, the fluorinated silane molecules are densely packed).

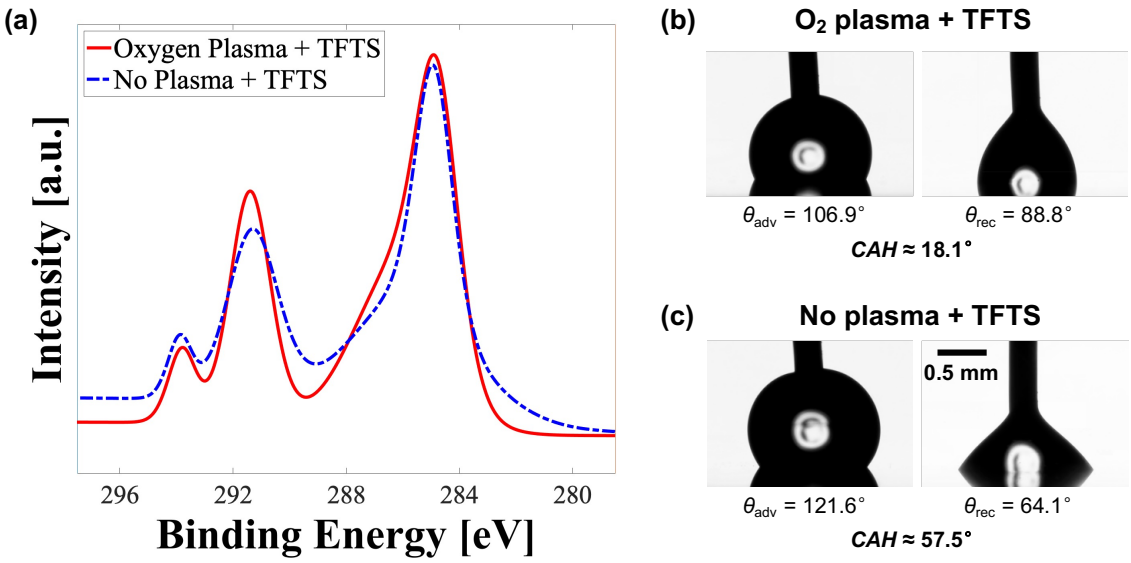

Figure 47. (a) XPS carbon spectra and (b) representative images showing advancing and receding droplets and their corresponding contact angles on the TFTS coated copper samples with and without oxygen plasma treatment.

4.4.2 Durability Test during Water Vapor Condensation

Surface roughness is known to affect silane SAM coating quality,[53, 60, 197] and this may also affect coating durability during water vapor condensation. Hence, we studied the effect of substrate roughness on coating durability during water vapor condensation. We prepared copper substrates at four different roughness levels (Figure 48): samples polished by 400 grit sandpaper and 1200 grit sandpaper, oxidized by H_2O_2 solution and mechanically polished with a 0.05 μm polishing slurry had root mean square (RMS) roughness (or *Rq*, obtained by AFM with a scan size 20 μm by 20 μm) of 420 nm, 232 nm, 23 nm and 2.70 nm, respectively. All four samples were subsequently treated with oxygen plasma for 10 minutes and then coated with TFTS in a controlled environment. Oxygen plasma treatment did not affect the roughness level. The plasma treatment time of

≈10 minutes was adopted based on multiple experiments performed to identify the optimum plasma treatment time which resulted in a TFTS coating with minimal contact angle hysteresis (Figure 48). The smoothest substrate exhibited a favorably low contact angle hysteresis (≈20.3°) for TFTS, while the other three samples all have contact angle hysteresis greater than 40° (data is summarized in Table 7). A lower contact angle hysteresis is more favorable for heat transfer applications, since faster droplet shedding increases condensate nucleation rate, resulting in a higher condensation heat transfer coefficient.

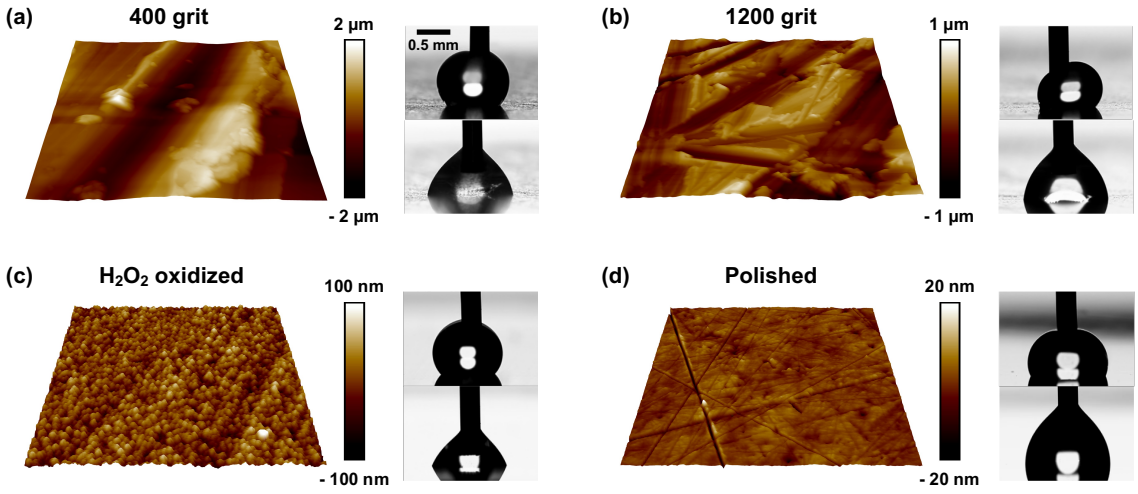

Figure 48. AFM topography images (20 µm by 20 µm) and the corresponding advancing and receding droplet images for copper substrates (a) polished with 400 grit sandpaper, (b) polished with 1200 grit sandpaper, (c) chemically oxidized by hydrogen peroxide, and (d) mechanically polished. All substrates were treated with oxygen plasma for 10 minutes prior to coating TFTS on them.

In Section 4.3.3, we have shown that a controlled/anhydrous environment is essential to creating robust silane SAM coatings during water vapor condensation on silicon substrates. Performing silane SAM synthesis in an ambient environment with moisture leads to uncoated substrate regions (*i.e.*, defects) resulting from (i) silane

agglomerates (or multilayers) caused by cross-linking of silane molecules and/or (ii) preferential wetting of water/moisture on the substrate which shields the substrate from the coating solution. These defects expand during condensation, leading to the degradation of silane SAM coatings. Here, we investigate the roles of the coating environment and oxygen plasma modification on coating durability during water vapor condensation on copper surfaces coated with TFTS. We integrate TFTS on plasma-treated copper surfaces and surfaces not treated by oxygen plasma in both a controlled (*i.e.*, nitrogen glovebox) and an ambient (*i.e.*, fume hood) environment. All substrates were oxidized by H_2O_2 prior to plasma treatment and/or TFTS coating synthesis to ensure that the RMS roughness for the underlying substrate is uniform (Rq ≈23 nm) for all samples. As shown in Figure 49, the sample treated by oxygen plasma and coated in the controlled environment (*i.e.*, OP-C) exhibited a relatively low contact angle hysteresis ≈28.3°. Conversely, the sample treated by oxygen plasma and synthesized in ambient conditions (*i.e.*, OP-A) had a very large advancing angle ≈164.4° and a large hysteresis ≈69.0°, with the receding angle above 90°. For substrates not treated with oxygen plasma (*i.e.*, NP-C and NP-A), however, the droplets advance on the surface in a Cassie-Baxter state with the advancing angles above 160° and a hysteresis greater than 110°. Note, the droplet pinned on the NP-C surface with a receding angle ≈0°. These results indicate that coatings integrated in a controlled environment on plasma-treated copper are more promising candidates to promote dropwise condensation over an extended period.

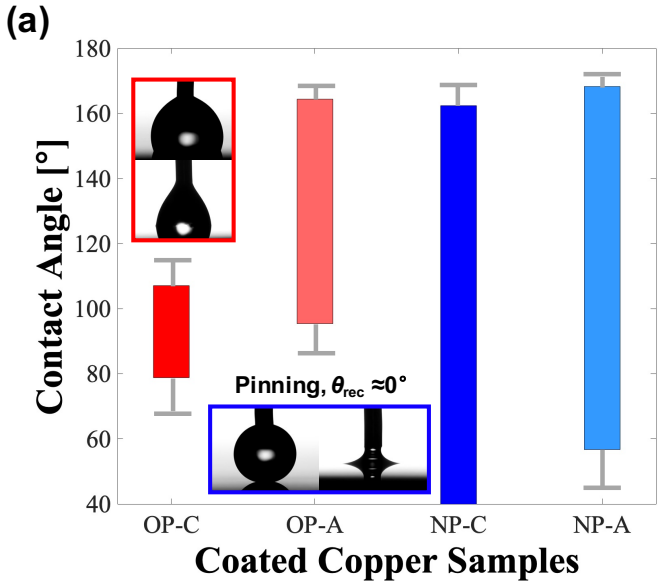

Figure 49. Contact angles measurements on TFTS coatings prepared in a controlled and an ambient environment with different plasma modification methods (*i.e.*, oxygen plasma *v/s* no plasma treatment)

We subsequently characterized the durability of different copper substrates (treated *via* the various methods described earlier) during active water vapor condensation heat transfer in a pure vapor environment. We terminated these durability tests before complete coating failure was achieved for most samples (*i.e.*, we only tested up to ≈360 hours, or 15 days) to avoid a binary pass/fail result due to coating removal, and to facilitate meaningful surface characterization post water vapor condensation. When characterizing the effect of surface roughness on coating durability, all four samples demonstrated partial filmwise condensation to varying degrees after condensing water vapor for ≈360 hours. The vapor and substrate temperatures at steady state were ≈53.9 °C and ≈48.0 °C, respectively (*i.e.*, subcooling ≈5.9 °C). We define coating failure either as regions of the sample which exhibit a transition from dropwise to filmwise condensation, or the presence of large pinned droplets. The substrates polished by 400 grit sandpaper

(Figure 50a) and 1200 grit sandpaper (Figure 50b) maintained small droplet diameters for the first 24 hours, and started to fail from the sample edge after ≈190 hours, when the droplet contact angles noticeably decreased. The area covered by pinned droplets also increased over time. Partial failure was observed around ≈94 hours and ≈24 hours for the H_2O_2 oxidized surface (Figure 50c) and the mechanically polished surface (Figure 50d), respectively. We attribute this early failure on the smoother surfaces to faster droplet shedding with lower contact angle hysteresis (and hence a higher heat/mass transfer rate). Faster nucleation and shedding drives more water vapor to the surface, resulting in a higher heat transfer rate and a larger quantity of pure water interacting with the coating/substrate, leading to faster coating degradation. It is interesting to note that the failure regions on these smoother surface samples did not propagate (*i.e.*, increase in size) significantly up to the termination of the experiment at ≈360 hours, which is different from the rougher surface samples which progressively failed over time.

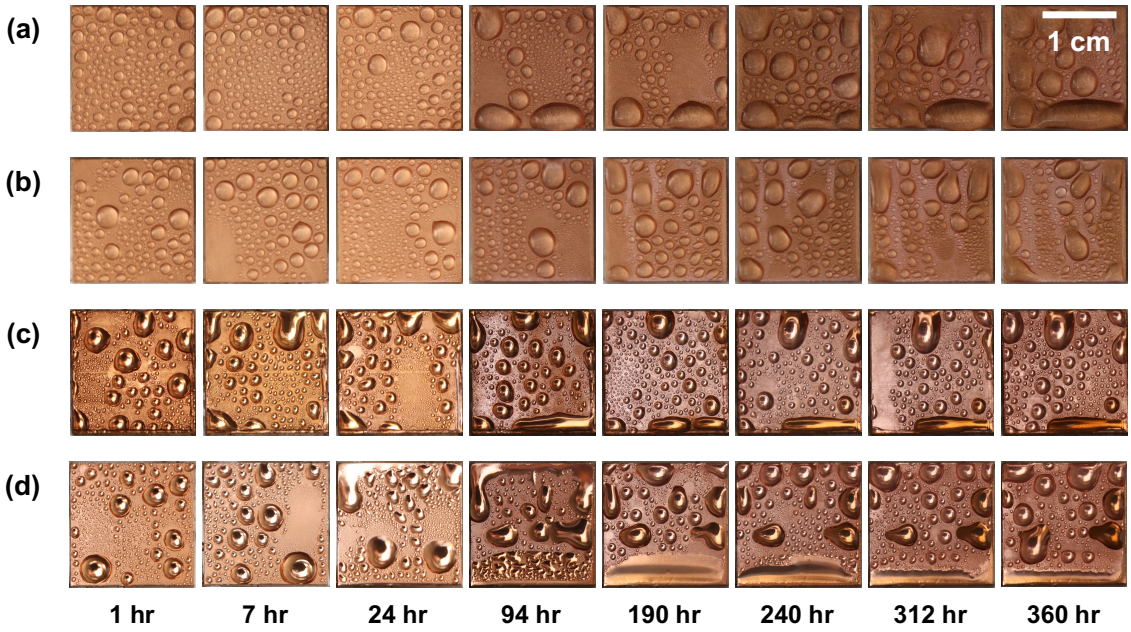

Figure 50. Time-lapse images of continuous water vapor condensation on copper surfaces (a) polished with 400 grit sandpaper, (b) polished with 1200 grit sandpaper, (c) chemically oxidized by hydrogen peroxide, and (d) mechanically polished. All substrates were treated with oxygen plasma for 10 minutes prior to coating TFTS on them.

We then characterized the durability of the samples prepared in the controlled and ambient environments with different plasma modification methods (*i.e.*, OP-C, OP-A, NP-C and NP-A). The subcooling was decreased to ≈1.5 °C (vapor temperature ≈47.8 °C and substrate temperature ≈46.3 °C) from 5.9 °C in the previous test to prolong the lifetime of the NP-C and the -A samples (OP-A and NP-A), and to conclusively demonstrate the benefits of O_2 plasma treatment and the coating condition. Despite the decreased subcooling in this test, the two samples coated in ambient conditions (*i.e.*, OP-A and NP-A) transitioned from dropwise condensation to filmwise condensation within 20 minutes (Figures 51a and 51b) and before a true steady state was achieved for the experiment. This confirmed the importance of the anhydrous synthesis environment in

SAM coating robustness during water vapor condensation discussed in Chapter 4.1. The sample coated in the controlled condition without plasma treatment (*i.e.*, NP-C) started to fail (*i.e.*, partial filmwise) after condensing water vapor for ≈74 hours (Figure 51d), and completely transitioned to the filmwise mode after ≈120 hours. The oxygen plasma treated sample synthesized in the controlled condition (*i.e.*, OP-C) maintained perfect dropwise behavior after ≈360 hours of water vapor condensation (Figure 51c), validating that oxygen plasma modification significantly enhances the coating durability during condensation. Note that testing of this OP-C sample here is a repetition of the sample test reported in Figure 50c (however, at a lower subcooling). Figure 51 visually demonstrates that both a controlled coating environment and oxygen plasma treatment are essential to improving coating robustness during water vapor condensation. A comparison of Figures 50c and 51c also demonstrates that the magnitude of surface subcooling also plays an important role in determining the extent and rate at which coating degradation occurs during water vapor condensation.

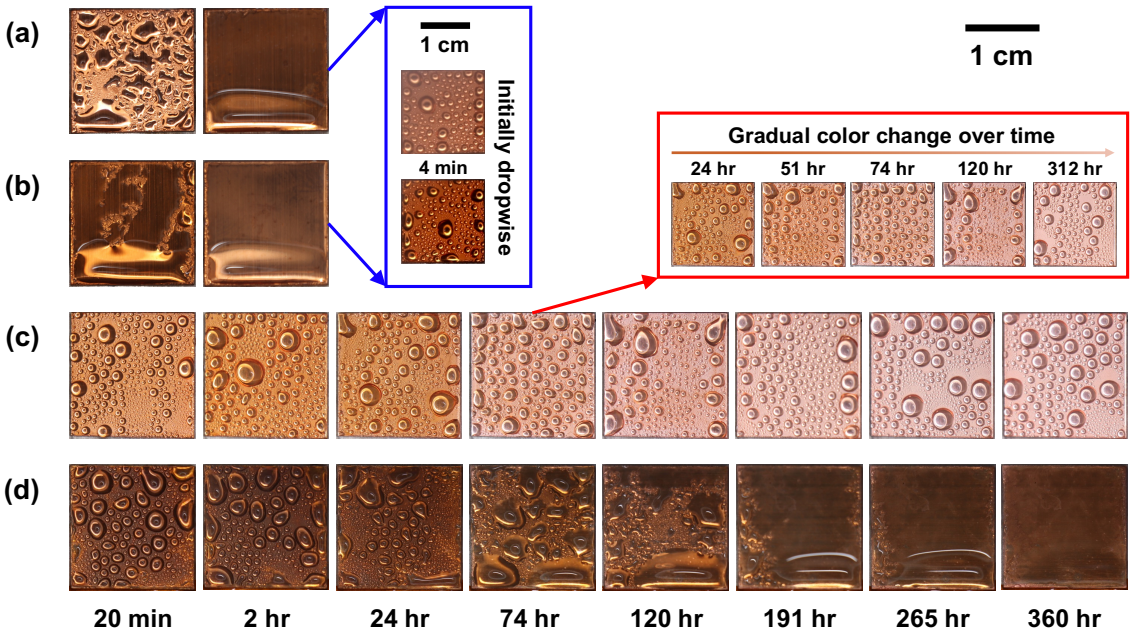

Figure 51. Time-lapse images of continuous water vapor condensation on (a) OP-A, (b) NP-A, (c) OP-C, and (d) NP-C. All samples were chemically oxidized with hydrogen peroxide solution before any plasma treatment and coating synthesis.

We extracted droplet departure sizes for the flat copper samples from videos recorded during the durability tests (time-lapse images reported in Figures 50 and 51), and plotted the changes in the departure diameter over time in Figure 52. For the four samples with different roughness levels (Figure 52a), the departure diameters were significantly different. This difference is despite the fact that they were all treated by oxygen plasma, coated in a controlled condition concurrently, and predominantly exhibited dropwise behavior during the ≈360 hours of water vapor condensation. The 1200 grit sandpaper-roughened copper sample had a considerable increase in the departure diameter from less than 2 mm to over 15 mm over the ≈360 hours of testing. The 400 grit sandpaper-roughened sample showed a steadily increasing trend in the droplet departure diameter, while the chemically oxidized and the mechanically polished samples did not display any

clear trends in the droplet departure sizes over the ≈360 hours of testing. The chemically oxidized copper substrate however did exhibit the lowest droplet departure diameter among all four samples over the course of the experiment. For the test of the samples treated *via* different methods and coated in different conditions, we only captured the departure diameters for the two samples coated in the controlled condition (*i.e.*, OP-C and NP-C, Figure 52b). This was because the coatings prepared in the ambient condition transitioned to a filmwise condensation mode within ≈20 minutes of the experiment starting, and before steady state was achieved. The NP-C sample transitioned to partial filmwise after ≈74 hours and completely failed after ≈120 hours, hence only 4 data points are plotted. The departure diameters on the OP-C samples remained fairly constant (≈4.2 ± 0.5 mm), indicating excellent coating robustness over the ≈360 hours of water vapor condensation (Figure 52b).

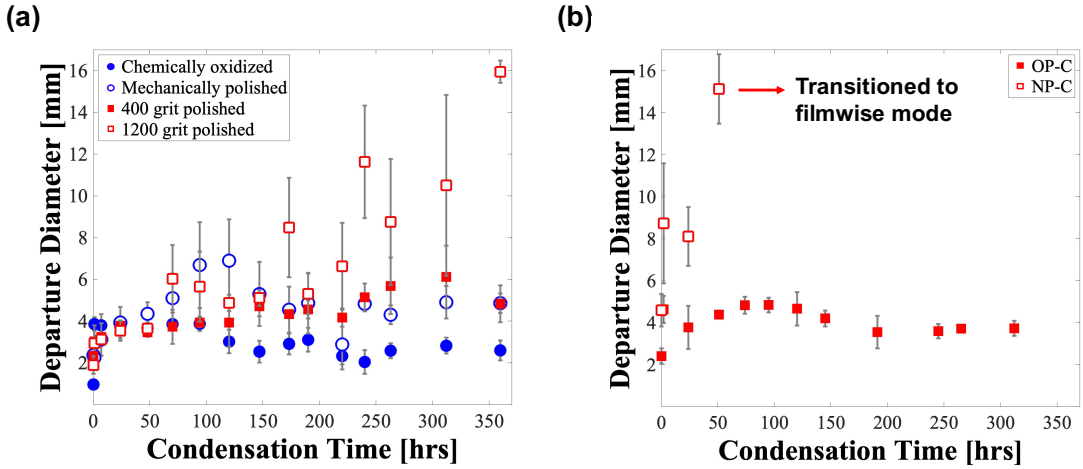

Figure 52. Droplet departure diameters during water vapor condensation experiments on (a) oxygen plasma modified TFTS coated copper substrates with different roughness levels, and (b) samples oxidized by hydrogen peroxide solution and coated with TFTS in the controlled condition.

We *estimated* the effective heat transfer coefficient (HTC) for the coated copper sheets during the durability testing by assuming near-perfect insulation by the polyimide film covering the cold plate, so that heat transfer only occurs on the test samples adhered to the cold plate. Additionally, the estimation does not account for any thermal contact resistances and the thermal resistance from the carbon tape used to mount the sample. The heat flux into the test samples during condensation is estimated by calculating the sensible heat gained by the coolant flowing through the cold plate as shown in eq. 4.23, and the average HTC is estimated from dividing the overall heat flux by the subcooling. For the condensation durability experiment with samples of various roughness levels, the estimated heat flux is ≈228.51 kW/m^2, and the corresponding average HTC (for the samples and the uninsulated region) is 38.47 $kW/m^2 \cdot K$ with an average subcooling of 5.94 °C. If the uninsulated region on the cold plate is considered as filmwise condensation (FWC) and the samples are considered as dropwise condensation, the corrected dropwise HTC is 43.28 $kW/m^2 \cdot K$, assuming all four samples have equivalent heat transfer rates (not strictly true since they exhibited different droplet sizes at departure) and the HTC for dropwise condensation is ≈8× that of FWC. For the condensation durability test with the sheet samples prepared in different coating conditions and with different plasma modification methods, we included two filmwise samples to ensure no contamination in the system. The two samples coated in the ambient conditions failed rapidly (transitioned to filmwise condensation after ≈20 minutes of testing) and before steady state was achieved (≈1.5 hours), hence we also treat these two *failed/degraded* samples as filmwise regions. The estimated heat flux is ≈81.00 kW/m^2 in this experiment. In this test, we

decreased the subcooling ($\Delta T_{subcooling}$ ≈1.49 °C) by introducing a larger amount of vapor/condensate in order to prolong the lifetime of the samples coated in the ambient condition, hence the lower heat flux than the previous test. The average HTC for all six samples and the uninsulated region in this experiment was calculated to be ≈54.50 kW/m^2·K. Similarly, we estimated that the *corrected* dropwise HTC for the two DWC samples coated in the controlled condition is ≈130.80 kW/m^2·K (before the NP-C sample failed).

4.4.3 Post-Condensation Surface Characterization

We first performed surface characterization for copper samples with different roughness levels (shown in Figure 53) after terminating the water vapor condensation durability experiment. In Figures 53a and 53d, we show AFM scans of the H_2O_2 oxidized and the mechanically polished samples after condensation testing (≈360 hours). Several randomly distributed pinholes (≈0.5-2 μm in diameter and ≈100-400 nm in depth) were observed on the surface. Larger pinholes were typically deeper, and the pinhole density was lower on the mechanically polished sample (*i.e.*, the smoothest substrate). The pinholes and silane agglomerates contributed to an observable increase in the RMS roughness, which is ≈2× for the chemically oxidized sample and ≈13× for the mechanically polished sample. The receding contact angles for both samples decreased significantly to <15°. Additionally, the post-condensation Cu peaks obtained by XPS indicated a cuprous oxide (Cu_2O) composition for both the chemically oxidized surface (Figure 53b) and the mechanically polished surface (Figure 53e), even though both

samples had cupric oxide (CuO) signatures (due to oxygen plasma treatment) prior to water vapor condensation testing. Oxygen XPS profiles for both samples (Figures 53c and 53f) comprise of a copper hydroxide peak and a cuprous oxide peak, with a hydroxide-to-oxide ratio of 79:21%. Although the samples polished by 400 grit sandpaper and 1200 grit sandpaper maintained the same level of RMS roughness as before condensation experiments, the receding contact angles decreased to <30°, and the contact angle hysteresis after ≈360 hours of water vapor condensation for these two samples were 88.6° and 80.9°. We believe that pinholes also exist on the samples polished by 400 grit and 1200 grit sandpaper, however the height ranges for the topography are sufficiently large due to the inherent surface roughness that pinholes are not detectable by AFM on these rough substrates. Similar to the smoother surface samples (Figure 53), both sandpaper polished samples had the same Cu_2O profiles (Cu peak) and the metal oxide and hydroxide profiles (O peak) from XPS measurements (Figure 54). The post-condensation characterization results are summarized in Table 7.

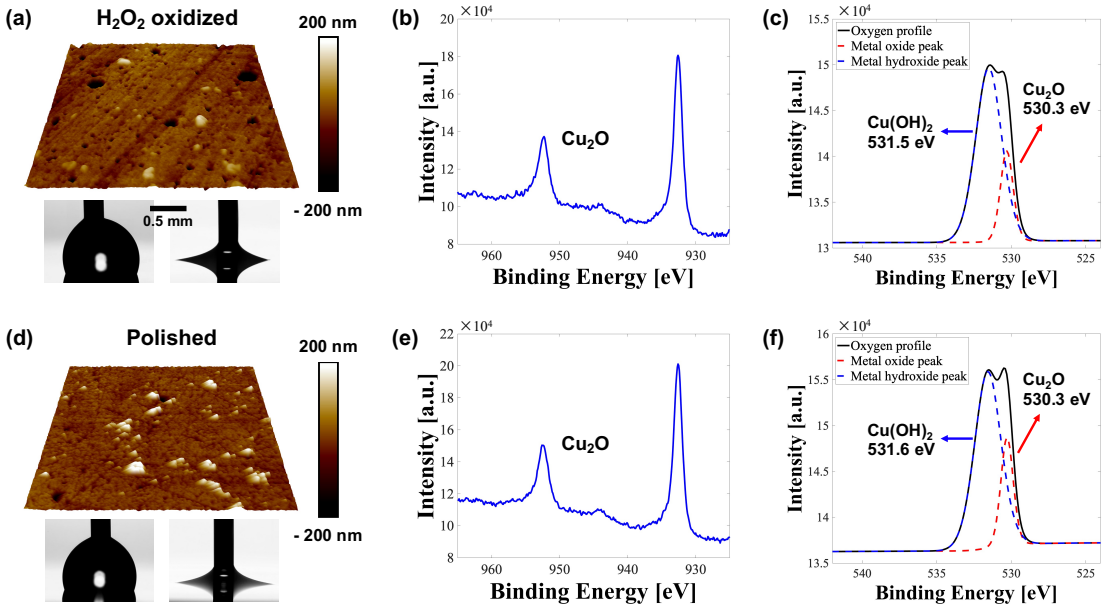

Figure 53. AFM topography images and corresponding XPS scans (for copper and oxygen) after ≈360 hours of water vapor condensation for copper surfaces (a, b and c) chemically oxidized by hydrogen peroxide solution, and (d, e and f) polished by a mechanical polisher.

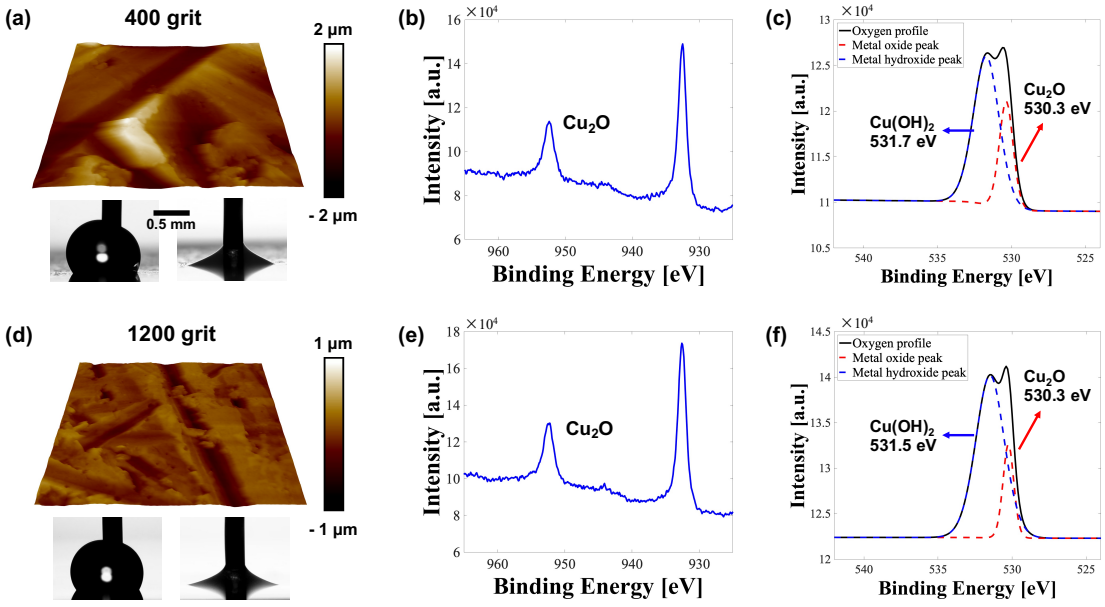

Figure 54. AFM topography images and corresponding XPS scans of copper and oxygen peaks after ≈360 hours of water vapor condensation for copper surfaces (a, b, c) polished with 400 grit sandpaper, and (d, e, f) polished with 1200 grit sandpaper.

Table 7. Surface characterization results for TFTS coated on copper substrates at different roughness levels pre (≈0 hours) and post (≈360 hours) water vapor condensation. All samples were treated by oxygen plasma for 10 minutes, and the coating synthesis was performed in a controlled/anhydrous environment.

Surface Modification	Measurement	Rq (nm)	CAM (°)				
			Adv	Std	Rec	Std	CAH
400 grit	Pre	420	129.1	6.8	73.3	5.3	55.8
	Post	404	117.0	4.8	28.4	8.7	88.6
1200 grit	Pre	232	126.4	11.5	82.6	10.3	43.8
	Post	165	109.2	7.2	28.3	8.4	80.9
Chemically oxidized	Pre	23.0	129.9	7.0	74.5	6.4	54.4
	Post	49.0	98.8	8.7	12.7	3.7	86.1
Mechanically polished	Pre	2.70	110.9	6.4	90.6	4.4	20.3
	Post	36.8	106.8	7.6	14.3	6.4	92.5

We then characterized the samples created in the controlled and ambient environments with different plasma modification methods (*i.e.*, OP-C, OP-A, NP-C and NP-A) after condensing water vapor on them for ≈360 hours. Figures 55a and 55d show the AFM topography scans of the OP-C and the NP-C samples with representative images of receding droplets, respectively. No obvious pinholes were observed for 20 μm by 20 μm AFM scans at multiple locations on the samples. This is attributed to the fact that the coating on the OP-C sample may have been at an initial stage of degradation, and the coating on NP-C sample was completely degraded. A comparison of Figures 55a and 53a further validates our hypothesis that the surface subcooling magnitude affects the rate of coating (and substrate) degradation. The existence of pinholes serves as an indicator for the progression of coating degradation (*i.e.*, partial dropwise mode, Figures 50c and 53a),

and the combined indicators of filmwise condensation and an absence of pinholes demonstrates complete coating removal (Figures 51d and 55d). Although perfect dropwise condensation behavior was observed for the OP-C sample throughout the ≈360 hours experiment, the contact angle hysteresis increased from 28.3° to 64.7° (θ_{adv} =101.9° ±8.2°, θ_{rec} =37.2° ±8.2° after ≈360 hours of condensation), and the RMS roughness also moderately decreased (≈13.9 nm or ≈0.5×) after the condensation experiment, which are signs of a minor degradation of the OP-C sample coating. The XPS copper profile (Figure 55b) indicates that the substrate reduces from cupric oxide (CuO, created by oxygen plasma treatment) to cuprous oxide (Cu_2O) during condensation. The decrease in peak intensity for CF_2 bonds and the disappearance of the CF_3 peak in the XPS carbon profile (Figure 55c) also confirmed the trend of a minor coating degradation, and explains the increase in contact angle hysteresis. The NP-C sample exhibited a higher RMS roughness (≈34.5 nm or ≈1.5×) with several agglomerates on the surface (Figure 55d). The advancing angle changed from 162.4° ±5.9° to 141.1° ±8.7°, and the receding angle reduced to ≈0° with a thin liquid film wetting the surface. This NP-C substrate also transitioned from CuO to Cu_2O similar to the OP-C sample (Figure 55e), but the CuO was created by the chemical oxidation with the hydrogen peroxide solution, since the NP-C sample did not undergo any plasma treatment. Additionally, the disappearance of the CF_2 and CF_3 peaks in the carbon profile suggest a severe-to-complete coating degradation (Figure 55f), which is supported by contact angle measurements. Both the OP-A and the NP-A samples failed by transitioning from the dropwise mode to the filmwise mode within the first 20 minutes of the condensation experiment. Since the

experiment was terminated after ≈360 hours, the coatings were completely degraded when the post-condensation characterization was performed. Figure 56 shows the topography obtained with AFM and XPS copper and carbon spectra. The XPS scans indicated a Cu_2O substrate similar to all other samples after water vapor condensation in the absence of oxygen. No CF_2 or CF_3 peaks were detected in the carbon profile. The peak for the C=O bond on the NP-A sample (Figure 56f) most likely results from the H_2O_2 oxidation step since the NP-A sample did not undergo any plasma modification/treatment. We found that the C=O bond peak exists for all H_2O_2 oxidized copper surfaces regardless of prior surface treatment methods (*i.e.*, solvent cleaning, oxygen plasma or argon plasma treatment), however it disappears after an O_2 plasma treatment.

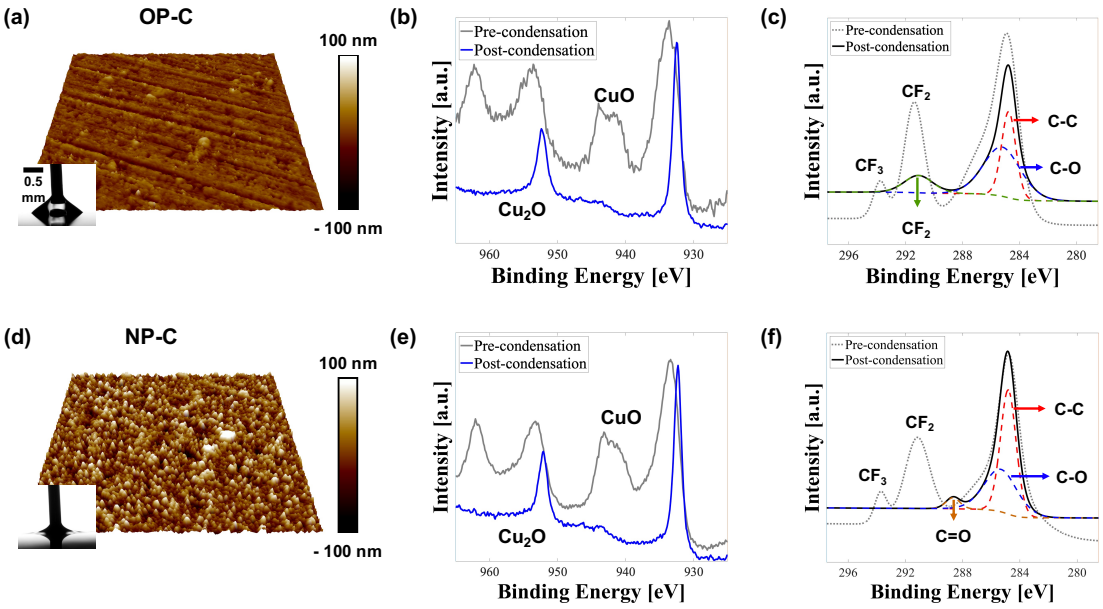

Figure 55. AFM topography images and corresponding XPS scans (copper and carbon) after ≈360 hours of water vapor condensation for (a, b and c) the OP-C sample, and (d, e and f) the NP-C sample.

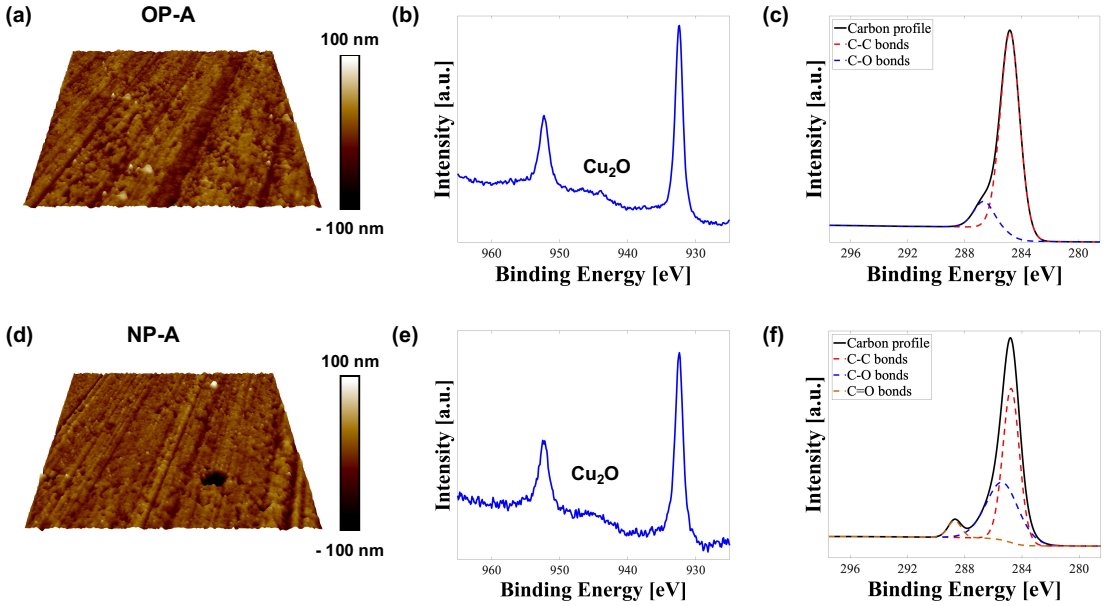

Figure 56. AFM topography images and corresponding XPS scans (copper and carbon) after ≈360 hours of water vapor condensation for (a, b and c) the OP-A sample, and (d, e and f) the NP-A sample.

4.4.4 SAM Degradation Mechanism on Copper

Given the limitation of mechanical polishing with polycrystalline diamonds and the fact that copper is a soft metal, polished copper surfaces cannot be as smooth as silicon surfaces. Despite this, an RMS roughness lower than 3 nm (20 µm by 20 µm) was achieved on flat polished copper surfaces. Due to the minimal thickness of the silane SAM coatings (<2 nm), this level of surface roughness may still contribute to some level of coating defects (*i.e.*, uncoated and/or partially coated regions such as nano-grooves created during polishing), even if the controlled/anhydrous condition eliminates cross-linking of silane molecules and guarantees a monolayer coating. During the process of

condensation, water vapor preferentially condenses on such coating defects due to their higher surface energy compared to the coating. The condensate likely dissolves or reduces the oxide interfacial layer between the copper substrate and coating as shown in Figures 53a and 53d, creating pinholes and delaminating the silane monolayer coating. Therefore, we suggest that coating degradation originates from coating defects and propagates during condensation. However, since the pinholes are randomly distributed and only occupy part of the surface, a majority of the surface area would remain coated, leading to partial dropwise condensation with complete degradation likely over extended periods. The significantly decreased receding contact angles (*i.e.*, droplets pinning at the defects, shown in the insets of Figures 53a and 53d) result from these pinholes (or exposed substrate regions), because the receding contact angle is determined by hydrophilic defects on a hydrophobic surface based on the model reported by Raj et al. The post condensation XPS results indicate that the cupric oxide (CuO) layer was reduced to cuprous oxide (Cu_2O) for all surface treatments (Figure 55b for the OP-C sample, Figures 53b and 53e for the chemically oxidized and mechanically polished samples, and Figure 55e for the NP-C sample). Thus, it is likely that this reduction chemical reaction occurs at defect sites during water vapor condensation regardless of the extent of coating degradation. The gradual change in the surface color (especially obvious on the OP-C sample shown in Figure 51c and the inset highlighted in the red box) qualitatively confirms the occurrence of chemical reactions at the coating substrate interface. Substrate color changes while maintaining good dropwise condensation were previously observed by Marto *et. al.* on polymer coated surfaces (nominally a thicker coating).[56] They reported that copper nickel

coated with Nedox® turned dark after 24 hours, copper and brass coated with No-stik turned green after 22,000 hours, and copper nickel coated with NRL C-6 Fluoroepoxy turned black after 1,000 hours. They claimed that the color change of the copper surface was attributable to the oxidation of the copper substrates, which is consistent with the change in color they observed (black and green being common colors of oxides of copper). However, we believe that what we observed in Figure 51c was a reduction reaction instead of oxidation, with the color approaching that of bare copper. This observation is validated by the XPS spectra that show a transition from CuO to Cu_2O. Further studies are required to probe the degradation behavior over time from a local (*i.e.*, coating-substrate interface) and global (*i.e.*, applied heat transfer) perspective, which will shed additional light on the degradation mechanism.

4.4.5 Condensation Heat Transfer Measurements

We integrated the TFTS SAM coating on a polished and oxygen plasma-modified copper tubes to precisely characterize heat transfer performance during water vapor condensation. The lengths (for two separate experiments), outer diameter (OD) and wall thickness of the copper tubes were ≈124 mm and ≈128 mm, 6.35 mm, and 0.89 mm, respectively. The surface *Rq* after polishing was 7.98 nm (20 μm by 20 μm scan area) obtained by AFM (Figure 57a). Perfect dropwise condensation was observed immediately (Figure 58a) on this TFTS-coated copper tube when water vapor was introduced into the testing chamber. We varied the subcooling from 1.6 °C to 15.3 °C by adjusting the coolant temperature, while the wet-bulb temperature in the chamber was maintained at ≈48.5 °C

(standard deviation <0.1 °C). The measured heat fluxes in the dropwise and filmwise experiments at various subcoolings are shown in Figure 58b, and the calculated condensation heat transfer coefficients (HTCs) from measurements and a 1D thermal resistance network are reported in Figure 58c. The dropwise experiment (*i.e.*, TFTS coated copper tube) demonstrated a higher heat flux compared to the filmwise experiment (*i.e.*, copper tube oxidized by H_2O_2 then treated by oxygen plasma, no TFTS coating) and the Nusselt model, and the corresponding dropwise HTC is ≈5~7× enhancement compared to the filmwise HTC. The measured vapor pressure in the test chamber always matched the saturation pressure (standard deviation <0.02 kPa) corresponding to the wet-bulb temperature, which indicated a NCG free environment. We performed two separate dropwise condensation tests with TFTS coated tubes under the same experimental conditions to show the reproducibility of the heat transfer data. We also compared the heat flux obtained from our first dropwise condensation experiment against previous work in literature[32, 125] that used the same TFTS coating and the similar coolant conditions for a wide range of log mean temperature difference values (Figure 57b). The higher heat flux reported in this current work is likely due to a combination of the lower level of NCGs in our experiment and a minor enhancement effect from the higher vapor temperature.

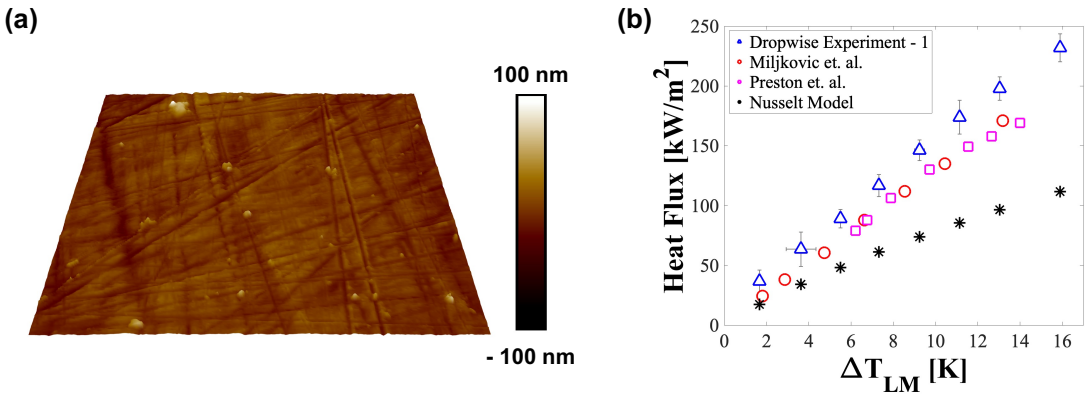

Figure 57. (a) AFM topography image of a polished copper tube (Rq ≈7.98 nm) on a 20 µm by 20 µm area. (b) A comparison of the measured heat flux as a function of the log mean temperature difference (LMTD) from the current work and available results from literature, Miljkovic *et al.*[32] and Preston *et al.*[125]

After obtaining the data at different subcooling (≈2.5 hours, for the first dropwise test), we adjusted the subcooling to be ≈5.3 °C and continued the experiment for 2 hours to monitor the HTC as a function of time (Figure 58d). The first steady state data point for this constant subcooling longevity test (≈2.6 hours after the experiment was started) is plotted in magenta in Figures 58b and 58c. It overlaps with the previous data point obtained at that subcooling (≈1 hour after the experiment was started). This indicates that the coating did not degrade over the first 2.5 hours of condensation, and also validates the absence of any NCGs in the vapor environment. Although the HTC appears to marginally decrease between 2.5 and 4.5 hours (for the first dropwise test) at a constant subcooling ≈5.3 °C, the estimated change in HTC is within the uncertainty of the measurement. Additionally, the HTC at the end of the experiment was higher than the filmwise HTC (factor of ≈5×), and the tube visually showed perfect dropwise behavior when the experiment was terminated (Figure 58e). Similarly for the second dropwise condensation test, the HTC remained constant between 3.5 and 4.5 hours at a constant subcooling

≈5.2 °C and condensation appeared to be occurring in the dropwise mode. The estimated HTC for these two individual dropwise experiments perfectly matched from 3.5 to 4.5 hours. The experiments were terminated intentionally at 4.5 hours due to constraints of the test setup for the tube heat transfer measurement configuration.

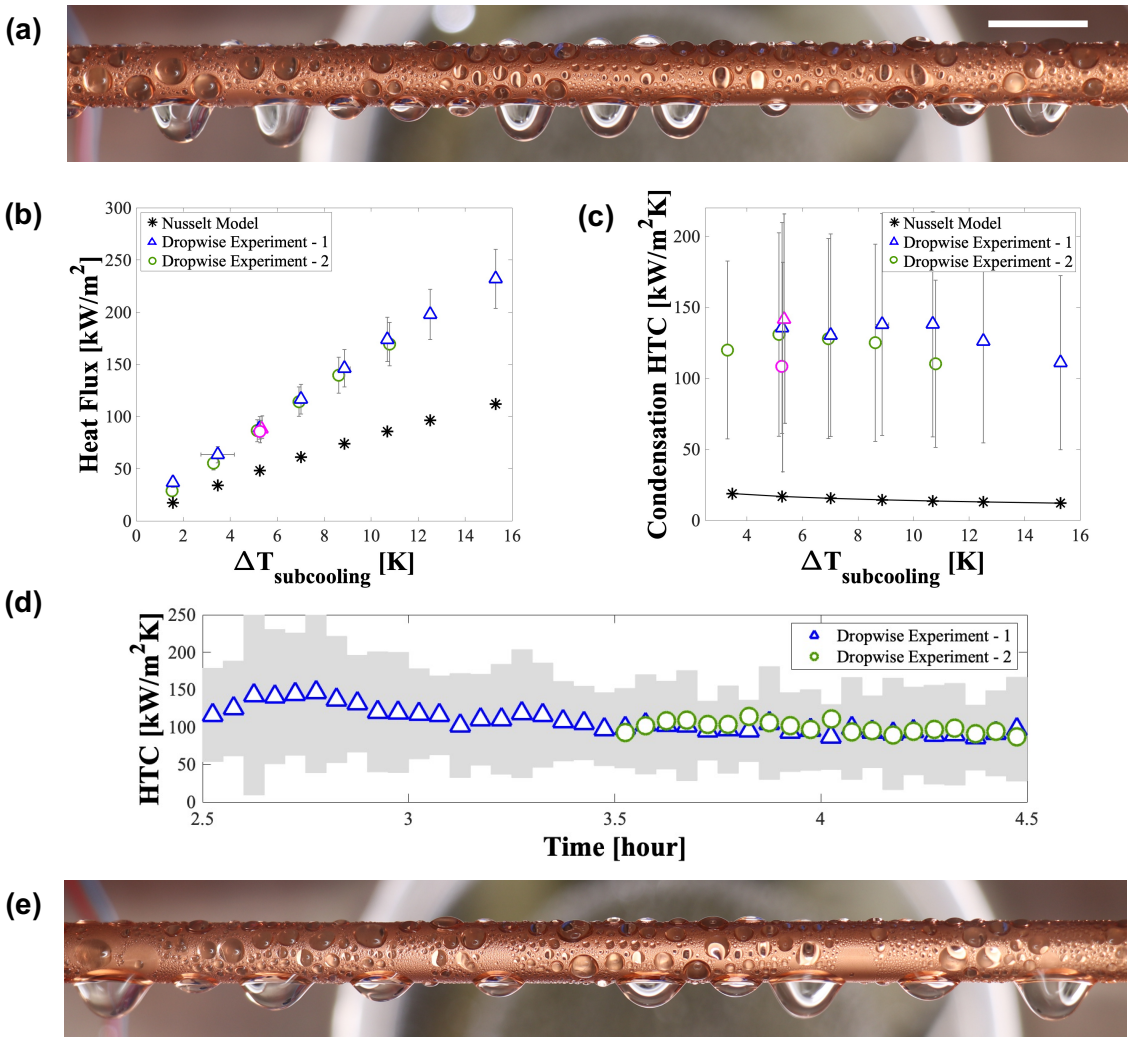

Figure 58. Dropwise condensation on a TFTS-coated copper tube with the subcooling at ≈5.2°C. (b) Measurement of the condensation heat flux and (c) calculated heat transfer coefficient (HTC) for two separate dropwise experiments at different subcoolings. (d) Calculated HTC over time at subcoolings of ≈5.3°C and ≈5.2°C for dropwise experiments 1 and 2, respectively. The tube sample maintained perfect dropwise for ≈4.5 hours as shown in (e), when the experiment was terminated.

4.5 Chapter Summary

In this chapter, we elucidated the degradation mechanisms of organofunctional silane self-assembled monolayer coatings integrated on *silicon* and *copper* surfaces during continuous condensation of pure water vapor. Various surface characterization methods, condensation durability tests, condensation heat transfer performance measurement, and the pre- and post-condensation characterizations of molecular bonding and coating substrate interfacial interactions also validated our proposed condensation-mediated failure mechanisms. We leveraged this knowledge to develop stringent synthesis procedures for silane SAM coatings and substrate preparation methods for silicon and copper surfaces in order to suppress the defect formation, and more importantly to extend the lifetime of SAM coating promoting efficient dropwise condensation on widely used heat exchanger materials. The advancements and novel understanding from this chapter will enable the development of durable ultra-thin coatings for enhanced heater transfer technologies in a variety of industrial applications such as electronics thermal management, semiconductor industries, and energy conversion systems.

CHAPTER V

CONCLUSIONS & FUTURE WORK

5.1 Dissertation Summary

5.1.1 Surface Geometry Method

In the surface geometry method of enhancing liquid-vapor phase change heat transfer, we report a novel mode of condensation (*i.e.*, capillary-enhanced filmwise mode) where the condensate is wicked away by a porous condenser surface and the capillary enhanced condensate removal is supported by an external pump for the condensate removal from the condenser. This mode enhances phase change heat transfer *via* increasing the effective thermal conductivity of the porous wick and the liquid, without flooding the surface. A detailed non-CFD based modeling framework is presented to model the general problem of fluid flow through porous media in phase change processes (*i.e.*, condensation and evaporation) with excellent accuracy resulting from accounting for the nonlinear variation in the pressure drop in the modeling domain. Discretizing the porous wick structure enables us to solve for the local pressure gradient in the wick instead of assuming a linear pressure gradient, and contributes to an accurate prediction of the condensate flow velocity and the condensation rate, both of which are obtained by iterating the model with updated pressure gradients. We further improve the model accuracy by incorporating the local meniscus curvature/shape within the discretized modeling unit cell and utilizing an effective liquid height/thickness in the model. Moreover, a liquid permeability submodel is reported based on the local meniscus shape that compares well

with 3D CFD simulations and demonstrates superior accuracy compared to available permeability models in literature. We have applied this modeling framework to both condensation and evaporation phase change heat transfer to predict the heat transfer coefficient enhancement and the dry-out heat flux, respectively, and the accuracy is validated against available experimental data in literature. The comparison of different modeling methods (*i.e.*, discretization and applying different properties such as permeability and liquid height) highlights the importance of: (i) incorporating the effect of the liquid-vapor interface with local liquid properties, and (ii) discretizing the flow domain to obtain an accurate pressure profile along the porous media. More importantly, the capillary-enhanced filmwise condensation mode demonstrates significant enhancements in the heat transfer coefficient for various low surface tension liquids, where the enhancement depends on the wick geometry and the liquid properties.

This surface geometry method overcomes the limitation of enhancing condensation for low surface tension liquids and offers a durable solution to enhance condensation heat transfer without any low surface energy coatings that have been shown to degrade over time. This work also presents a complete methodology to model the general steady state liquid-vapor phase change processes in porous media, and it can be applied to design and optimize the surface geometry for liquid-vapor phase change heat transfer applications in thermal management and energy conversion systems.

5.1.2 Surface Energy Method

In the surface energy method of enhancing liquid-vapor phase change heat transfer, we significantly enhance the durability of self-assembled monolayer (SAM) coatings deposited on silicon and copper surfaces during continuous water vapor condensation by elucidating the condensation-mediated degradation mechanism of SAM coatings. We have proposed and experimentally validated our hypothesis that the organofunctional silane SAM coatings degrade when condensing water vapor because of the expansion of the defects within the SAM coating. These degradation nucleation site defects are likely uncoated substrate regions that dissolve in the presence of pure water that is actively and continuously transported to the coating-substrate interface during condensation. We propose that these defects primarily form during coating synthesis procedures in uncontrolled environments with unregulated water/moisture content *via*: (i) hydrolysis and cross-linking of silane molecules in wet conditions that result in bulk silane agglomerates and multilayers, and (ii) preferential wetting of the silicon substrate by moisture/water in a non-anhydrous environment that shields the uncoated substrate from the silane molecules in the solution. We experimentally demonstrate that the silane SAM coatings deposited in an anhydrous coating environment exhibit higher quality (*i.e.*, lower RMS roughness and minimal contact angle hysteresis), and more importantly, the favorable surface properties of coatings synthesized under anhydrous conditions result in better condensation performance for extended periods during condensation heat transfer testing compared to the coatings deposited in the uncontrolled/ambient environment. We further

leverage this knowledge to develop robust SAM coatings on copper surfaces *via* (i) polishing the copper surface to an ultra-smooth level to minimize any uncoated defects and achieve low contact angle hysteresis, and (ii) introducing a pure oxygen plasma to terminate the copper substrate with sufficient copper hydroxide for better bonding with SAM molecules. We hypothesize and verify that the oxygen plasma removes surface-bound hydrocarbons and chemically transforms the substrate into a complete cupric oxide layer with a copper hydroxide interface. Our condensation heat transfer measurements on TFTS-coated plasma-modified copper tubes demonstrate heat transfer coefficients (≈5-7× over the filmwise HTC) comparable to the maximum HTCs expected from the dropwise mode while sustaining visually perfect dropwise behavior on the copper tube for extended periods of time. Additionally, we reveal that a reduction reaction from cupric oxide (CuO) to cuprous oxide (Cu_2O) occurs at the substrate interface based on the post-condensation characterization. This observation is different from a prior hypothesized oxidative degradation mechanism for copper surfaces coated with low surface energy materials, and our hypothesis is further supported by the substrate color change which visibly transitioned from dark brown to bright orange/pink during water vapor condensation. Overall, with the stringent coating procedure and sample preparation procedure (*i.e.*, cleaning, polishing, plasma treatment), the SAM coatings we deposited in the anhydrous/controlled condition maintained perfect dropwise condensation with no signs of coating failure for 460 hours and 360 hours for silicon and copper substrates respectively (note that the experiments were terminated at that time in order to characterize the surface properties, not because of coating failure). Various surface characterization

methods (*e.g.*, XPS, AFM, ellipsometry, CAM) have been used to capture the coating/interface properties and the coating degradation before and after condensation heat transfer experiments, validating the proposed condensation-mediated degradation mechanism of SAM coatings for both silicon and copper substrates.

The surface energy method work presented here provides a mechanistic understanding of the condensation-mediated degradation of self-assembled monolayer coatings which has not been solved for decades, and considerably increases the lifetime of low surface energy coatings promoting efficient dropwise condensation on typical industrial condenser materials. This work highlights the importance of the coating procedure, synthesis environment, and substrate activation/preparation in facilitating long-term coating durability for enhanced phase change heat transfer applications, and the outcomes from this will enable the development of durable ultrathin coatings for a variety of water-energy industries such as power generation and water harvesting/desalination.

5.2 Future Work

5.2.1 Time dependent surface characterization & Extended longevity test

In the previous coating durability tests during water vapor condensation, we terminated the experiments after 460 hours and 360 hours for SAM coatings deposited on silicon and copper surfaces respectively for the purpose of characterizing the coating properties before the coatings completely degrade. We demonstrated coating degradation through the changes of condensation modes, contact angles, surface topographies and chemical compositions, however, only the pre- and post-condensation states were

captured. We propose to perform the time dependent surface characterizations by repeating the condensation experiments and terminating them after different time periods (*e.g.*, hours to days), through which the coating failure (*i.e.*, changes of surface properties) can be monitored as a function of time. This would provide further information on coating degradation and assist in improving the coating durability during water vapor condensation.

Additionally, perfect dropwise condensation was maintained on the OTCS-coated silicon wafer (*i.e.*, OTCS controlled) and the TFTS-coated copper with the oxygen plasma modification (*i.e.*, OP-C) without any sign of coating failure at the time the experiments stopped, however, the actual lifetime of the coatings deposited in the controlled environment remains unknown. We plan to test the longevity of the best coatings until complete failure (*i.e.*, transition to filmwise mode on the entire surface) in order to offer a thorough evaluation of our SAM coatings and show the advantage of the synthesis procedure we developed.

5.2.2 Enhanced Jumping Droplet Condensation

As discussed in Section 2.3.3, the jumping droplet mode of condensation fails at higher subcoolings with the condensate flooding the texture structures. We propose to apply the stringent coating procedures we report here and conduct the synthesis in a controlled environment to achieve a more complete and conformal SAM coating on the nanostructured substrate. Also, the extremely low leak rate (<0.5 Pa/hr) of our experimental system guarantees a minimal amount of non-condensable gases even during

a long-term condensation test. Thus, improving the coating quality and creating the NCG-free environment are expected to push the boundary of subcoolings and delay the failure of the jumping droplet mode while maintaining a large heat transfer coefficient.

REFERENCES

1. Pop, E., Energy dissipation and transport in nanoscale devices. *Nano Research* **2010,** *3* (3), 147-169.

2. Faghri, A., *Heat pipe science and technology*. Taylor & Francis: Washington, DC, 1995.

3. Reay, D.; McGlen, R.; Kew, P., *Heat pipes*. 2014.

4. Mudawar, I., Assessment of high-heat-flux thermal management schemes. In *IEEE Transactions on Components and Packaging Technologies*, IEEE: 2001.

5. Majumdar, A., Thermoelectric devices: Helping chips to keep their cool. *Nat Nanotechnol* **2009,** *4* (4), 214-215.

6. Attinger, D.; Frankiewicz, C.; Betz, A. R.; Schutzius, T. M.; Ganguly, R.; Das, A.; Kim, C.-J.; Megaridis, C. M., Surface engineering for phase change heat transfer: A review. *MRS Energy & Sustainability* **2014,** *1* (1).

7. Carey, V. P., *Liquid-vapor phase-change pheomena*. 2nd ed.; Taylor & Francis: New York, 2008; p xxii, 742 p.

8. Cho, J. H.; Preston, D. J.; Zhu, Y.; Wang, E. N., Nanoengineered materials for liquid-vapour phase-change heat transfer. *Nature Review Materials* **2016,** *2* (16092).

9. Webb, R. L., Kim, Nae-Hyun, *Principles of enhanced heat transfer*. 2005.

10. Shakouri, A., Nanoscale thermal transport and microrefrigerators on a chip. *Proceedings of the IEEE* **2006,** *94* (8), 1613-1638.

11. Yang, S.; Xiang, D.; Bryant, A.; Mawby, P.; Ran, L.; Tavner, P., Condition monitoring for device reliability in power electronic converters: A review. *IEEE Transactions on Power Electronics* **2010,** *25* (11), 2734-2752.

12. Beér, J. M., High efficiency electric power generation: The environmental role. *Progress in Energy and Combustion Science* **2007,** *33* (2), 107-134.

13. Enright, R.; Miljkovic, N.; Alvarado, J. L.; Kim, K.; Rose, J. W., Dropwise condensation on micro- and nanostructured surfaces. *Nanoscale and Microscale Thermophysical Engineering* **2014,** *18* (3), 223-250.

14. Khan, S. A.; Tahir, F.; Baloch, A. A. B.; Koc, M., Review of micro–nanoscale surface coatings application for sustaining dropwise condensation. *Coatings* **2019,** *9* (2).

15. de Gennes, P.-G.; Brochard-Wyart, F.; Quéré, D., *Capillarity and wetting phenomena: Drops, bubbles, pearls, waves*. New York : Springer: 2004.

16. Quéré, D., Wetting and roughness. *Annual Review of Materials Research* **2008,** *38* (1), 71-99.

17. Ćoso, D.; Srinivasan, V.; Lu, M.-C.; Chang, J.-Y.; Majumdar, A., Enhanced heat transfer in biporous wicks in the thin liquid film evaporation and boiling regimes. *Journal of Heat Transfer* **2012,** *134* (10).

18. Betz, A. R.; Jenkins, J.; Kim, C. J.; Attinger, D., Boiling heat transfer on superhydrophilic, superhydrophobic, and superbiphilic surfaces. *International Journal of Heat and Mass Transfer* **2013,** *57* (2), 733-741.

19. Betz, A. R.; Xu, J.; Qiu, H.; Attinger, D., Do surfaces with mixed hydrophilic and hydrophobic areas enhance pool boiling? *Applied Physics Letters* **2010,** *97* (14).

20. Liang, G. T.; Mudawar, I., Review of pool boiling enhancement by surface modification. *International Journal of Heat and Mass Transfer* **2019,** *128*, 892-933.

21. Hou, Y.; Yu, M.; Chen, X.; Wang, Z.; Yao, S., Recurrent filmwise and dropwise condensation on a beetle mimetic surface. *ACS Nano* **2015,** *9* (1), 71-81.

22. Lo, C.-W.; Chu, Y.-C.; Yen, M.-H.; Lu, M.-C., Enhancing condensation heat transfer on three-dimensional hybrid surfaces. *Joule* **2019,** *3* (11), 2806-2823.

23. Peng, B.; Ma, X.; Lan, Z.; Xu, W.; Wen, R., Experimental investigation on steam condensation heat transfer enhancement with vertically patterned hydrophobic–hydrophilic hybrid surfaces. *International Journal of Heat and Mass Transfer* **2015,** *83*, 27-38.

24. Chatterjee, A.; Derby, M. M.; Peles, Y.; Jensen, M. K., Condensation heat transfer on patterned surfaces. *International Journal of Heat and Mass Transfer* **2013,** *66*, 889-897.

25. Wilke, K. L.; Kalinina, K. B.; Zhu, Y.; Preston, D. J.; Antao, D. S.; Adera, S.; Wang, E. N., Enhancement of dry-out heat flux in nonuniform avriable-permeability wicking structures. In *Proceedings of the 16th International Heat Transfer Conference, IHTC-16*, Beijing, China, 2018.

26. Preston, D. J.; Lu, Z.; Song, Y.; Zhao, Y.; Wilke, K. L.; Antao, D. S.; Louis, M.; Wang, E. N., Heat transfer enhancement during water and hydrocarbon condensation on lubricant infused surfaces. *Sci Rep* **2018,** *8* (1), 540.

27. Preston, D. J.; Wang, E. N., Jumping droplets push the boundaries of condensation heat transfer. *Joule* **2018,** *2* (2), 205-207.

28. Ma, J.; Sett, S.; Cha, H.; Yan, X.; Miljkovic, N., Recent developments, challenges, and pathways to stable dropwise condensation: A perspective. *Applied Physics Letters* **2020,** *116* (26).

29. Khalil, K.; Soto, D.; Farnham, T.; Paxson, A.; Katmis, A. U.; Gleason, K.; Varanasi, K. K., Grafted nanofilms promote dropwise condensation of low-surface-tension fluids for high-performance heat exchangers. *Joule* **2019,** *3* (5), 1377-1388.

30. Liu, Z.; Preston, D. J., Enhanced condensation for improved energy efficiency. *Joule* **2019,** *3* (5), 1182-1184.

31. Nusselt, W., The surface condensation of water vapour. *Zeitschrift Des Vereines Deutscher Ingenieure* **1916,** *60*, 541-546.

32. Miljkovic, N.; Enright, R.; Nam, Y.; Lopez, K.; Dou, N.; Sack, J.; Wang, E. N., Jumping-droplet-enhanced condensation on scalable superhydrophobic nanostructured surfaces. *Nano Lett* **2013,** *13* (1), 179-187.

33. Lee, S.; Cheng, K.; Palmre, V.; Bhuiya, M. D. M. H.; Kim, K. J.; Zhang, B. J.; Yoon, H., Heat transfer measurement during dropwise condensation using micro/nano-scale porous surface. *International Journal of Heat and Mass Transfer* **2013,** *65*, 619-626.

34. B. W. Tanner, C. J. P., D. Pope aad D. West, Heat transfer in dropwise condensation—part i the effects of heat flux, steam velocity and non-condensable gas concentration. *International Journal of Heat and Mass Transfer* **1965**.

35. Ma, X.; Tao, B.; Chen, J.; Xu, D.; Lin, J., Dropwise condensation heat transfer of steam on a polytethefluoroethylene film. *Journal of Thermal Science* **2001**.

36. Chang, W.; Peng, B.; Egab, K.; Zhang, Y.; Cheng, Y.; Li, X.; Ma, X.; Li, C., Few-layer graphene on nickel enabled sustainable dropwise condensation. *Science Bulletin* **2021,** *66* (18), 1877-1884.

37. Zhang, B. J.; Kuok, C.; Kim, K. J.; Hwang, T.; Yoon, H., Dropwise steam condensation on various hydrophobic surfaces: Polyphenylene sulfide (pps), polytetrafluoroethylene (ptfe), and self-assembled micro/nano silver (sams). *International Journal of Heat and Mass Transfer* **2015,** *89*, 353-358.

38. B. W. Tanner, C. J. P., D. Pope aad D. West, Heat transfer in dropwise condensation at low steam pressures in the absence and presence of non-condensable gas. *International Journal of Heat and Mass Transfer* **1968**.

39. Cavallini, A.; Censi, G.; Del Col, D.; Doretti, L.; Longo, G. A.; Rossetto, L.; Zilio, C., Condensation inside and outside smooth and enhanced tubes — a review of recent research. *International Journal of Refrigeration* **2003,** *26* (4), 373-392.

40. Cavallini, A.; Del Col, D.; Doretti, L.; Longo, G. A.; Rossetto, L., Heat transfer and pressure drop during condensation of refrigerants inside horizontal enhanced tubes. *Int J Refrig* **2000,** *23* (1), 4-25.

41. Dalkilic, A. S.; Wongwises, S., Intensive literature review of condensation inside smooth and enhanced tubes. *International Journal of Heat and Mass Transfer* **2009,** *52* (15-16), 3409-3426.

42. Ji, W.-T.; Chong, G.-H.; Zhao, C.-Y.; Zhang, H.; Tao, W.-Q., Condensation heat transfer of r134a, r1234ze(e) and r290 on horizontal plain and enhanced titanium tubes. *International Journal of Refrigeration* **2018,** *93*, 259-268.

43. Shekarriz, A.; Plumb, O. A., Enhancement of film condensation using porous fins. *Journal of Thermophysics and Heat Transfer* **1989,** *3* (3), 309-314.

44. Renken, K. J.; Mueller, C. D., Measurements of enhanced film condensation utilizing a porous metallic coating. *Journal of Thermophysics and Heat Transfer* **1993,** *7* (1), 148-152.

45. Preston, D. J.; Wilke, K. L.; Lu, Z.; Cruz, S. S.; Zhao, Y.; Becerra, L. L.; Wang, E. N., Gravitationally driven wicking for enhanced condensation heat transfer. *Langmuir* **2018,** *34* (15), 4658-4664.

46. Goswami, A.; Pillai, S. C.; McGranaghan, G., Surface modifications to enhance dropwise condensation. *Surfaces and Interfaces* **2021,** *25*.

47. Das, A. K.; Kilty, H. P.; Marto, P. J.; Andeen, G. B.; Kumar, A., The use of an organic self-assembled monolayer coating to promote dropwise condensation of steam on horizontal tubes. *Journal of Heat Transfer* **2000,** ***122*** (2), 278-286.

48. Rose, J. W., Dropwise condensation theory and experiment: A review. *Proceedings of the Institution of Mechanical Engineers, Part A: Journal of Power and Energy* **2002,** *216* (2), 115-128.

49. Bonner III, R. W. In *Dropwise condensation life testing of self-assembled monolayers*, Proceedings of the International Heat Transfer Conference, 2010.

50. Torresin, D.; Tiwari, M. K.; Del Col, D.; Poulikakos, D., Flow condensation on copper-based nanotextured superhydrophobic surfaces. *Langmuir* **2013,** *29* (2), 840-848.

51. Depew, C. A.; Reisbig, R. L., Vapor condensation on a horizontal tube using teflon to promote dropwise condensation. *Industrial & Engineering Chemistry Process Design and Development* **1964,** *3*, 365-369.

52. Holden, K. M. An evaluation of polymer coatings for the promo- tion of dropwise condensation of steam. Naval Postgraduate School, Monterey, CA, 1984.

53. Marto, P. J.; Nunn, R. H. A critical review of heat transfer enhancement techniques for use in marine condensers. Naval Postgraduate School, Monterey, California, 1982.

54. Wilke, K. L.; Antao, D. S.; Cruz, S.; Iwata, R.; Zhao, Y.; Leroy, A.; Preston, D. J.; Wang, E. N., Polymer infused porous surfaces for robust, thermally conductive, self-healing coatings for dropwise condensation. *ACS Nano* **2020,** *14* (11), 14878-14886.

55. Holden, K. M.; Wanniarachchi, A. S.; Marto, P. J.; Boone, D. H.; Rose, J. W., The use of organic coatings to promote dropwise condensation of steam. *Journal of Heat Transfer* **1987,** *109* (3), 768-774.

56. Marto, P. J.; Looney, D. J.; Rose, J. W.; Wanniarachchi, A. S., Evaluation of organic coatings for the promotion of dropwise condensation of steam. *International Journal of Heat and Mass Transfer* **1986,** *29* (8), 1109-1117.

57. Reed Jr, C. O. Promotion of dropwise condensation by silicones. The University pf Missouri, Rolla, Missouri, 1956.

58. Bigelow, W. C.; Pickett, D. L.; Zisman, W. A., Oleophobic monolayers: I. Films adsorbed from solution in non-polar liquids. *Journal of Colloid Science* **1946,** *1* (6), 513-538.

59. Blackman, L. C. F.; Dewar, M. J. S., Promoters for the dropwise condensation of steam. *Journal of the Chemical Society* **1957**, 171-176.

60. Blackman, L. C. F.; Dewar, M. J. S.; Hampson, H., An investigation of compounds promoting the dropwise condensation of steam. *Journal of Applied Chemistry* **1957**, 160-171.

61. Bonner III, R. W., Dropwise condensation in vapor chambers. In ***26th IEEE SEMI-THERM Symposium***, 2010.

62. Chen, C.-H.; Cai, Q.; Tsai, C.; Chen, C.-L.; Xiong, G.; Yu, Y.; Ren, Z., Dropwise condensation on superhydrophobic surfaces with two-tier roughness. *Applied Physics Letters* **2007,** *90* (17).

63. Chen, L.; Liang, S.; Yan, R.; Cheng, Y.; Huai, X.; Chen, S., N-octadecanethiol self-assembled monolayer coating with microscopic roughness for dropwise condensation of steam. *Journal of Thermal Science* **2009,** *18* (2), 160-165.

64. Enright, R.; Miljkovic, N.; Al-Obeidi, A.; Thompson, C. V.; Wang, E. N., Condensation on superhydrophobic surfaces: The role of local energy barriers and structure length scale. *Langmuir* **2012,** *28* (40), 14424-14432.

65. Chandekar, A.; Sengupta, S. K.; Whitten, J. E., Thermal stability of thiol and silane monolayers: A comparative study. *Applied Surface Science* **2010,** *256* (9), 2742-2749.

66. Love, J. C.; Estroff, L. A.; Kriebel, J. K.; Nuzzo, R. G.; Whitesides, G. M., Self-assembled monolayers of thiolates on metals as a form of nanotechnology. *Chem Rev* **2005,** ***105*** (4), 1103-1169.

67. Ulman, A., Formation and structure of self-assembled monolayers. *Chem Rev* **1996,** *96* (4), 1533-1554.

68. Wasserman, S. R.; Tao, Y. T.; Whitesides, G. M., Structure and reactivity of alkylsiloxane monolayers formed by reaction of alkyltrichlorosilanes on silicon substrates. *Langmuir* **2002,** *5* (4), 1074-1087.

69. Fadeev, A. Y.; McCarthy, T. J., Trialkylsilane monolayers covalently attached to silicon surfaces: Wettability studies indicating that molecular topography contributes to contact angle hysteresis. *Langmuir* **1999,** *15* (11), 3759-3766.

70. Fadeev, A. Y.; McCarthy, T. J., Self-assembly is not the only reaction possible between alkyltrichlorosilanes and surfaces. *Langmuir* **2000,** *16*, 7268-7274.

71. Naik, V. V.; Crobu, M.; Venkataraman, N. V.; Spencer, N. D., Multiple transmission-reflection ir spectroscopy shows that surface hydroxyls play only a minor role in alkylsilane monolayer formation on silica. *The Journal of Physical Chemistry Letters* **2013,** *4* (16), 2745-2751.

72. Fadeev, A. Y.; Kazakevich, Y. V., Covalently attached monolayers of oligo(dimethylsiloxane)s on silica a siloxane chemistry approach for surface modification. *Langmuir* **2002,** *18*, 2665-2672.

73. White, B. J.; Melde, B.; Malanoski, A. P.; Moore, M. H. *Bioinspired surface treatments for improved decontamination slippery omniphobic covalently attached liquid (socal)*; Naval Research Laboratory: 2017.

74. Flagg, D. H.; McCarthy, T. J., Rapid and clean covalent attachment of methylsiloxane polymers and oligomers to silica using b(c6f5)3 catalysis. *Langmuir* **2017,** *33* (33), 8129-8139.

75. Lin, Y.; Wang, L.; Krumpfer, J. W.; Watkins, J. J.; McCarthy, T. J., Hydrophobization of inorganic oxide surfaces using dimethylsilanediol. *Langmuir* **2013,** *29* (5), 1329-1332.

76. Wang, L.; McCarthy, T. J., Covalently attached liquids: Instant omniphobic surfaces with unprecedented repellency. *Angew Chem Int Ed Engl* **2016,** *55* (1), 244-248.

77. Bewig, K. W.; Zisman, W. A., The wetting of gold and platinum by water. *The Journal of Physical Chemistry* **1965,** *69*.

78. Erb, R. A., Wettability of metals under continuous condensing conditions. *Journal of Physical Chemistry* **1965,** *69* (4), 1306-&.

79. Beamish, F. E., *The analytical chemistry of the noble metals*. Pergamon Press: 1966.

80. Azimi, G.; Dhiman, R.; Kwon, H. M.; Paxson, A. T.; Varanasi, K. K., Hydrophobicity of rare-earth oxide ceramics. *Nat Mater* **2013,** *12* (4), 315-320.

81. Kulah, E.; Marot, L.; Steiner, R.; Romanyuk, A.; Jung, T. A.; Wackerlin, A.; Meyer, E., Surface chemistry of rare-earth oxide surfaces at ambient conditions: Reactions with water and hydrocarbons. *Sci Rep* **2017,** *7*, 43369.

82. Shim, J.; Seo, D.; Oh, S.; Lee, J.; Nam, Y., Condensation heat-transfer performance of thermally stable superhydrophobic cerium-oxide surfaces. *ACS Appl Mater Interfaces* **2018,** *10* (37), 31765-31776.

83. Qi, Z.; Zhang, D. C.; Lin, J. F., Surface materials with dropwise condensation made by ion-implantation technology. *International Journal of Heat and Mass Transfer* **1991,** *34* (11), 2833-2835.

84. Dearnaley, D., Ion implantation. *Nature* **1975,** *256*.

85. Do, S. C.; Kim, K. W.; Jeong, J. H., The variation of hydrophobicity of aluminum alloy by nitrogen and argon ion implantation. *Heat and Mass Transfer* **2014,** *51* (4), 487-495.

86. Wen, R.; Xu, S.; Zhao, D.; Lee, Y. C.; Ma, X.; Yang, R., Hierarchical superhydrophobic surfaces with micropatterned nanowire arrays for high-efficiency jumping droplet condensation. *ACS Appl Mater Interfaces* **2017,** *9* (51), 44911-44921.

87. Chen, X.; Wu, J.; Ma, R.; Hua, M.; Koratkar, N.; Yao, S.; Wang, Z., Nanograssed micropyramidal architectures for continuous dropwise condensation. *Advanced Functional Materials* **2011,** *21* (24), 4617-4623.

88. Enright, R.; Miljkovic, N.; Dou, N.; Nam, Y.; Wang, E. N., Condensation on superhydrophobic copper oxide nanostructures. *Journal of Heat Transfer* **2013,** *135* (9).

89. Seo, D.; Shim, J.; Moon, B.; Lee, K.; Lee, J.; Lee, C.; Nam, Y., Passive anti-flooding superhydrophobic surfaces. *ACS Appl Mater Interfaces* **2020,** *12* (3), 4068-4080.

90. Olceroglu, E.; McCarthy, M., Self-organization of microscale condensate for delayed flooding of nanostructured superhydrophobic surfaces. *ACS Appl Mater Interfaces* **2016,** *8* (8), 5729-5736.

91. Boreyko, J. B.; Chen, C. H., Self-propelled dropwise condensate on superhydrophobic surfaces. *Phys Rev Lett* **2009,** *103* (18), 184501.

92. Boreyko, J. B.; Chen, C.-H., Self-propelled jumping drops on superhydrophobic surfaces. *Physics of Fluids* **2010,** *22* (9).

93. Wen, R.; Xu, S.; Ma, X.; Lee, Y.-C.; Yang, R., Three-dimensional superhydrophobic nanowire networks for enhancing condensation heat transfer. *Joule* **2018,** *2* (2), 269-279.

94. Mukherjee, R.; Berrier, A. S.; Murphy, K. R.; Vieitez, J. R.; Boreyko, J. B., How surface orientation affects jumping-droplet condensation. *Joule* **2019,** *3* (5), 1360-1376.

95. Miljkovic, N.; Preston, D. J.; Enright, R.; Wang, E. N., Electrostatic charging of jumping droplets. *Nat Commun* **2013,** *4*, 2517.

96. Varanasi, K. K.; Hsu, M.; Bhate, N.; Yang, W.; Deng, T., Spatial control in the heterogeneous nucleation of water. *Applied Physics Letters* **2009,** *95* (9).

97. Anand, S.; Paxson, A. T.; Dhiman, R.; Smith, J. D.; Varanasi, K. K., Enhanced condensation on lubricant-impregnated nanotextured surfaces. *ACS Nano* **2012,** *6* (11), 10122-10129.

98. Cao, M.; Guo, D.; Yu, C.; Li, K.; Liu, M.; Jiang, L., Water-repellent properties of superhydrophobic and lubricant-infused "slippery" surfaces: A brief study on the functions and applications. *ACS Appl Mater Interfaces* **2016,** *8* (6), 3615-3623.

99. Kim, P.; Wong, T. S.; Alvarenga, J.; Kreder, M. J.; Adorno-Martinez, W. E.; Aizenberg, J., Liquid-infused nanostructured surfaces with extreme anti-ice and anti-frost performance. *ACS Nano* **2012,** *6* (8), 6569-6577.

100. Li, J.; Ueda, E.; Paulssen, D.; Levkin, P. A., Slippery lubricant-infused surfaces: Properties and emerging applications. *Advanced Functional Materials* **2019,** *29* (4).

101. Preston, D. J.; Song, Y.; Lu, Z.; Antao, D. S.; Wang, E. N., Design of lubricant infused surfaces. *ACS Appl Mater Interfaces* **2017,** *9* (48), 42383-42392.

102. Sett, S.; Yan, X.; Barac, G.; Bolton, L. W.; Miljkovic, N., Lubricant-infused surfaces for low-surface-tension fluids: Promise versus reality. *ACS Appl Mater Interfaces* **2017,** *9* (41), 36400-36408.

103. Smith, J. D.; Dhiman, R.; Anand, S.; Reza-Garduno, E.; Cohen, R. E.; McKinley, G. H.; Varanasi, K. K., Droplet mobility on lubricant-impregnated surfaces. *Soft Matter* **2013,** *9* (6), 1772-1780.

104. Subramanyam, S. B.; Azimi, G.; Varanasi, K. K., Designing lubricant-impregnated textured surfaces to resist scale formation. *Advanced Materials Interfaces* **2014,** *1* (2).

105. Wong, T. S.; Kang, S. H.; Tang, S. K.; Smythe, E. J.; Hatton, B. D.; Grinthal, A.; Aizenberg, J., Bioinspired self-repairing slippery surfaces with pressure-stable omniphobicity. *Nature* **2011,** *477* (7365), 443-447.

106. Lafuma, A.; Quéré, D., Slippery pre-suffused surfaces. *EPL (Europhysics Letters)* **2011,** *96* (5).

107. Epstein, A. K.; Wong, T. S.; Belisle, R. A.; Boggs, E. M.; Aizenberg, J., Liquid-infused structured surfaces with exceptional anti-biofouling performance. *Proc Natl Acad Sci U S A* **2012,** *109* (33), 13182-13187.

108. Boreyko, J. B.; Polizos, G.; Datskos, P. G.; Sarles, S. A.; Collier, C. P., Air-stable droplet interface bilayers on oil-infused surfaces. *Proc Natl Acad Sci U S A* **2014,** *111* (21), 7588-7593.

109. Günay, A. A.; Sett, S.; Ge, Q.; Zhang, T.; Miljkovic, N., Cloaking dynamics on lubricant‐infused surfaces. *Advanced Materials Interfaces* **2020,** *7* (19).

110. Sun, J.; Weisensee, P. B., Microdroplet self-propulsion during dropwise condensation on lubricant-infused surfaces. *Soft Matter* **2019,** *15* (24), 4808-4817.

111. Van Oss, C. J.; Ju, L.; Chaudhury, M. K.; Good, R. J., Estimation of the polar parameters of the surface tension of liquids by contact angle measurements on gels. *Journal of Colloid and Interface Science* **1989,** *128* (2), 313-319.

112. Van Oss, C. J.; Chaudhury, M. K.; Good, R. J., Interfacial lifshitz-van der waals and polar interactions in macroscopic systems. *Chemical Reviews* **1988,** *88*, 927-941.

113. Adera, S.; Alvarenga, J.; Shneidman, A. V.; Zhang, C. T.; Davitt, A.; Aizenberg, J., Depletion of lubricant from nanostructured oil-infused surfaces by pendant condensate droplets. *ACS Nano* **2020,** *14* (7), 8024-8035.

114. Xiao, R.; Miljkovic, N.; Enright, R.; Wang, E. N., Immersion condensation on oil-infused heterogeneous surfaces for enhanced heat transfer. *Sci Rep* **2013,** *3*, 1988.

115. Minkowycz, W. J.; Sparrow, E. M., Condensation heat transfer in the presence of noncondensables, interfacial resistance, superheating, variable properties, and diffusion. *International Journal of Heat and Mass Transfer* **1966,** *9*, 1125-1144.

116. Zhao, Y. J.; Preston, D. J.; Lu, Z. M.; Zhang, L. N.; Queeney, J.; Wang, E. N., Effects of millimetric geometric features on dropwise condensation under different vapor conditions. *International Journal of Heat and Mass Transfer* **2018,** *119*, 931-938.

117. Rykaczewski, K.; Paxson, A. T.; Staymates, M.; Walker, M. L.; Sun, X.; Anand, S.; Srinivasan, S.; McKinley, G. H.; Chinn, J.; Scott, J. H.; Varanasi, K. K., Dropwise condensation of low surface tension fluids on omniphobic surfaces. *Sci Rep* **2014,** *4*, 4158.

118. Sett, S.; Sokalski, P.; Boyina, K.; Li, L.; Rabbi, K. F.; Auby, H.; Foulkes, T.; Mahvi, A.; Barac, G.; Bolton, L. W.; Miljkovic, N., Stable dropwise condensation of ethanol and hexane on rationally designed ultrascalable nanostructured lubricant-infused surfaces. *Nano Lett* **2019,** *19* (8), 5287-5296.

119. Edwards, J. A.; Doolittle, J. S., Tetrafluoroethylene promoted dropwise condensation. *International Journal of Heat and Mass Transfer* **1965,** *8*, 663-666
.

120. Ma, X.; Wang, B., Lifetime test of dropwise condensation on polymer coated surfaces. *Heat Transfer - Asian Research* **1999,** *28* (7).

121. Paxson, A. T.; Yague, J. L.; Gleason, K. K.; Varanasi, K. K., Stable dropwise condensation for enhancing heat transfer via the initiated chemical vapor deposition (icvd) of grafted polymer films. *Adv Mater* **2014,** *26* (3), 418-423.

122. Parin, R.; Rigon, M.; Bortolin, S.; Martucci, A.; Del Col, D., Optimization of hybrid sol-gel coating for dropwise condensation of pure steam. *Materials (Basel)* **2020,** *13* (4).

123. Stephen R. Wasserman; George M. Whitesides; Ian M. Tidswell; Ben M. Ocko; Peter S. Pershan; Axe, J. D., The structure of self-assembled monolayers of alkylsiloxanes on silicon- a comparison of results from ellipsometry and low-angle x-ray reflectivity. *Journal of American Chemical Society* **1989,** *111*, 5852-5861.

124. Miljkovic, N.; Wang, E. N., Condensation heat transfer on superhydrophobic surfaces. *MRS Bulletin* **2013,** *38* (5), 397-406.

125. Preston, D. J.; Mafra, D. L.; Miljkovic, N.; Kong, J.; Wang, E. N., Scalable graphene coatings for enhanced condensation heat transfer. *Nano Lett* **2015,** *15* (5), 2902-2909.

126. Yang, Q.; Gu, A., Dropwise condensation on sam and electroless composite coating surfaces. *Journal of Chemical Engineering of Japan* **2006,** *39* (8), 826-830.

127. Vemuri, S.; Kim, K. J.; Wood, B. D.; Govindaraju, S.; Bell, T. W., Long term testing for dropwise condensation using self-assembled monolayer coatings of n-octadecyl mercaptan. *Applied Thermal Engineering* **2006,** *26* (4), 421-429.

128. Wang, Y.; Lieberman, M., Growth of ultrasmooth octadecyltrichlorosilane self-assembled monolayers on sio2. *Langmuir* **2003,** *19* (4), 1159-1167.

129. Wang, M.; Liechti, K. M.; Wang, Q.; White, J. M., Self-assembled silane monolayers: Fabrication with nanoscale uniformity. *Langmuir* **2005,** *21* (5), 1848-1857.

130. Ito, Y.; Virkar, A. A.; Mannsfeld, S.; Oh, J. H.; Toney, M.; Locklin, J.; Bao, Z., Crystalline ultrasmooth self-assembled monolayers of alkylsilanes for organic field-effect transistors. *J Am Chem Soc* **2009,** *131* (26), 9396-9404.

131. Lessel, M.; Bäumchen, O.; Klos, M.; Hähl, H.; Fetzer, R.; Paulus, M.; Seemann, R.; Jacobs, K., Self‐assembled silane monolayers: An efficient step‐by‐step recipe for high‐quality, low energy surfaces. *Surface and Interface Analysis* **2015,** *47* (5), 557-564.

132. Adera, S.; Naworski, L.; Davitt, A.; Mandsberg, N. K.; Shneidman, A. V.; Alvarenga, J.; Aizenberg, J., Enhanced condensation heat transfer using porous silica inverse opal coatings on copper tubes. *Sci Rep* **2021,** *11* (1), 10675.

133. Weisensee, P. B.; Wang, Y.; Qian, H.; Schultz, D.; King, W. P.; Miljkovic, N., Condensate droplet size distribution on lubricant-infused surfaces. *International Journal of Heat and Mass Transfer* **2017,** *109*, 187-199.

134. Liu, Y.; Wexler, J. S.; Schönecker, C.; Stone, H. A., Effect of viscosity ratio on the shear-driven failure of liquid-infused surfaces. *Physical Review Fluids* **2016,** *1* (7).

135. Wexler, J. S.; Grosskopf, A.; Chow, M.; Fan, Y.; Jacobi, I.; Stone, H. A., Robust liquid-infused surfaces through patterned wettability. *Soft Matter* **2015,** *11* (25), 5023-5029.

136. Wexler, J. S.; Jacobi, I.; Stone, H. A., Shear-driven failure of liquid-infused surfaces. *Phys Rev Lett* **2015,** *114* (16), 168301.

137. Ma, J.; Cha, H.; Kim, M. K.; Cahill, D. G.; Miljkovic, N., Condensation induced delamination of nanoscale hydrophobic films. *Advanced Functional Materials* **2019,** *29* (43).

138. Luo, H.; Liu, T.; Ma, J.; Wang, P.; Wang, Y.; Leprince-Wang, Y.; Jing, G., Evaporation-induced failure of hydrophobicity. *Physical Review Fluids* **2016,** *1* (5).

139. Pellerite, M. J.; Wood, E. J.; Jones, V. W., Dynamic contact angle studies of self-assembled thin films from fluorinated alkyltrichlorosilanes. *The Journal of Physical Chemistry B* **2002,** *106* (18), 4746-4754.

140. Cheng, J.; Vandadi, A.; Chen, C.-L., Condensation heat transfer on two-tier superhydrophobic surfaces. *Applied Physics Letters* **2012,** *101* (13).

141. Antao, D. S.; Wilke, K. L.; Sack, J. H.; Xu, Z.; Preston, D. J.; Wang, E. N., Jumping droplet condensation in internal convective vapor flow. *International Journal of Heat and Mass Transfer* **2020,** *163*.

142. Sparrow, E. M.; Eckert, E. R. G., Effects of superheated vapor and noncondensable gases on laminar film condensation. *Aiche Journal* **1961,** *7* (3), 473-477.

143. Al-Shammari, S. B.; Webb, D. R.; Heggs, P., Condensation of steam with and without the presence of non-condensable gases in a vertical tube. *Desalination* **2004,** *169* (2), 151-160.

144. Ma, J.; Porath, L. E.; Haque, M. F.; Sett, S.; Rabbi, K. F.; Nam, S.; Miljkovic, N.; Evans, C. M., Ultra-thin self-healing vitrimer coatings for durable hydrophobicity. *Nat Commun* **2021,** *12* (1), 5210.

145. Oh, J.; Zhang, R.; Shetty, P. P.; Krogstad, J. A.; Braun, P. V.; Miljkovic, N., Thin film condensation on nanostructured surfaces. *Advanced Functional Materials* **2018,** *28* (16).

146. Wilke, K. L.; Preston, D. J.; Lu, Z.; Wang, E. N., Toward condensation-resistant omniphobic surfaces. *ACS Nano* **2018,** *12* (11), 11013-11021.

147. McCarthy, M.; Gerasopoulos, K.; Maroo, S. C.; Hart, A. J., Materials, fabrication, and manufacturing of micro/nanostructured surfaces for phase-change heat transfer enhancement. *Nanoscale and Microscale Thermophysical Engineering* **2014,** *18* (3), 288-310.

148. Cha, H.; Vahabi, H.; Wu, A.; Chavan, S.; Kim, M. K.; Sett, S.; Bosch, S. A.; Wang, W.; Kota, A. K.; Miljkovic, N., Dropwise condensation on solid hydrophilic surfaces. *Sci Adv* **2020,** *6* (2), eaax0746.

149. Budakli, M.; Salem, T. K.; Arik, M.; Donmez, B.; Menceloglu, Y., Effect of polymer coating on vapor condensation heat transfer. *Journal of Heat Transfer* **2020,** *142* (4).

150. Chang, W.; Peng, B.; Khan, A. S.; Alwazzan, M.; Zhang, Y.; Li, X.; Tong, Y.; Li, C., Grain size effects on the wettability of as-grown graphene and dropwise condensation. *Carbon* **2021,** *171*, 507-513.

151. Zhu, Y.; Antao, D. S.; Lu, Z.; Somasundaram, S.; Zhang, T.; Wang, E. N., Prediction and characterization of dry-out heat flux in micropillar wick structures. *Langmuir* **2016,** *32* (7), 1920-1927.

152. Adera, S.; Antao, D.; Raj, R.; Wang, E. N., Design of micropillar wicks for thin-film evaporation. *International Journal of Heat and Mass Transfer* **2016,** *101*, 280-294.

153. Adera, S.; Antao, D. S.; Raj, R.; Wang, E. N., Hotspot thermal management via thin-film evaporation—part ii: Modeling. *IEEE Transactions on Components, Packaging and Manufacturing Technology* **2018,** *8* (1), 99-112.

154. Adera, S.; Antao, D. S.; Raj, R.; Wang, E. N., Hotspot thermal management via thin-film evaporation—part i: Experimental characterization. *IEEE Transactions on Components, Packaging and Manufacturing Technology* **2018,** *8* (1), 88-98.

155. Antao, D. S.; Adera, S.; Zhu, Y.; Farias, E.; Raj, R.; Wang, E. N., Dynamic evolution of the evaporating liquid-vapor interface in micropillar arrays. *Langmuir* **2016,** *32* (2), 519-526.

156. Brinkman, H. C., A calculation of the viscous force exerted by a flowing fluid on a dense swarm of particles. *Appl Sci Res* **1947,** *1* (1), 27-34.

157. Byon, C.; Kim, S. J., The effect of meniscus on the permeability of micro-post arrays. *Journal of Micromechanics and Microengineering* **2011,** *21* (11).

158. Liu, H.; Patil, P. R.; Narusawa, U., On darcy-brinkman equation - viscous flow between two parallel plates packed with regular square arrays of cylinders. *Entropy* **2007,** *9*, 118-131.

159. Wei, M.; He, B.; Liang, Q.; Somasundaram, S.; Tan, C. S.; Wang, E. N., Optimization and thermal characterization of uniform silicon micropillar based evaporators. *International Journal of Heat and Mass Transfer* **2018,** *127*, 51-60.

160. Xiao, R.; Enright, R.; Wang, E. N., Prediction and optimization of liquid propagation in micropillar arrays. *Langmuir* **2010,** *26* (19), 15070-15075.

161. Somasundaram, S.; Zhu, Y.; Lu, Z.; Adera, S.; Bin, H.; Mengyao, W.; Tan, C. S.; Wang, E. N., Thermal design optimization of evaporator micropillar wicks. *International Journal of Thermal Sciences* **2018,** *134*, 179-187.

162. Wang, Y. X.; Peterson, G. P., Analytical model for capillary evaporation limitation in thin porous layers. *Journal of Thermophysics and Heat Transfer* **2003,** *17* (2), 145-149.

163. Lu, Z.; Preston, D. J.; Antao, D. S.; Zhu, Y.; Wang, E. N., Coexistence of pinning and moving on a contact line. *Langmuir* **2017,** *33* (36), 8970-8975.

164. The MathWorks, I. *Matlab function reference*, 2019.

165. Srivastava, N.; Din, C.; Judson, A.; MacDonald, N. C.; Meinhart, C. D., A unified scaling model for flow through a lattice of microfabricated posts. *Lab Chip* **2010,** *10* (9), 1148-1152.

166. Tamayol, A.; Bahrami, M., Analytical determination of viscous permeability of fibrous porous media. *Int. J. Heat Mass Transfer* **2009,** *52*, 2407–2414.

167. Nam, Y.; Sharratt, S.; Cha, G.; Ju, Y. S., Characterization and modeling of the heat transfer performance of nanostructured cu micropost wicks. *Journal of Heat Transfer* **2011,** *133* (10).

168. Alhosani, M. H.; Zhang, T., Dynamics of microscale liquid propagation in micropillar arrays. *Langmuir* **2017,** *33* (26), 6620-6629.

169. Fanchi, J. R., Porosity and permeability. In *Integrated reservoir asset management*, 2010; pp 49-69.

170. Wenzel, R. N., Resistance of solid surfaces to wetting by water. *Industrial & Engineering Chemistry* **2002,** *28* (8), 988-994.

171. ANSYS *Ansys fluent tutorial guide*, 2012.

172. Sangani, A. S.; Acrivos, A., Slow flow past periodic arrays of cylinders with application to heat transfer. *International Journal of Multiphase Flow* **1982,** *8* (3), 193-206.

173. Yazdchi, K.; Srivastava, S.; Luding, S., Microstructural effects on the permeability of periodic fibrous porous media. *International Journal of Multiphase Flow* **2011,** *37* (8), 956-966.

174. Gebart, B. R., Permeability of unidirectional reinforcements for rtm. *J Compos Mater* **1992,** *26* (8), 1100-1133.

175. Drummond, J. E.; Tahir, M. I., Laminar viscous flow through regular arrays of parallel solid cylinders. *International Journal of Multiphase Flow* **1984,** *10* (5), 515-540.

176. Cho, S.; Tummala, R.; Joshi, Y., Capillary performance of micropillar arrays in different arrangements. *Nanoscale and Microscale Thermophysical Engineering* **2018,** *22* (2), 97-113.

177. Horner, D.; Ravi, S.; Moghaddam, S., Monoporous micropillar wick structures, ii-optimization & theoretical limits. *Applied Thermal Engineering* **2014,** *73* (1), 1378-1386.

178. Ravi, S.; Dharmarajan, R.; Moghaddam, S., Physics of fluid transport in hybrid biporous capillary wicking microstructures. *Langmuir* **2016,** *32* (33), 8289-8297.

179. Vaartstra, G.; Lu, Z.; Wang, E. N., Simultaneous prediction of dryout heat flux and local temperature for thin film evaporation in micropillar wicks. *International Journal of Heat and Mass Transfer* **2019,** *136*, 170-177.

180. Auriault, J.-L., On the domain of validity of brinkman's equation. *Transport in Porous Media* **2008,** *79* (2), 215-223.

181. Durlofsky, L.; Brady, J. F., Analysis of the brinkman equation as a model for flow in porous media. *Physics of Fluids* **1987,** *30* (11).

182. Gong, L.; Wang, Y.; Cheng, X.; Zhang, R.; Zhang, H., A novel effective medium theory for modelling the thermal conductivity of porous materials. *International Journal of Heat and Mass Transfer* **2014,** *68*, 295-298.

183. Li, C.; Peterson, G. P., The effective thermal conductivity of wire screen. *International Journal of Heat and Mass Transfer* **2006,** *49* (21-22), 4095-4105.

184. Mills, A. F., *Heat transfer*. McGraw-Hill, Inc.: New York, 1992.

185. Nam, K.; Jeong, S., Investigation of oscillating flow friction factor for cryocooler regenerator considering cryogenic temperature effect. *Cryogenics* **2005,** *45*, 733-738.

186. Zhang, X. B.; Qiu, L. M.; Gan, Z. H.; He, Y. L., Cfd study of a simple orifice pulse tube cooler. *Cryogenics* **2007,** *47*, 315-321.

187. Lemmon, E. W.; Bell, I. H.; Huber, M. L.; McLinden, M. O., Refprop standard reference data program, 10.0. (NIST), N. I. o. S. a. T., Ed. Gaithersburg, MD, 2018.

188. Adamkiewicz, M.; O'Hara, T.; O'Hagan, D.; Hähner, G., A vapor phase deposition of self-assembled monolayers: Vinyl-terminated films of volatile silanes on silicon oxide substrates. *Thin Solid Films* **2012,** *520* (22), 6719-6723.

189. Dorvel, B.; Reddy, B.; Block, I.; Mathias, P.; Clare, S. E.; Cunningham, B.; Bergstrom, D. E.; Bashir, R., Vapor-phase deposition of monofunctional alkoxysilanes for sub-nanometer-level biointerfacing on silicon oxide surfaces. *Advanced Functional Materials* **2010,** *20* (1), 87-95.

190. Yadav, A. R.; Sriram, R.; Carter, J. A.; Miller, B. L., Comparative study of solution-phase and vapor-phase deposition of aminosilanes on silicon dioxide surfaces. *Mater Sci Eng C Mater Biol Appl* **2014,** *35*, 283-290.

191. Arkles, B.; Steinmetz, J. R.; Zazyczny, J.; Mehta, P., Factors contributing to the stability of alkoxysilanes in aqueous solution. *Journal of Adhesion Science and Technology* **1992,** *6* (1), 193-206.

192. Sagiv, J., Organized monolayers by adsorption. 1. Formation and structure of oleophobic mixed monolayers on solid surfaces. *Journal of the American Chemical Society* **2002,** *102* (1), 92-98.

193. Maoz, R.; Sagiv, J.; Degenhardt, D.; Mohwald, H.; OQuint, P., Hydrogen-bonded multilayers of self-assembling silanes. *Supramolecular Science* **1995,** *2*, 9-24.

194. Naik, V. V.; Stadler, R.; Spencer, N. D., Effect of leaving group on the structures of alkylsilane sams. *Langmuir* **2014,** *30* (49), 14824-14831.

195. Wen, K.; Maoz, R.; Cohen, H.; Sagiv, J.; Gibaud, A.; Desert, A.; Ocko, B. M., Postassembly chemical modification of a highly ordered organosilane multilayer: New insights into the structure, bonding, and dynamics of self-assembling silane monolayers. *ACS Nano* **2008,** *2* (3), 579-599.

196. Ewers, B. W.; Batteas, J. D., Molecular dynamics simulations of alkylsilane monolayers on silica nanoasperities: Impact of surface curvature on monolayer structure

and pathways for energy dissipation in tribological contacts. *The Journal of Physical Chemistry C* **2012,** *116* (48), 25165-25177.

197. Jones, R. L.; Pearsall, N. C.; Batteas, J. D., Disorder in alkylsilane monolayers assembled on surfaces with nanoscopic curvature. *The Journal of Physical Chemistry C* **2009,** *113* (11), 4507-4514.

198. Van Oss, C. J.; Good, R. J.; Chaudhury, M. K., Additive and nonadditive surface tension components and the interpretation of contact angles. *Langmuir* **2002,** *4* (4), 884-891.

199. Jakhar, K.; Chattopadhyay, A.; Thakur, A.; Raj, R., Spline based shape prediction and analysis of uniformly rotating sessile and pendant droplets. *Langmuir* **2017,** *33* (22), 5603-5612.

200. Zhuravlev, L. T., Concentration of hydroxyl groups on the surface of amorphous silicas. *Langmuir* **2002,** *3* (3), 316-318.

201. Zhuravlev, L. T., Surface characterization of amorphous silica—a review of work from the former ussr. *Colloids and Surfaces A: Physicochemical and Engineering Aspects* **1993,** *74* (1), 71-90.

202. Fiorilli, S.; Rivolo, P.; Descrovi, E.; Ricciardi, C.; Pasquardini, L.; Lunelli, L.; Vanzetti, L.; Pederzolli, C.; Onida, B.; Garrone, E., Vapor-phase self-assembled monolayers of aminosilane on plasma-activated silicon substrates. *J Colloid Interface Sci* **2008,** *321* (1), 235-241.

203. Wiegand, M.; Reiche, M.; Gosele, U., Time‐dependent surface properties and wafer bonding of o2 ‐ plasma ‐ treated silicon (100) surfaces. *Jounral of The Electrochemical Society* **2000,** *147* (7), 2734-2740.

204. Wu, L.; Cai, L.; Liu, A.; Wang, W.; Yuan, Y.; Li, Z., Self-assembled monolayers of perfluoroalkylsilane on plasma-hydroxylated silicon substrates. *Applied Surface Science* **2015,** *349*, 683-694.

205. Yan, X.; Huang, Z.; Sett, S.; Oh, J.; Cha, H.; Li, L.; Feng, L.; Wu, Y.; Zhao, C.; Orejon, D.; Chen, F.; Miljkovic, N., Atmosphere-mediated superhydrophobicity of rationally designed micro/nanostructured surfaces. *ACS Nano* **2019,** *13* (4), 4160-4173.

206. Iler, R. K., *The chemistry of silica*. John Wiley & Sons: 1979.

207. Raj, R.; Enright, R.; Zhu, Y.; Adera, S.; Wang, E. N., Unified model for contact angle hysteresis on heterogeneous and superhydrophobic surfaces. *Langmuir* **2012,** *28* (45), 15777-15788.

208. Watson, S.; Nie, M.; Wang, L.; Stokes, K., Challenges and developments of self-assembled monolayers and polymer brushes as a green lubrication solution for tribological applications. *RSC Advances* **2015,** *5* (109), 89698-89730.

209. Moulder, J. F.; Stickle, W. F.; Sobol, P. E.; Bomben, K. D., *Handbook of x-ray photoelectron spectroscopy*. Perkin-Elmer Corporation: 1992.

210. Wagner, C. D., The nist x-ray photoelectron spectroscopy (xps) database. U.S. Government Printing Office: 1991.

211. Tsai, T. C.; McIntyre, K.; Burnette, M.; Staack, D., Copper film deposition using a helium dielectric barrier discharge jet. *Plasma Processes and Polymers* **2020,** *17* (11).

APPENDIX A

NOMENCLATURE

SAM	Self-assembled monolayer
DWC	Dropwise condensation
FWC	Filmwise condensation
CAM	Contact angle measurement
CAH	Contact angle hysteresis
AFM	Atomic force microscopy
XPS	X-ray photoelectron spectroscopy
FTIR	Fourier-transform infrared spectroscopy
HTC	Heat transfer coefficient
OTCS	Trichloro(octadecyl)silane
TFTS	Trichloro(1H,1H,2H,2H-perfluorooctyl)silane
TFDS	1H,1H,2H,2H-perfluorododecyl trichlorosilane
MNCS	Chloro(dodecyl)dimethylsilane
OTCS Controlled	OTCS coating deposited in the controlled condition with the anhydrous solvent on silicon surface
OTCS Ambient-A	OTCS coating deposited in the ambient condition with the anhydrous solvent on silicon surface
OTCS Ambient-NA	OTCS coating deposited in the ambient condition with the non-anhydrous solvent on silicon surface

TFTS Controlled	TFTS coating deposited in the controlled condition with the anhydrous solvent on silicon surface
TFTS Ambient-A	TFTS coating deposited in the ambient condition with the anhydrous solvent on silicon surface
TFTS Ambient-NA	TFTS coating deposited in the ambient condition with the non-anhydrous solvent on silicon surface
OP-C	Copper surface modified with oxygen plasma and coated with TFTS in the controlled condition surface
NP-C	Copper surface did not undergo plasma modification and coated with TFTS in the controlled condition
OP-A	Copper surface modified with oxygen plasma and coated with TFTS in the ambient condition
NP-A	Copper surface did not undergo plasma modification and coated with TFTS in the ambient condition